

POLISH ACADEMY OF SCIENCES – WROCLAW BRANCH
WROCLAW UNIVERSITY OF TECHNOLOGY

ARCHIVES OF CIVIL AND MECHANICAL ENGINEERING

Quarterly
Vol. V, No. 1

WROCLAW 2005



Surface-roughness model in traverse grinding

J. PORZYCKI

Rzeszów University of Technology, ul. Wincentego Pola 2, 35-959 Rzeszów

Shaping of the surface roughness in traverse grinding is much more complex compared to plunge grinding. What significantly influences the roughness of the machined surfaces in traverse grinding is the dressing of the grinding wheel, grinding parameters, and the form of the grinding wheel wear in this process. The occurrence of wear steps on the active grinding wheel surface (AGWS) causes that the set-up depth of cut is split into the wheel's different steps, which in turn is a reason of a varying roughness shaped by those steps. The surface-roughness model presented, which includes parameters of the grinding wheel dressing with the single point diamond dresser and grinding parameters, allows us to estimate the size of surface roughness in the process of traverse grinding.

Keywords: surface-roughness model, traverse grinding, grinding wheel dressing

1. Introduction

The surface roughness of workpiece is one of the basic values shaped in the process of grinding. Therefore, many papers present the models describing roughness, the majority of which, however, deal with plunge grinding [2, 3, 4]. Among the models presented, dependencies which have a simple form are of a practical use, making the roughness of the ground surfaces dependent on the equivalent thickness of grinding h_{eq} .

2. Surface-roughness model in traverse grinding

Shaping of the surface roughness in traverse grinding is much more complex compared to plunge grinding. This is due to the kinematics of this process and due to the form of grinding wheel wear, which differs from wear in plunge grinding. The main reason of this difference is the axial feed, which can be one- or two-directional. The quantitative and qualitative analyses of the grinding wheel wear in the process of traverse grinding were presented in a macroscopic scale by Verkerk [5]. The grinding wheel wears off in this process gradually (in sections), where the step (section) width is equal to the value of the axial feed per revolution of the workpiece f_a (Figure 1). At an initial stage, the wheel grinds with one step (Figure 1a) and the size of the wheel wear in this step is the depth of cut for the following step (Figure 1b). That way, gradually, the grinding wheel wear is developed by an emergence of the next steps (Figure 1c).

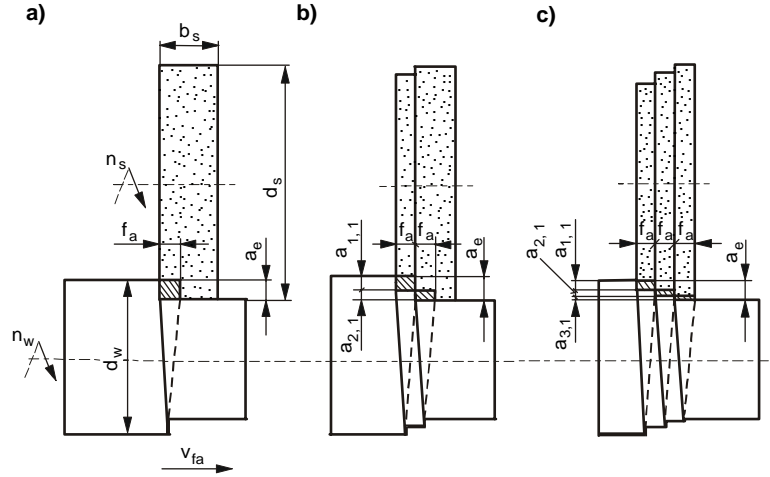


Fig. 1. Traverse grinding: a) initially the wheel grinds with one step, b), c) the next step begins to grind as soon as the first step has been worn off

The occurrence of the steps on AGWS as a result of the grinding wheel wear causes that the set up depth of cut is split into separate steps, which is a reason for a different roughness, shaped by different parts of the grinding wheel. The depth of cut for the last step is of course the smallest, therefore the roughness is low, all the more because the last part – the cylindrical part of the grinding wheel which is not worn off – partially causes the lowering of the roughness during the traverse movement. In this case, the dressing parameters play an important role, because the cylindrical part of the grinding wheel (which is not worn off) preserves, for a long time, features which are close to the ones gained in the dressing. However, the dressing parameters do not have a significant influence on the surface roughness shaped by the grinding wheel steps, which are wearing off. Therefore, the feed f_a , or actually the ratio b_s/f_a , influences (apart from the depth of cut a_e) the shaping of the roughness and, in consequence, in order to obtain its low value, wide grinding wheels should be used together with a small feed f_a .

The structure of the grinding wheel and a defined process of its dressing determine the real active surface of the grinding wheel before grinding. Using the single-point dresser in dressing allows us to affect the topography of AGWS in a simple way (Figure 2). The conditions of this process are as follows: the shape of the dresser (r_d – the radius of its top) and the dressing depth of cut a_{ed} and the dressing axial feed per revolution of the wheel f_{ad} . The parameter of the result is the overlap k_d in dressing:

$$k_d = \frac{b_d}{f_{ad}}. \quad (1)$$

As a result of the dressing process, a defined AGWS outline characterized by the parameter R_{ts} (active grinding wheel surface roughness) is obtained. It significantly influences the size of the workpiece roughness. The dependence of the parameter R_{ts} on the feed f_{ad} and the radius r_d , with $k_d \geq 1$, may be expressed as follows:

$$R_{ts} \approx \frac{f_{ad}^2}{8 \cdot r_d}. \quad (2)$$

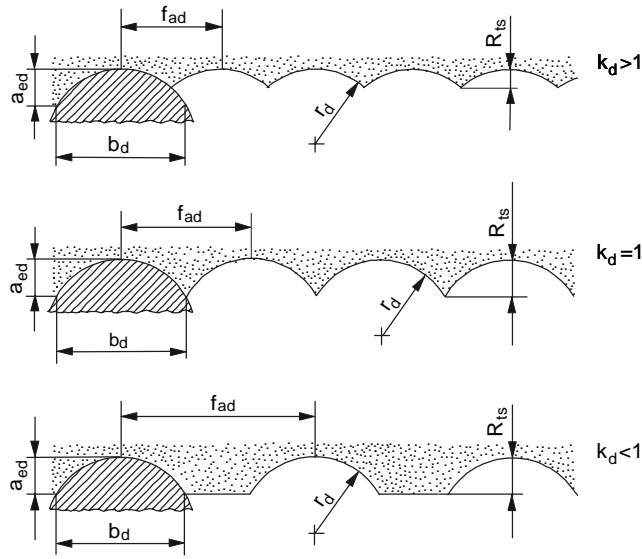


Fig. 2. The influence of the dressing parameters on the active grinding wheel surface roughness

Generally accepted dependence for estimating the workpiece roughness in the plunge grinding:

$$R_a = R_1 \cdot h_{eq}^r \quad (3)$$

should be accepted for the traverse grinding as [5]:

$$R_a = R_1^* \cdot \left(\frac{a_e}{b_s / f_a} \cdot \frac{v_w}{v_s} \right)^r, \quad (4)$$

where: R_1 , R_1^* – constants, and the exponent r is dependent on the grinding conditions (material, hardness, cooling etc.)

In order to use dependence (4) to define the roughness of the machined surfaces in traverse grinding, what has to be included is the influence of the dressing parameters on the shaped surface. This influence may be included in the connection of the roughness of the active grinding wheel surface roughness R_{ts} with the workpiece roughness. Therefore, dependence (4) may be presented as follows:

$$R_a = R_1^* \cdot R_{ts}^{r_1} \cdot \left(\frac{a_e}{b_s/f_a} \cdot \frac{v_w}{v_s} \right)^r \quad (5)$$

Including equation (2) describing R_{ts} and the constant speed ratio $q = v_s/v_w$ results in:

$$R_a = R_1^{**} \cdot \left(\frac{f_{ad}^2}{8 \cdot r_d} \right)^{r_1} \cdot \left(\frac{a_e}{b_s/f_a} \right)^r \quad (6)$$

where : R_1^* , R_1^{**} are constants.

Equation (6) was accepted as a model of the surface roughness of workpiece and, based on the results of the experimental testing, it was analysed numerically in order to arrive at its coefficients.

3. Experimental testing

Testing in traverse grinding was conducted on a test stand built on the basis of a modernized RUP 28 CNC grinder [1]. During tests of traverse grinding, the machined workpieces were made of 100Cr6 (PN-EN ISO 683-17:2002U) steel (LH15), of a 62 ± 2 HRC hardness. The 38AJ60VBE 400×50×127 grinding wheel was used and dressed with a M3010 single point dresser (produced by the VIS co.) The speed ratio was $q = 80$. The 3% Castrol oil water solution was used as a cooling and lubricating liquid. The results of the testing were determined using the regression method ($\alpha = 0.05$) and obtaining the following dependence (an average coefficient $R^2 = 0.97$):

$$R_a = 0.91 \cdot \left(\frac{f_{ad}^2}{8 \cdot r_d} \right)^{0.29} \cdot \left(\frac{a_e}{b_s/f_a} \right)^{0.5} \quad (7)$$

The examples of testing and the values of the roughness (marked with a dotted line) calculated from dependence (7) for conditions in which the testing was conducted are shown in Figures 3 and 4. Figure 5 presents the results gained from Equation (7) for the range of the radius r_d changeability (which resulted from the experimental testing) – between 0.4 mm to 0.8 mm and the feed $f_a = 6$ mm per workpiece revolution.

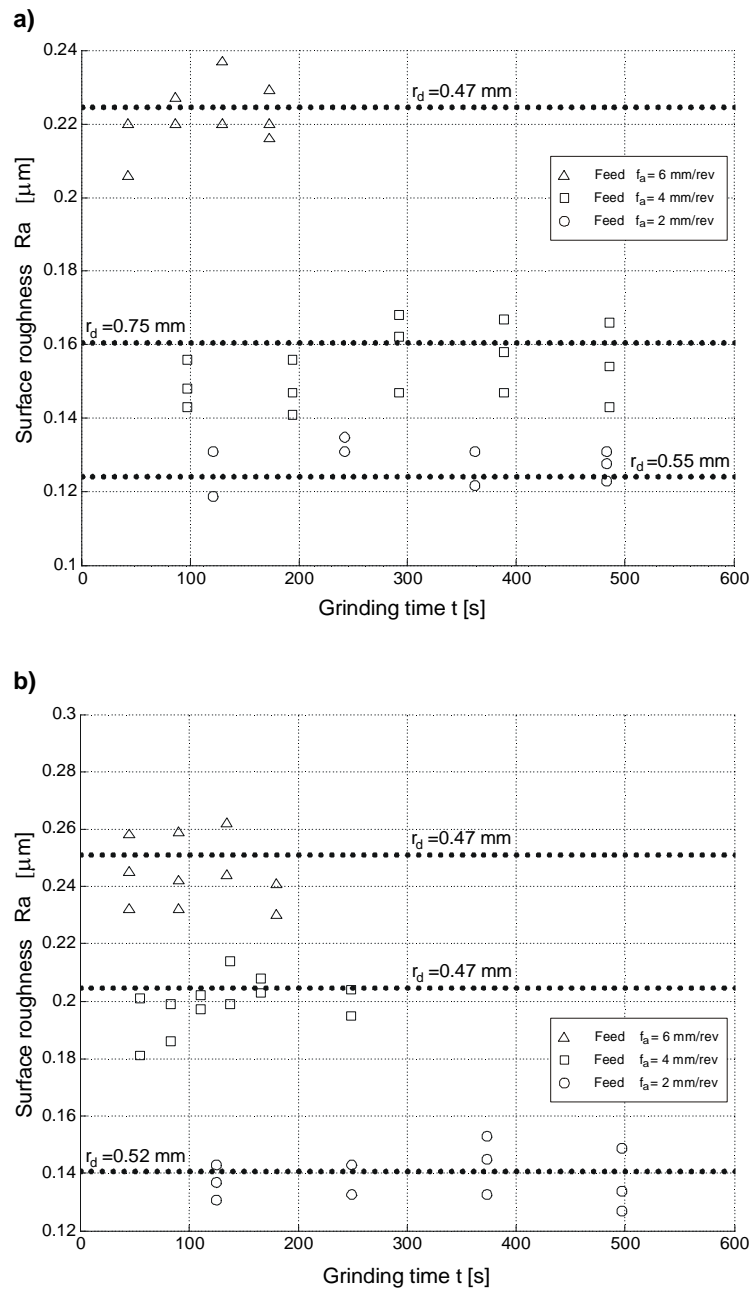


Fig. 3. Roughness of the surfaces ground with a depth of cut a_e : a) 32 μm , b) 40 μm ; finishing dressing

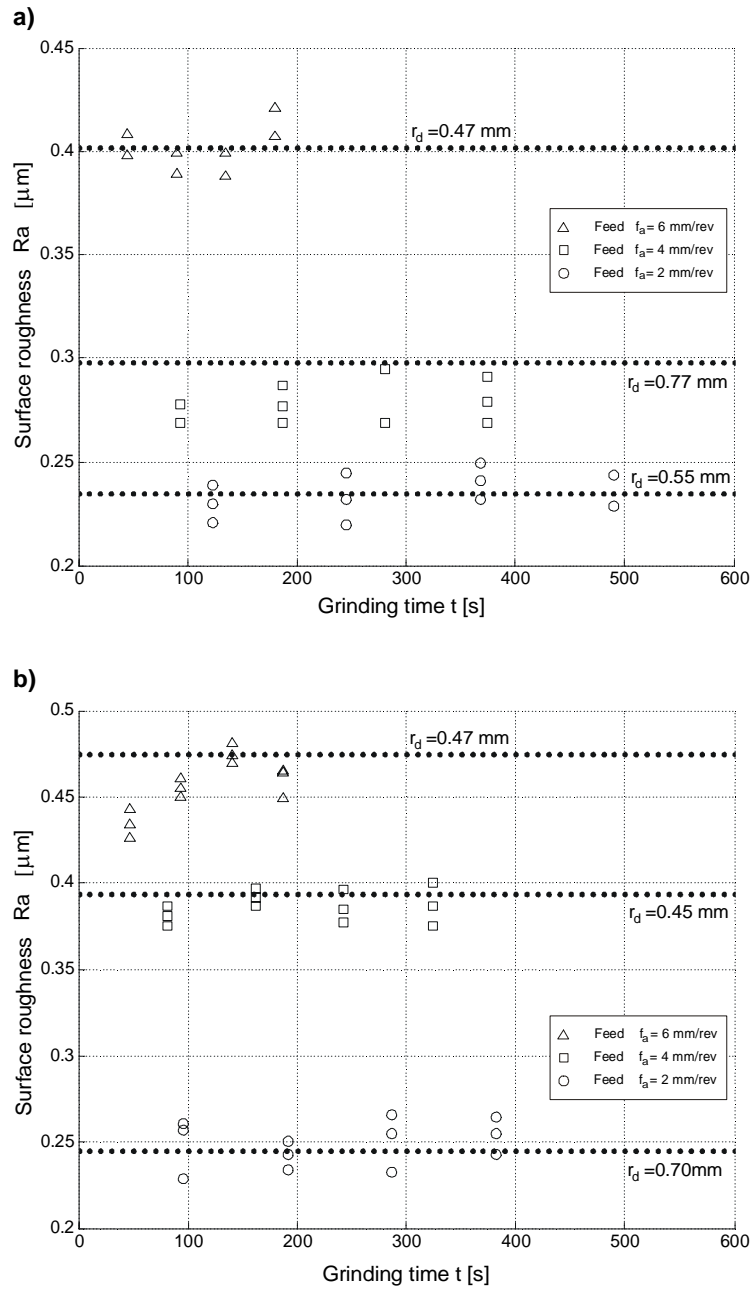


Fig. 4. Roughness of the surfaces ground with a depth of cut a_e : a) 32 μm , b) 40 μm ; rough dressing

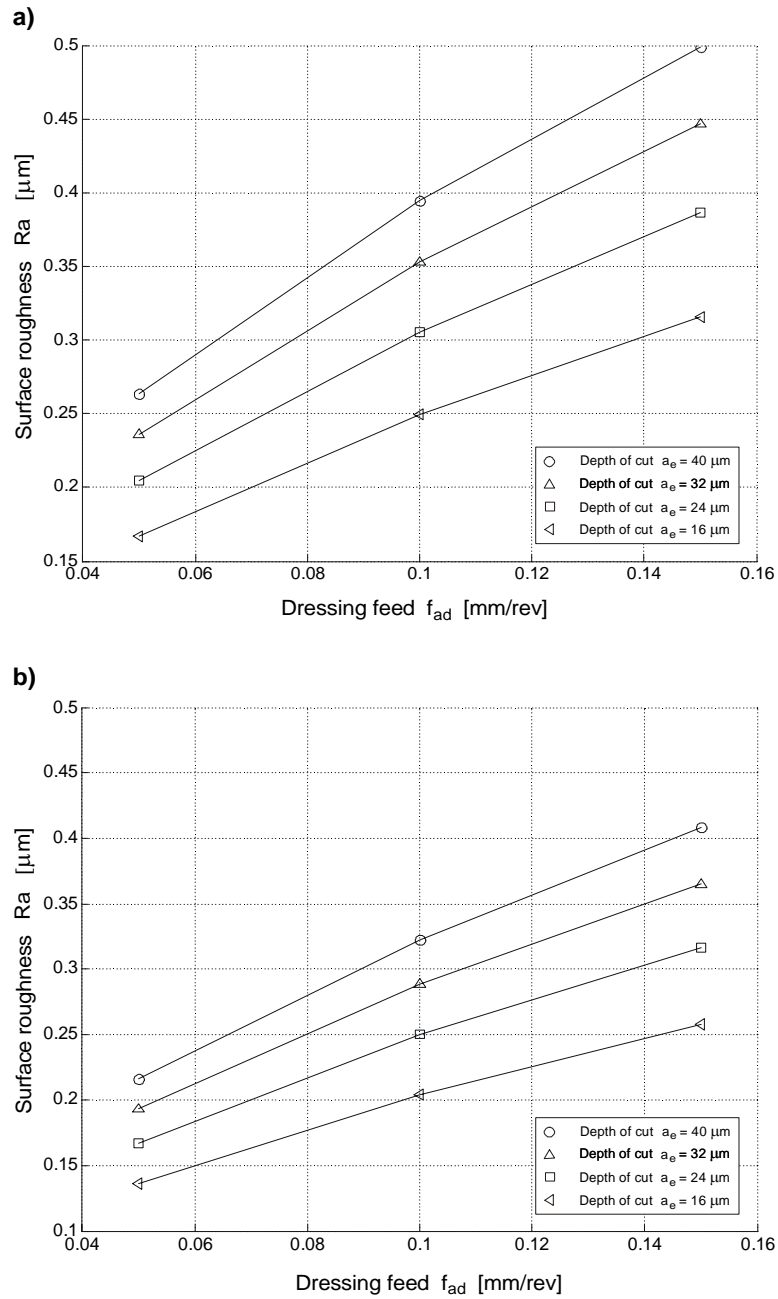


Fig. 5. Influence of the grinding depth of cut and dressing feed on the surface roughness for a dresser with a radius r_d : a) 0.4 mm, b) 0.8 mm; feed $f_a = 6$ mm/rev

4. Conclusion

Dependence (7) obtained on the basis of experimental testing allows us to estimate the surface roughness of a workpiece in traverse grinding. An analysis of these results confirms a significant influence of the dressing parameters and grinding on the surface roughness and the necessity to monitor the wearing off of a single-point diamond dresser in order to make an appropriate evaluation of the roughness of a shaped workpiece.

References

- [1] Batsch A., Pokrzycki J.: *Zastosowanie układu CNC w wersji tokarkowej do sterowania szlifierką do wałków*, XXV Naukowa Szkoła Obróbki Ściernej, Wrocław, 2002, 75–80.
- [2] Oczó K.E., Pokrzycki J.: *Szlifowanie – podstawy i technika*, Warszawa, WNT, 1986.
- [3] Peters J.: *Contribution of CIRP to the development of metrology and surface quality evaluation during the last fifty years*, Annals of the CIRP, 2001, 50, 2, 471–488.
- [4] Tönshoff H.K., Peters J., Inasaki T., Paul T.: *Modeling and simulation of grinding process*, Annals of the CIRP, 1992, 41, 2, 677–688.
- [5] Verkerk J.: *Wheel wear control in grinding. Models for the control of wheel wear, force and surface roughness by the choice of dressing and grinding conditions*, PhD Thesis, TH Delft, 1976.

Model chropowości w szlifowaniu osiowym zewnętrznych powierzchni walcowych

Kształtowanie chropowości w procesie szlifowania osiowego zewnętrznych powierzchni walcowych jest dużo bardziej złożone niż w szlifowaniu promieniowym. Zasadniczy wpływ na chropowość obrobionych powierzchni w tym procesie mają: proces obciążania ściernicy, parametry szlifowania oraz forma zużywania się ściernicy w czasie szlifowania osiowego. Pojawienie się stopni zużycia na czynnej powierzchni ściernicy (CPS) powoduje, że zadany dosuw jest rozłożony na poszczególne jej stopnie, co jest przyczyną różnej chropowości kształtowanej przez te stopnie. Opracowany model chropowości powierzchni, w którym uwzględniono parametry obciążania ściernicy obciążaczem jednoziamistym oraz parametry szlifowania, pozwala oszacować wielkość chropowości w procesie szlifowania osiowego zewnętrznych powierzchni walcowych.



Monitoring of the single-point diamond dresser wear

W. HABRAT, A. BATSCH, J. PORZYCKI

Rzeszów University of Technology, ul. Wincentego Pola 2, 35-959 Rzeszów

The geometry of the dresser is a quantity influencing the real conditions of the grinding wheel dressing. Monitoring of the dresser wear is necessary because the active grinding wheel surface depends on it, together with the resulting workpiece surface roughness. The structure of the monitoring system of the single-point diamond dresser wear, the methods of carrying out measurements and their examples have been presented in this paper.

Keywords: monitoring, wear, single-point diamond dresser

1. Introduction

The active grinding wheel surface produced in the process of its dressing plays an important role in shaping roughness of ground surfaces [2]. In the case of the grinding wheel dressing with a single-point diamond dresser, what also influences the characteristics of the active grinding wheel surface, apart from such dressing parameters as the dressing depth of cut a_{ed} and the dressing traverse feed per revolution f_{ad} , is the shape of the dresser top. The top is a result of the dresser wear and it influences at the same time the surface roughness [3]. Therefore, in consequence, monitoring of the dresser wear is necessary – it enables a correct controlling of the grinding process in terms of the required workpiece surface roughness [4].

2. Test stand

The test stand made in the Department of Manufacturing Techniques and Automation in Rzeszów University of Technology, used in carrying out experimental tests of the cylindrical traverse grinding [1], was supplied with a monitoring system of the single-point diamond dresser wear (Figure 1).

The system consists of an analog TAYAMA B/W TC-3102-08D camera 1 with a resolution of 500×582 pixels equipped with an optical system 2 with a TAYAMA M2025 lens, which allows us to magnify the specimen 200 times. The camera is attached to the headstock of the grinder by handle 3, moving with it along the X -axis. The diamond dresser 4 is placed on the tailstock of the grinder and moves along the Z -axis, together with the grinder table. Controlling the feed rates in both axes is possible due to the PRONUM 630T computer numerical control system. The image from the camera is transmitted to the PC computer 6 through the AverTV Studio 303 TV card,

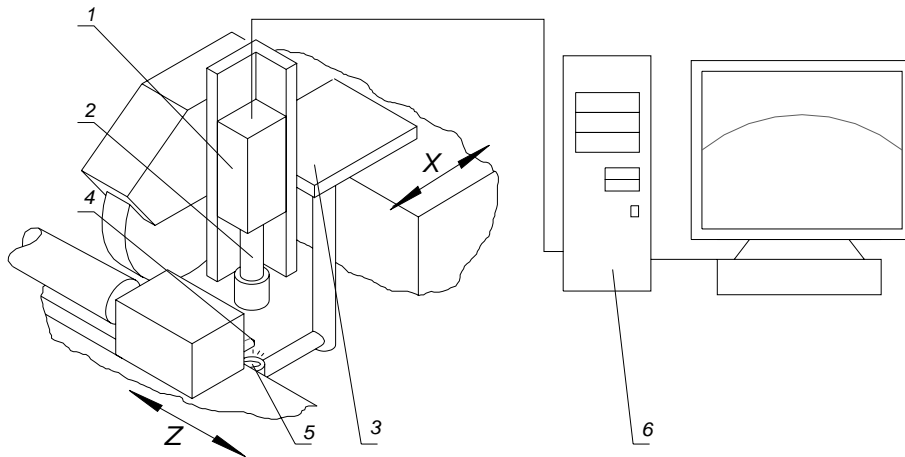


Fig. 1. A diagram of the monitoring system of the single-point diamond dresser wear:
 1 – analog camera, 2 – optical system, 3 – handle, 4 – single-point diamond dresser,
 5 – illuminator, 6 – PC computer

which is at the same time an A/C converter. In order to provide an appropriate contrast for the image produced, illuminator 5 is attached to the camera's handle. The light intensity of the illuminator is adjustable.

3. Measurement

In order to determine the equivalent radius of the diamond dresser top on the basis of its image, a computer program was developed to enable the calculation of this radius.

The image obtained from the analog camera is processed into digital form using a television card. This card allows recording the image obtained in a graphic file. Then the graphic file is processed into a matrix. The size of the matrix initially corresponds to the resolution of the image. Then, a "sub-matrix" which is centered in relation to the matrix is chosen – its size is 500×500 . The matrix selected in the above way allows processing the image, which includes filtration and digitizing of data. This is aimed at eliminating image distortions resulting from impurities in the optical system (in the case of such a big magnification and depth of field). After this processing, the matrix possesses the elements of 0 or 255 value, which denote colours – white or black correspondingly.

In the next stage, a diagram is created on the basis of the matrix, where its points are determined according to the situating of the matrix elements (line, column) defining the top edge of the diamond dresser with a simultaneous reversal of the X -axis (Figure 2).

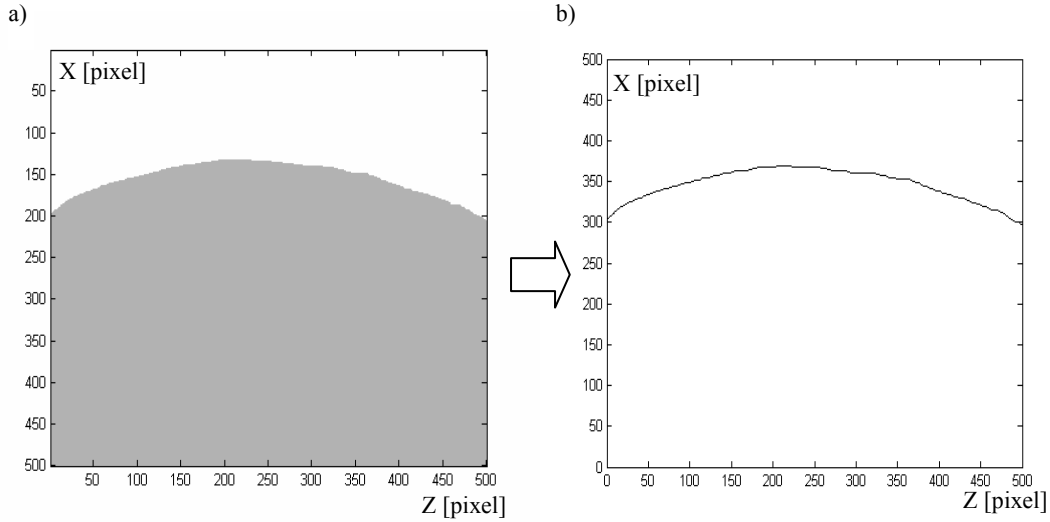


Fig. 2. Creating a diagram reflecting the top edge of the diamond dresser:
a) image of the diamond dresser top, b) the diagram created

The diagram points are determined iteratively from the following dependence:

$$A(i, j) - A(i, j + 1) < 0,$$

where:

- A – diamond dresser image matrix,
- i – number of matrix line,
- j – number of matrix column.

In the process of grinding wheel dressing, only a fragment of the dresser top resulting from the dressing depth of cut (a_{ed}) takes part. Therefore, in defining an equivalent radius, only this fragment is used. The maximum point is defined on this diagram, and then from this point the limit points resulting directly from the depth of cut are determined (Figure 3). The limit points set the above mentioned diagram fragment, the so-called active edge of the dresser.

On the basis of the points determining this part of the diagram, the approximation of the active edge of the dresser is carried out, using the circle equation:

$$Z = A_z + \sqrt{A_r^2 - (X - A_x)^2},$$

where:

- A_r – circle radius,

A_X, A_Z – coordinates of the circle centre.

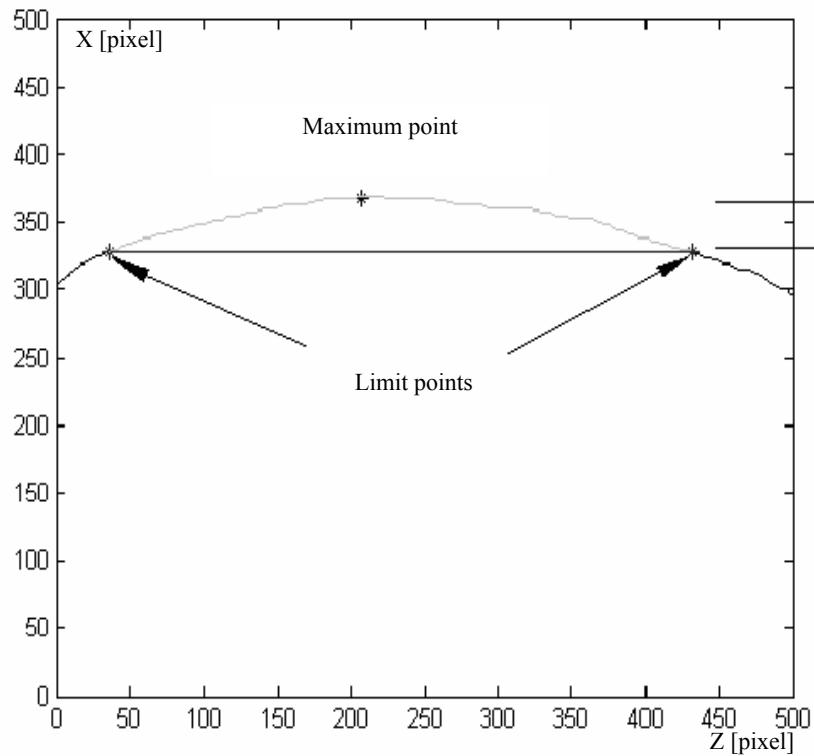


Fig. 3. Defining an active dresser edge

After the transformation of the equation obtained the radius value is expressed in pixels. The dependence which is a result of the magnification:

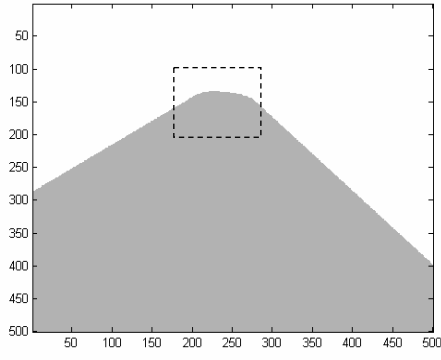
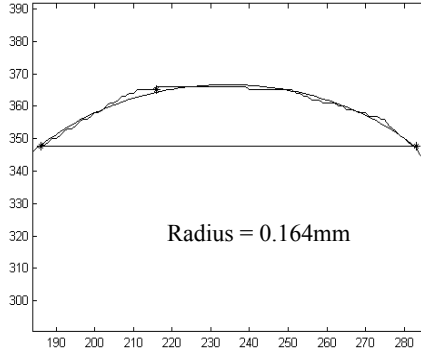
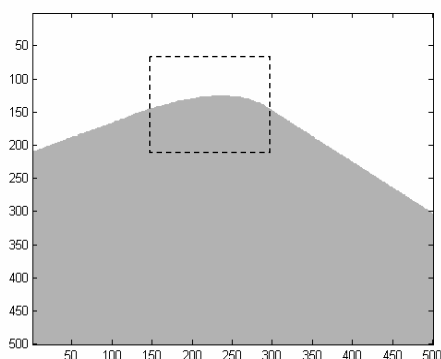
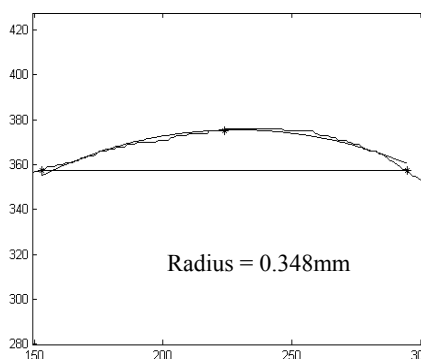
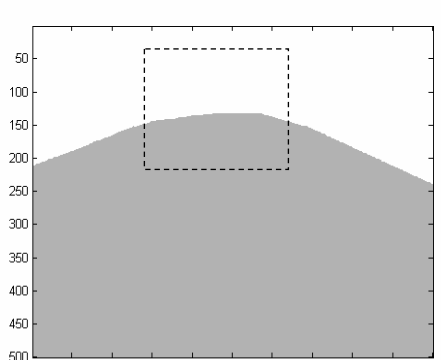
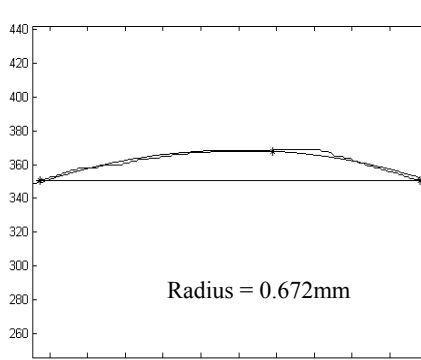
$$1 \text{ pixel} = 0.0023 \text{ mm}$$

allows calculating the value in millimetres of the equivalent radius of the single-point diamond dresser.

4. Measurement examples

Examples of measuring the equivalent radius of the single-point diamond dressers with the described monitoring wear system are presented in the Table.

Table. Examples of measurements of the equivalent radius of the single-point diamond dressers

Image of the diamond top	Active dresser edge with an approximating curve
 <p>A 2D plot showing the top profile of a diamond dresser. The x-axis ranges from 50 to 500, and the y-axis ranges from 50 to 500. A dashed rectangular box highlights the top edge of the diamond, which is approximately between x=200 and x=300.</p>	 <p>A 2D plot showing the active dresser edge with an approximating curve. The x-axis ranges from 190 to 280, and the y-axis ranges from 300 to 390. The curve is a smooth arc with a radius of 0.164mm. A horizontal line is drawn at y=350, and the curve is symmetric about this line.</p>
 <p>A 2D plot showing the top profile of a diamond dresser. The x-axis ranges from 50 to 500, and the y-axis ranges from 50 to 500. A dashed rectangular box highlights the top edge of the diamond, which is approximately between x=180 and x=280.</p>	 <p>A 2D plot showing the active dresser edge with an approximating curve. The x-axis ranges from 150 to 300, and the y-axis ranges from 280 to 420. The curve is a smooth arc with a radius of 0.348mm. A horizontal line is drawn at y=355, and the curve is symmetric about this line.</p>
 <p>A 2D plot showing the top profile of a diamond dresser. The x-axis ranges from 50 to 500, and the y-axis ranges from 50 to 500. A dashed rectangular box highlights the top edge of the diamond, which is approximately between x=150 and x=330.</p>	 <p>A 2D plot showing the active dresser edge with an approximating curve. The x-axis ranges from 140 to 320, and the y-axis ranges from 260 to 440. The curve is a smooth arc with a radius of 0.672mm. A horizontal line is drawn at y=350, and the curve is symmetric about this line.</p>

5. Conclusion

The measurements carried out show that the presented system of monitoring of the dresser wear has a simple structure and provides a quick measurement of its radius. This enables undertaking tests which aim at creating a dynamic model of the single-point diamond dresser wear. It also allows a qualitative analysis of the influence of the dresser geometry on the active grinding wheel surface developed in the process of dressing and on the resulting workpiece surface roughness.

References

- [1] Batsch A., Pokrzycki J.: *Zastosowanie układu CNC w wersji tokarkowej do sterowania szlifierką do wałków*, XXV Naukowa Szkoła Obróbki Ściernej, Wrocław, 2002, 75–80.
- [2] Gołąbczak A.: *Metody kształtowania właściwości użytkowych ściernic*, Wydawnictwo Politechniki Łódzkiej, Łódź, 2004.
- [3] Oczóś K.E., Pokrzycki J.: *Szlifowanie – podstawy i technika*, WNT, Warszawa, 1986.
- [4] Pokrzycki J.: *Modelowanie szlifowania osiowego zewnętrznych powierzchni walcowych*, Oficyna Wydawnicza Politechniki Rzeszowskiej, Rzeszów, 2004.
- [5] Przybylski L.: *Powierzchnia robocza ściernicy kształtowana jednoziarnistym obciążaczem diamentowym*, Zakłady Graficzne Politechniki Krakowskiej, Sekcja Zeszytów Naukowych i Monografii, Kraków, 1979, 2004.

Monitorowanie zużycia jednoziarnistego obciążacza diamentowego

Geometria obciążacza stanowi wielkość wpływającą na rzeczywiste warunki obciążania ściernicy. Z tego powodu konieczne jest monitorowanie zużycia obciążacza, od którego zależy czynna powierzchnia ściernicy (CPS), utworzona w procesie obciążania, i wynikowa chropowatość powierzchni obrabianego przedmiotu. W artykule przedstawiono budowę układu monitorowania zużycia jednoziarnistego obciążacza diamentowego oraz sposób pomiaru.



Notes on time buffers' estimation in CCPM

ZDZISŁAW MILIAN

Cracow University of Technology, ul. Warszawska 24, 31-155 Kraków

The aim of the paper was to analyse the estimation errors of total duration of tasks performed in sequence and simultaneously, on the basis of estimates of duration of individual tasks at various probability distribution of these durations. The estimates are directly connected with buffer sizes in Critical Chain Project Management (CCPM). An analysis of the total duration of tasks performed in sequence starts from two tasks, followed by an analysis of the effect of the number of tasks on the estimate accuracy. A total duration of tasks performed simultaneously is analysed in a similar way. From the analysis it follows that the error estimates of duration of tasks performed in sequence and simultaneously have opposite signs, which means overestimation and underestimation, respectively. Moreover, the error range depends on both the distribution type and the number of tasks. An example of probability distribution is given in which the principle that *the estimate of the sum should be smaller than the sum of estimates*, suggested in literature and used in practice in reference to the sum of random variables, is incorrect. In such a case, the buffers should not be shortened, but increased. The aim of the examples discussed in the paper was to facilitate decision taking as to buffer sizes.

Keywords: critical chain, buffer sizing, CCPM

1. Introduction

In the 1990s, the method of the Critical Chain Project Management (CCPM) was developed to be applied in project management in the case of uncertainty of individual task durations. Since that time it has been more and more commonly used in the practice of management of both single projects and many projects executed simultaneously. The idea of the method was presented in [3, 4, 11, 13]. Much information is available in the Internet [1, 5, 8, 9, 12, 14–25]. The analysis of the method in terms of new elements of management and feasibility of adopting it in construction engineering is found in [10], where a comparison was made between this method and CPM, and PERT. Moreover, in [10] comments were provided on some articles and web pages.

The idea of CPM approach in non-deterministic conditions, applied in practice so far, was that instead of deterministic task duration estimates with 90% certainty were substituted. In CCPM approach, shorter task durations are used because they are 50% certainty estimates. To secure high certainty level of project due date (e.g. 90%) the so-called buffers were introduced, which are project scheduling components measured in time units. There are the so-called project buffers and feeding buffers. The project buffer is always inserted at the end of the network, while feeding buffers are most often placed where non-critical tasks join the critical path. The planned project duration is shorter than in CPM since the project buffer is smaller than the sum of eliminated

safety margins for individual tasks in the critical chain. The safety margin of task duration is understood as the difference between duration estimates with certainty of 90% and 50%.

In literature, we can find three ways of buffer sizing. One of these was given by Goldratt [4] who suggested that the project buffer size should approximately be half the size of the sum of the preceding tasks. Similarly, the sizes of feeding buffers should be 50% duration of the corresponding feeding chains. However, as Horroelen and Leus observed [7], this simple linear rule does not hold for construction projects, the duration of which is relatively long, because its linearity means that, for instance, 12-month projects should have 6-month buffers, and a 2-year project a year-long buffer.

Another method of buffer sizing, given by Newbold [11], is more precise. Its idea is to estimate the standard deviation of critical chain on the basis of estimates of standard deviations of the tasks belonging to the chain. The result should then be multiplied by 2. This is expressed by formula

$$B = 2\sigma = 2\sqrt{\left(\frac{\bar{X}_{1,0.9} - \bar{X}_{1,0.5}}{2}\right)^2 + \left(\frac{\bar{X}_{2,0.9} - \bar{X}_{2,0.5}}{2}\right)^2 + \dots + \left(\frac{\bar{X}_{N,0.9} - \bar{X}_{N,0.5}}{2}\right)^2} \quad (1)$$

called SSQ where for each task i feeding the buffer,

$$\left(\frac{\bar{X}_{i,0.9} - \bar{X}_{i,0.5}}{2}\right)^2$$

is the variance estimate of the task duration X_i ; $\bar{X}_{i,0.9}$ and $\bar{X}_{i,0.5}$ are the estimates of quantile of 0.9 and 0.5 order of X_i , respectively. The square root of the sum of duration variance estimates, provided that task durations are independent, is the standard deviation estimate of the sum of task durations. The suggested way of calculation of the variance estimate follows from the observation that the $\bar{X}_{i,0.9} - \bar{X}_{i,0.5}$ difference equals approximately a doubled value of standard deviation, provided that tasks' durations have a lognormal distribution. In [7] however, it was proved that there is no such dependence in lognormal distribution, which in general undermines the correctness of the estimates.

In the third method, proposed by Leach [9], the buffer is divided into two components

$$B = B_{\text{var}} + B_{\text{bias}}, \quad (2)$$

where B_{var} (Variation Buffer) denotes doubled standard deviation of critical chain duration (calculated by SSQ, PERT or Monte Carlo Method), while B_{bias} (Bias Buffer) is a component related to a systematic impact of certain factors on project duration. The factors affecting B_{bias} are estimated in per cent as shown in Table 1.

Table 1. Recommendation for project buffer correction [9]

Bias Factor	Schedule Impact
Merging	< 20%
Errors	5% – 25%
Spatial Cause Variation	0% – 30%
Failure to Report Rework	0% – 20%
Total	10% – 25% (Project Buffer) More with many parallel tasks

Leach [9] recommends also that the total size of project buffer should not be smaller than 25% of the critical chain total duration.

The supporters of CCPM approach emphasize that project duration determined on the basis of 90% certainty task estimate is overestimated. It is most often argued that this project duration can be shortened between 20% and 25%, and in the case of a large number of tasks even by 40%, still guaranteeing 90% certainty of project due date. In their arguments, they refer to statistic properties of the sum of independent random variables. Since these claims and suggestions [9, 11, 4] on buffer sizing do not quite agree with probabilistic analysis, the aim of the present study was to carry out a probabilistic analysis of estimate error of project duration on the basis of estimates of individual task estimates, which will help to define the buffer sizes more accurately.

2. Two tasks in series

Let us assume one of the simplest cases of project execution, composed of two tasks performed subsequently. A scheme of such a project is shown in Figure 1.

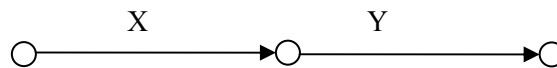


Fig. 1. Two tasks in series

Let X be duration of the first task, and Y be duration of the second one. The sum of durations of both tasks is the project duration, denoted by T . The project duration will be analysed when X and Y are random variables. Let us assume that random variables

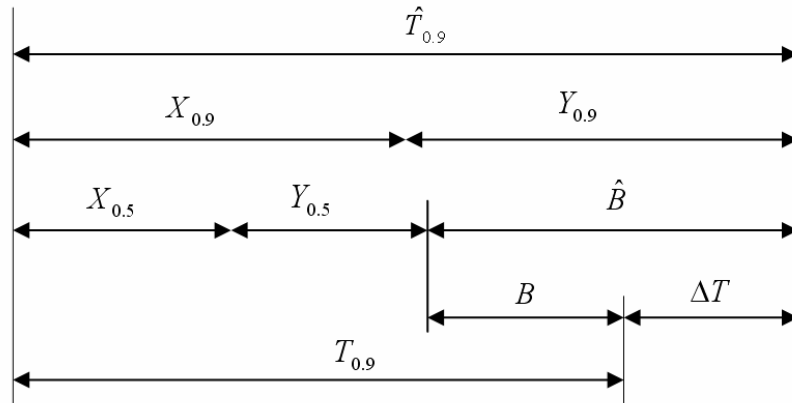
X and Y have the probability density functions denoted by $f(t)$ and $g(t)$, respectively. Thus the probability distribution functions of variables X and Y are

$$F(t) = P(X < t) = \int_{-\infty}^t f(x) dx \quad \text{and} \quad G(t) = P(Y < t) = \int_{-\infty}^t g(x) dx.$$

In further analysis, the notion of quantile will be used. For continuous random variable X quantile of the order p , denoted by X_p , is given by

$$F(X_p) = P(X < X_p) = \int_{-\infty}^{X_p} f(x) dx = p, \quad (3)$$

i.e. $X_p = F^{-1}(p)$. In CCPM method, the following duration estimate is proposed. The starting point of defining the project duration denoted by $\hat{T}_{0.9}$ is a sum of estimates of durations for individual tasks with probability 0.9. For scheduling tasks duration estimates with probability 0.5 are adopted. The resulting duration difference \hat{B} is shifted to the so-called project buffer.



Hence

$$\hat{T}_{0.9} = X_{0.9} + Y_{0.9} = X_{0.5} + Y_{0.5} + \hat{B}. \quad (4)$$

Let us denote by T the sum of random variables X and Y . Quantile $T_{0.9}$ can be expressed as follows

$$T_{0.9} = X_{0.5} + Y_{0.5} + B, \quad (5)$$

where B denotes the desired buffer size. By (4) and (5) we obtain $\hat{T}_{0.9} - T_{0.9} = \hat{B} - B$, hence

$$B = \hat{B} - \Delta T, \quad (6)$$

where $\Delta T = \hat{T}_{0.9} - T_{0.9}$. Figure 2 illustrates the relation between the variables introduced. From mathematical point of view the answer to the question whether the project duration can be shortened and if so, by how much, is reduced to the analysis of ΔT . It can be observed that if

$$(X + Y)_{0.9} < X_{0.9} + Y_{0.9}, \quad (7)$$

then the project duration estimate can be shortened.

The condition obtained can be expressed as follows: *project duration estimate can be shortened when the quantile of sum of tasks' durations is smaller than the sum of these durations' quantiles.*

The analysis of ΔT can be performed if the variable T probability distribution function is known. Since X and Y are independent and $T = X + Y$, having the probability density functions $f(t)$ and $g(t)$ of X and Y we can calculate the probability density function $h(t)$ and the probability distribution function $H(t)$ of T using the following formulas

$$h(t) = \int_{-\infty}^t f(x)g(t-x)dx, \quad (8)$$

$$H(t) = \int_{-\infty}^t f(x)G(t-x)dx. \quad (9)$$

Moreover, we shall analyse the relative difference as

$$\varepsilon = \frac{\Delta T}{\hat{T}_{0.9}}. \quad (10)$$

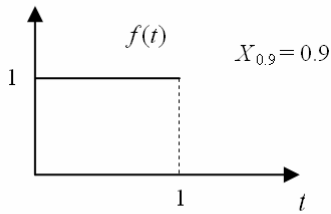
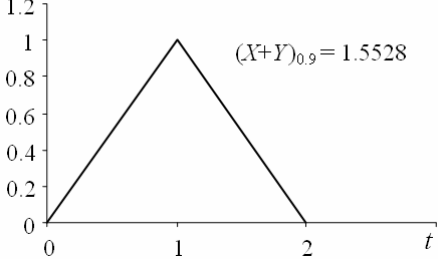
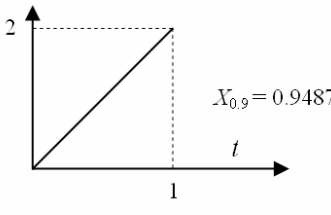
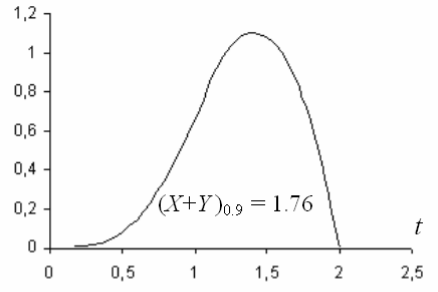
The per cent value of ε indicates by what percentage the project deadline can be shortened so that the project due date confidence was the same as that for individual tasks.

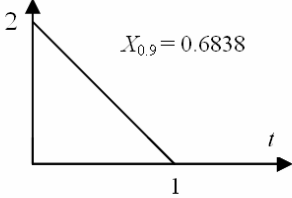
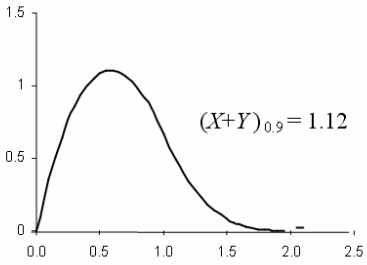
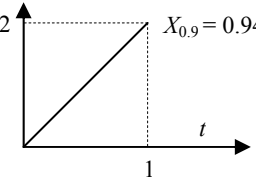
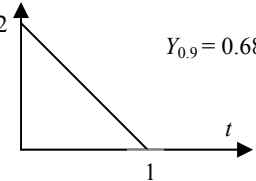
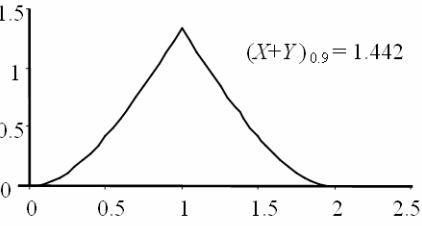
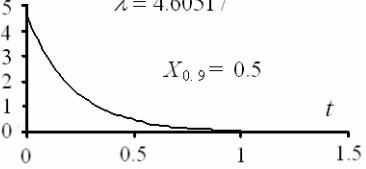
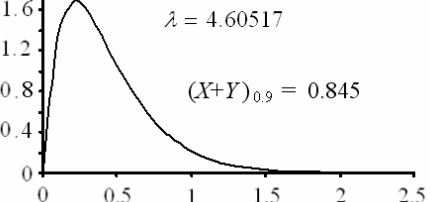
2.1. Examples where $\Delta T > 0$

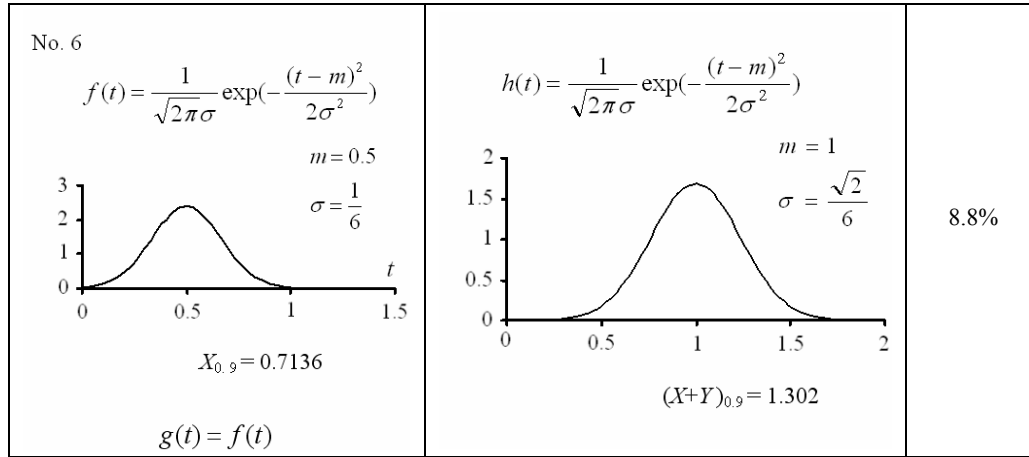
Analytical calculations of ε were made for different types of the distribution of variables X and Y . The distribution types were selected so as to obtain different shapes of the probability density $h(t)$ of the sum of X and Y . In case of distributions of unbounded range (exponential, normal), the distribution parameters were selected in

such a way that the probability of an occurrence in the interval $[0, 1]$ was at least 0.99. Practically then it is assumed that all the distributions of variables X and Y are concentrated in the interval $[0, 1]$. The values of quantiles 0.9 were calculated on the basis of dependence (3), $h(t)$ was calculated for each case on the basis of (6), and ε according to (10). The results of calculations have been tabulated in Table 2.

Table 2. Comparative tabulation of estimation errors

Probability densities $f(t)$ and $g(t)$	Probability density $h(t)$	ε
No. 1 $f(t)=1, t \in [0,1]$  $g(t) = f(t)$	$h(t) = \begin{cases} t, & 0 \leq t < 1 \\ 2 - t, & 1 \leq t \leq 2 \end{cases}$ 	13.73%
No. 2 $f(t) = 2t, t \in [0,1]$  $g(t) = f(t)$	 $h(t) = \begin{cases} \frac{2}{3}t^3, & 0 \leq t < 1 \\ \frac{8}{3} - \frac{2}{3}t^3 + 4t, & 1 \leq t < 2 \\ 0, & t < 0 \text{ or } t \geq 2 \end{cases}$	7.24%

<p>No. 3</p> $f(t) = 2(1-t), \quad t \in [0,1]$  $g(t) = f(t)$	$h(t) = \begin{cases} \frac{2}{3}t^3 - 4t^2 + 4t, & 0 \leq t < 1 \\ -\frac{2}{3}t^3 + 4t^2 - 8t + \frac{16}{3}, & 1 \leq t < 2 \\ 0, & \text{otherwise} \end{cases}$ 	<p>18.10%</p>
<p>No. 4</p> $f(t) = 2t \quad t \in [0,1]$  $g(t) = 2(1-t) \quad t \in [0,1]$ 	$h(t) = \begin{cases} -\frac{2}{3}t^3 + 2t^2, & 0 \leq t < 1 \\ \frac{2}{3}t^3 + 2t^2 + \frac{8}{3}, & 1 \leq t < 2 \\ 0, & t < 0 \text{ or } t \geq 2 \end{cases}$ 	<p>11.67%</p>
<p>No. 5</p> $f(t) = \lambda \exp(-\lambda t)$ $\lambda = 4.60517$  $g(t) = f(t)$	$h(t) = 1 - (1 + \lambda t) \exp(-\lambda t)$ $\lambda = 4.60517$ 	<p>15.5%</p>



2.2. A case where $\Delta T < 0$

The previous examples referred to cases where the sum of tasks durations estimates was greater than the estimate of tasks durations sum. However, it is not always that such relation occurs. Such a case is illustrated below. The variables X and Y are assumed to be independent and have identical probability density function $f(x)$. Let us assume that density function $f(x)$ is a positive constant in the interval $[0, a]$, equals zero in the interval $[a, 2a]$, and in the interval $[2a, 1]$ is also a positive constant. Let us assume the area below density function in the first interval to be p , and $1 - p$ in the third. The interpretation of such a distribution is as follows: if a task is not completed in the period of time $[0, a]$, there is a disruption lasting through the time a , next the task is resumed. The probability of the task completion in the period $[0, a]$ equals p . Let us determine p to be 0.9, so that it overlaps with the accuracy level of tasks duration estimate. A specific feature of this distribution is the disruption within the interval $[0, 1]$, which means that the duration cannot adopt any values in the interval $[a, 2a]$. A diagram of such a density function for $p = 0.9$ is shown in Figure 3.

The analytical formula of $f(x)$ is as follows

$$f(x) = g(x) = \begin{cases} \frac{p}{a} & \text{if } 0 \leq x \leq a, \\ \frac{1-p}{1-2a} & \text{if } 2a < x \leq 1, \\ 0 & \text{otherwise.} \end{cases} \quad (9)$$

Using (6) and (11), let us calculate the density h of $X+Y$. Let us analyse the cases depending on the position of parameter t . When $t < 0$ the integrand is always zero,

since for each x one of the functions in the product is zero. The case for t in $[0, a]$ has been illustrated in Figure 4.

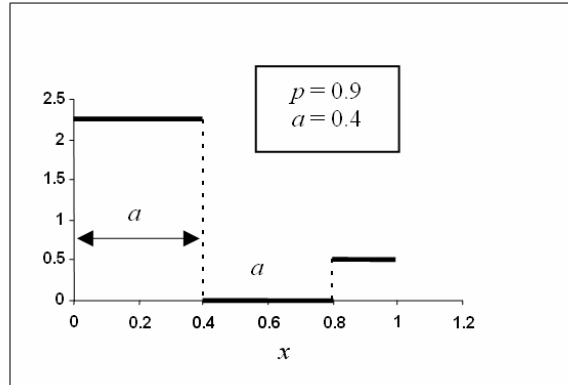


Fig. 3. Example of probability density function

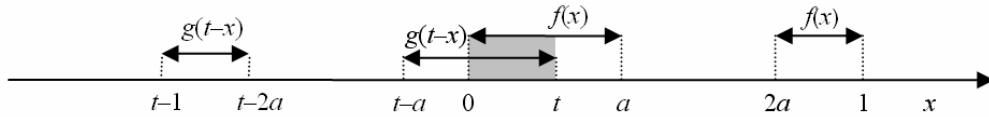


Fig. 4. Integration range where t belongs to the interval $[0, a]$

Notice that only in the interval $[0, t]$ the values of integrand will be greater than zero, so

$$h(t) = \int_{-\infty}^t f(x)g(t-x)dx = \int_0^t \frac{p}{a} \frac{p}{a} dx = \left(\frac{p}{a}\right)^2 t.$$

If t belongs to $[a, 2a]$, the integration range will be limited to $[a, t-a]$, so

$$h(t) = \int_{t-a}^a \frac{p}{a} \frac{p}{a} dx = \left(\frac{p}{a}\right)^2 t \Big|_{t-a}^a = \left(\frac{p}{a}\right)^2 (2a-t).$$

Following the same procedure for subsequent intervals we arrive at a complete formula (10) for $h(t)$, whose curve (for $p = 0.9$) has been shown in Figure 5.

Figure 6 presents the distribution function $F(t)$ common for random variables X and Y and the distribution function $H(t)$ of variable $T = X + Y$. Figure 7 shows the curves of T_p and \hat{T}_p , depending on p .

$$h(t) = \begin{cases} 0, & t < 0, \\ \left(\frac{p}{a}\right)^2 t, & 0 \leq t \leq a, \\ \left(\frac{p}{a}\right)^2 (2a - t), & a \leq t \leq 2a, \\ \frac{2p(1-p)}{a(1-2a)} (t - 2a), & 2a \leq t \leq 1, \\ \frac{2p(1-p)}{a}, & 1 \leq t \leq 3a, \\ \frac{2p(1-p)}{a(1-2a)} (1 + a - t), & 3a \leq t \leq 1 + a, \\ 0, & 1 + a \leq t \leq 4a, \\ \left(\frac{1-p}{1-2a}\right)^2 (t - 4a), & 1 + a \leq t \leq 1 + 2a, \\ \left(\frac{1-p}{1-2a}\right)^2 (2 - t), & 1 + 2a \leq t \leq 2, \\ 0, & t > 2. \end{cases} \quad (12)$$

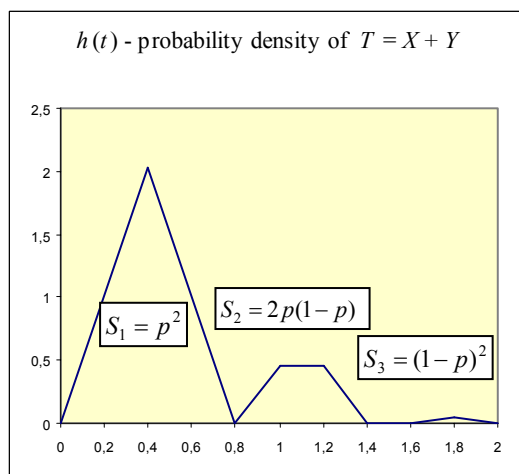


Fig. 5. Convolution of functions defined by (11)

For $p \in [0.8, 0.9]$ the estimate \hat{T}_p is below the estimate T_p , which means that the former is underestimated. The largest difference occurs for $p = 0.9$; then $\hat{T}_{0.9} = X_{0.9} + Y_{0.9} = 0.4 + 0.4 = 0.8$, while $T_{0.9} = 1.1$ thus $\varepsilon = -37.5\%$. The result proves that estimating T by the sum of quantiles can lead to underestimation. Notice that if the certainty level of estimate were greater than 0.9, the estimate would be overestimated, as in the majority of cases.

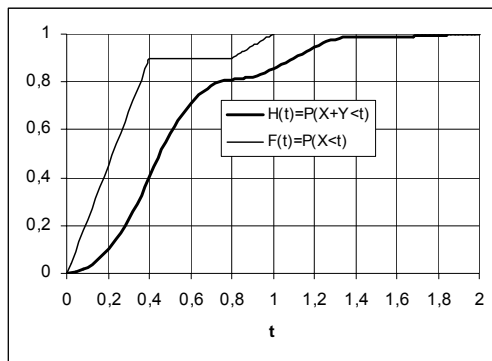
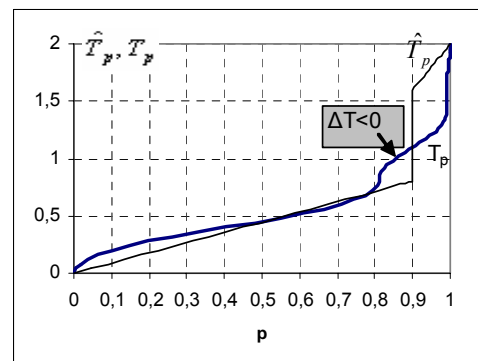
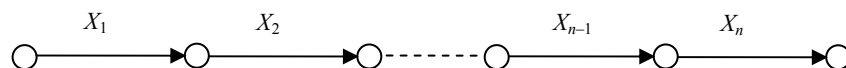
Fig. 6. Distribution function of variable X and T 

Fig. 7. Comparison of estimates

The case constructed theoretically can actually take place in the conditions of construction works when unfinished tasks have to be disrupted. The reasons may vary, e.g. shifting resources to other activities of higher priorities according to pre-scheduled task due dates, holidays, leaves of absence, etc.

3. N tasks in series

The case of two tasks can be generalised to a larger number of tasks. Let X_1, X_2, \dots, X_n denote a sequence of task durations. We assume that the tasks in the path are sequential, and that there is no parallelism. This is illustrated in Figure 8.

Fig. 8. N tasks in series

Following the previous procedure we shall analyse the error which results from estimating the sum of durations required to complete n tasks of random duration by the sum of estimates of individual durations on the assumed probability level:

$$T = \sum_{i=1}^n X_i . \quad (13)$$

If distributions of individual variables are known, the distribution of the sum T can be determined using formula (6) or (7) $n - 1$ times. Analytical solution is generally possible only in special cases, e.g. for a sequence of independent variables X_1, X_2, \dots, X_n of normal distribution, of expected value m and standard deviation σ . The estimate error was analysed according to the number of variables n and coefficient of variation, which is defined by σ / m for quantiles 0.9. The results have been illustrated in Figures 9a and 9b.

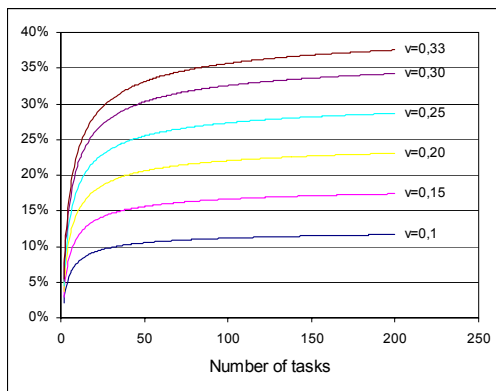


Fig. 9a. Estimate error of the sum of durations of the same distribution

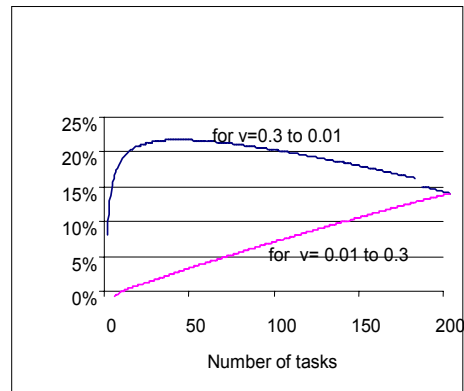


Fig. 9b. Estimate error of the sum of durations of different distribution

Figure 9a shows the results of analysis of estimate error, depending on n , when variables of the same distributions are added. As can be noticed, in this case the curve representing estimate error is monotonic and depends on both the number of variables and the coefficient of variation. Figure 9b presents the results of estimate error of partial sums of the sequence X_1, X_2, \dots, X_{200} . In this case, the distribution of variables was not the same. The coefficient of variation of the first variable was 0.01, of the last one 0.3. The increase of variation coefficient was uniform and equalled 0.00145. Two characteristics were determined for different summation ordering, one characterizing the estimate error

$$\sum_{i=1}^n X_i, \quad n = 2, \dots, 200, \text{ while the other } \sum_{i=1}^n X_{200-i+1}, \quad n = 2, \dots, 200.$$

In cases where the distributions of individual tasks durations are not normal distributions, an approximate distribution of their sum can be obtained, using a central limit theorem. According to this, accepting certain assumptions, the distribution of sum of random independent variables tends to normal distribution whose mean value is equal to the sum of the mean values of individual variables, and variance is equal to the sum of the variances of these variables. Moreover, the convolution of two normal distributions is also a normal distribution which make it possible to analyse the effect of the number of components on the estimate error level.

The characteristics collected prove that in the case of tasks in a series, the estimate error depends on both the number of variables and their parameters, the mean value and variance. Only the knowledge of these parameters allows us to make a reasonable error estimate and to calculate the size of buffer which guarantees keeping the project due date at a predetermined probability level.

4. N tasks in parallel

In network models representing project execution, there are also nodes connecting the activities executed simultaneously. Let X_i denote duration of i th task, $i=1, \dots, n$. This is illustrated in Figure 10.

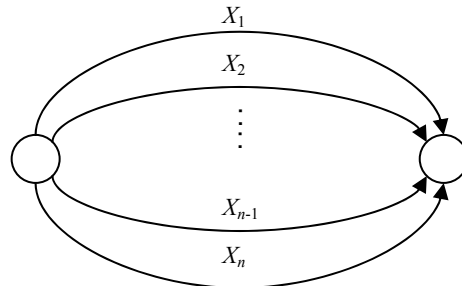


Fig.10. Tasks executed simultaneously

In this case, duration T of tasks is defined by the duration of the longest task. We can write down

$$T = \max(X_1, X_2, \dots, X_n). \quad (14)$$

As done earlier, let us assume that variables X_1, X_2, \dots, X_n are independent and the distribution of each variable is known. Let us denote the probability density func-

tion and probability distribution function of X_i by $f_i(t)$ and $F_i(t)$, respectively. By using independence of the random variables we can write down

$$P(T < t) = P(X_1 < t, X_2 < t, \dots, X_n < t) = P(X_1 < t)P(X_2 < t) \cdots P(X_n < t) = F_1(t)F_2(t) \cdots F_n(t)$$

so

$$H(t) = P(T < t) = \prod_{i=1}^n F_i(t). \quad (15)$$

Thus formula (15) enables us to calculate the probability distribution function H of duration of all tasks in parallel, provided that the probability distribution functions F_i of individual tasks are known. The probability density function $h(t)$ of the variable T can be calculated as a derivative of $H(t)$. If in the sequence of variables X_1, X_2, \dots, X_n the mean of X_i is much higher than the others, $H(t)$ distribution is approximate to $F_i(t)$. If all variables have an identical probability distribution function $F_i(t) = F(t)$, then $H(t)$ differs from $F(t)$ the most. This is why we shall analyse the case of identical probability density functions. Then (15) can be written in the form

$$H(t) = (F(t))^n, \quad (16)$$

while $h(t) = n(F(t))^{n-1} f(t)$. Like for tasks in series, let us also define the task duration estimates $\tilde{T}_{0.9}$ for task in parallel

$$\tilde{T}_{0.9} = \max(X_{1,0.9}, X_{2,0.9}, \dots, X_{n,0.9}), \quad (17)$$

where $X_{i,0.9}$ denotes the quantile 0.9 of the variable X_i . The error of this estimate is

$$\varepsilon = \frac{\tilde{T}_{0.9} - T_{0.9}}{\tilde{T}_{0.9}}. \quad (18)$$

Figure 11 presents the graphs of distribution function of the variable T for various values of n , provided that the distribution of X_i is uniform in $[0, 1]$, i.e. $F(t) = 1$ and $F(t) = t$ for $t \in [0, 1]$.

From the curves of duration distribution (Figure 11) it follows that the quantile 0.9 is shifted to the right with the growing number of tasks. On the basis of (16) $T_{0.9} = \sqrt[n]{0.9}$, while $\tilde{T} = 0.9$. The precise estimate errors have been shown in Figure 12 and tabulated in Table 3. Notice that the error sign has changed in comparison with

the tasks in series, which means that in case of tasks executed simultaneously the estimate is underestimated; in our case it ranges from -5.4% to -11% .

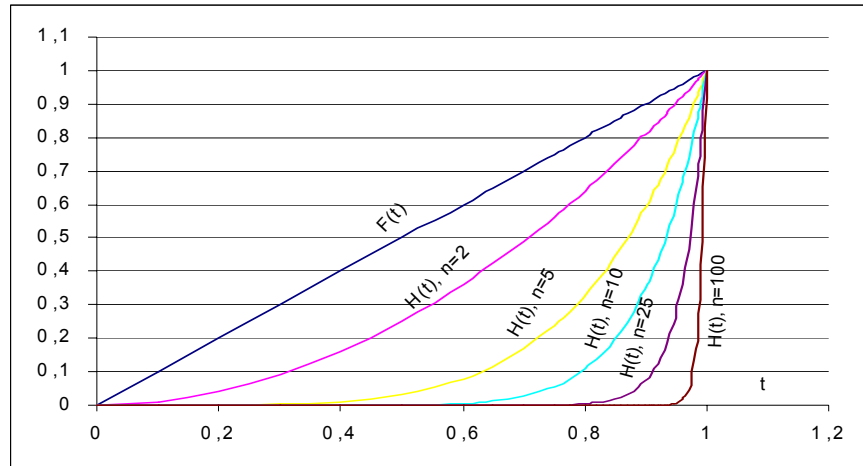


Fig. 11. Probability distribution function of $\max(X_1, X_2, \dots, X_n)$ for uniform distribution of X_i

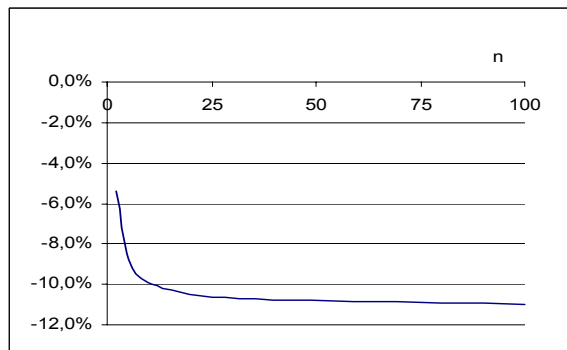


Fig. 12. Dependence of ε on the number of tasks – uniform duration distribution of individual task

Table 3. Precise estimate errors

n	$T_{0.9}$	ε
2	0.9487	-5.4%
5	0.9791	-8.8%
10	0.9895	-9.9%
25	0.9958	-10.6%
100	0.9989	-11.0%

Another case analysed also referred to tasks in parallel, but the type of task distribution changed into normal of parameters $m = 0.5$ and $\sigma = 1/6$. These parameters guarantee 99% that a value picked at random falls in the interval $[0, 1]$. The graphs of probability density function and distribution function together with the changing number of tasks n are presented in Figures 13 and 14, respectively.

In this case, also the growing n shifts the mean and the quantile to the right. The graph of probability density function gets off symmetry with respect to the mode (point at which density is at maximum) and the distribution becomes right-skewed. The values of $T_{0,9}$ and $\tilde{T}_{0,9}$ are calculated using (16) and the numerical procedure for normal distribution. It is interesting to notice the decrease of variance with the increase of n . The estimate error, cf. Figure 15 and Table 4, is larger than in the normal distribution and ranges from -29.6% to -7.6% .

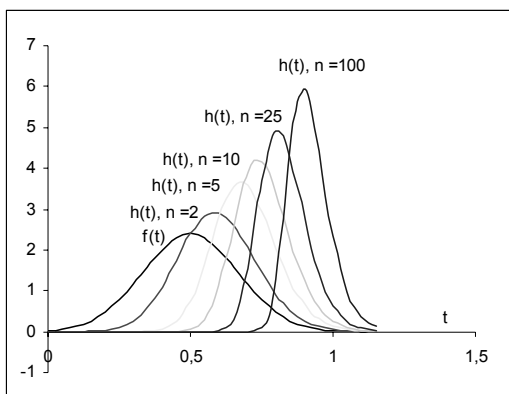


Fig. 13. Probability density functions of $\max(X_1, X_2, \dots, X_n)$ for normal distribution of X_i

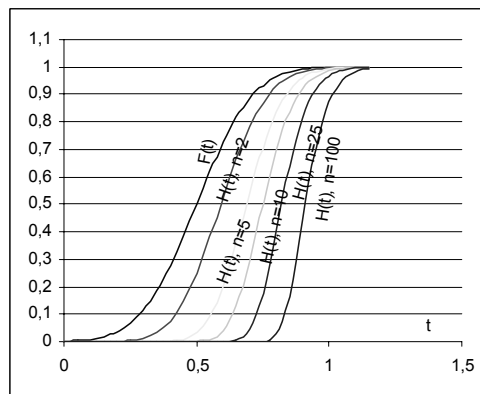


Fig. 14. Probability distribution functions of $\max(X_1, X_2, \dots, X_n)$ for normal distribution of X_i

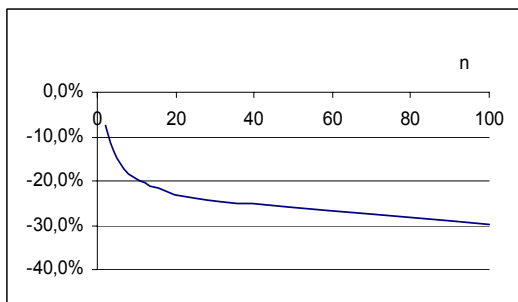


Fig. 15. Dependence of error ε on the number of tasks – single task duration is normal

Table 4. Estimate errors

n	$T_{0,9}$	ε
2	0.772317	-7.6%
5	0.840237	-15.1%
10	0.885713	-19.4%
25	0.940242	-24.1%
100	1.013749	-29.6%

The last case in our analysis refers to the exponential distribution of parameter $\lambda = 4.60517$. The value of the parameter has been selected so that 99% execution belonged to the interval $[0, 1]$. The graphs of probability density function and distribution function have been shown in Figures 16 and 17, respectively. In this case,

also the functions of density and distribution shift to the right with the growing n . This time the variance increases with an increase of n , unlike the case of normal distributions.

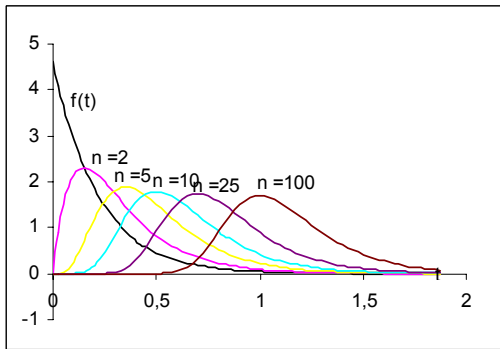


Fig. 16. Probability density functions of $\max(X_1, X_2, \dots, X_n)$ for exponential distribution of X_i

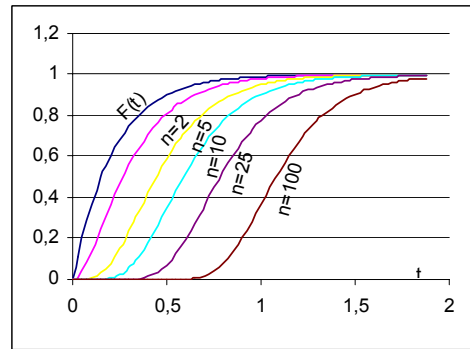


Fig. 17. Probability distribution functions of $\max(X_1, X_2, \dots, X_n)$ for exponential distribution of X_i

Relations

$$T_{0,9} = -\frac{1}{\lambda} \ln(1 - \sqrt[n]{0.9}), \quad \tilde{T}_{0,9} = \frac{1}{\lambda} \ln(10)$$

enable calculation of n dependent estimate errors ε . From Table 5 and Figure 18 it follows that the estimate error is much larger than in previous cases and its value ranges from -66.4% to -22.5% .

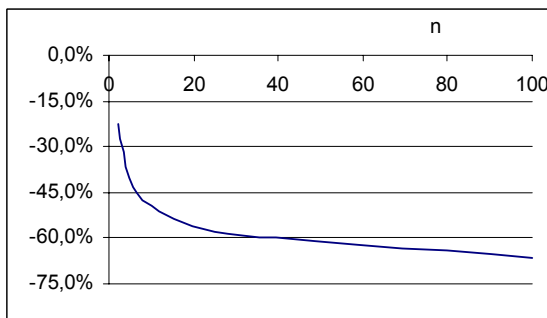


Fig. 18. Dependence of error ε on the number of tasks – single task duration has exponential distribution

Table 5. Estimate errors

n	$T_{0,9}$	ε
2	0.644871	-22.5%
5	0.84043	-40.5%
10	0.989804	-49.5%
25	1.188088	-57.9%
100	1.488775	-66.4%

5. Final remarks

As was shown in part 2 of the paper, buffer sizing results from shifting the individual tasks durations safety margins to the buffers and the error estimate of the quantiles of functions representing the duration of a set of tasks on the basis of these individual tasks durations quantiles. From the analysis performed the following conclusions can be drawn:

- generally the estimate error depends on the type of distribution (its parameters), the number of tasks, project network topology (the set of relationships determining the sequence of tasks execution), and the error size can be within the range of -64.4% – $+40\%$,
- for tasks in parallel the error has a sign opposite to that in series (excluding the case discussed in part 2.2),
- for tasks in parallel the error, depending on the number of tasks, rises faster than in series and is on a higher level.

In the majority of cases, the recommendations for buffer sizing quoted in [9] and [7] are correct. However, there are cases when they do not hold, e.g.:

- it cannot be claimed without any doubt that for task in series the sum of individual task durations estimates is larger than the estimate of task durations sum, as shown in the case studied in 2.2,
- a large number of tasks does not automatically mean that the entire project duration distribution will tend to normal distribution (e.g. two parallel task paths merging at the very end, although each can have normal distribution, but their parallel connection does not),
- the graphs given in Figures 9a and 9b show that the analysed estimate error in tasks series sequences largely depends on both the number of tasks and the scatter of individual distributions, that is why the suggested scatter estimate based on the difference in duration with 90% and 50% certainty may not be sufficient,
- for tasks in parallel the variance may increase with the number of tasks (Figure 16), not only decrease [9],
- a large number of tasks executed simultaneously in project execution may require a larger duration estimate resulting from the individual tasks estimates, which follows from the analysis of error increase with an increase in number of tasks in series and in parallel.

In analysis performed, we do not dispute the usefulness of applicability of CCPM. However, we do point to its not being universal, and consequently to the necessity of careful estimating buffer sizes. Moreover, it is essential to create one's own database that accumulates already completed projects. Such a database would include information on both planning and execution of individual tasks as well as buffer penetration, which would enable their analysis and include conclusions as to the management of the future projects.

References

- [1] Brant D.R.: *A New Vision for Project Management*, Cutter IT Journal, March 2003, Vol. 16, No. 3.
- [2] Chua D.K.H., Shen L.J., Bok S.H.: *Constraint-Based Planning with Integrated Production Scheduler over Internet*, Journal of Construction Engineering and Management, May/June 2003, Vol. 129, No. 3, pp. 293–301.
- [3] Duncan W.R.: *Back to basis: charters, chains, and challenges*, PM Network, Project Management Institute, April, 1999.
- [4] Goldratt E.: *Łańcuch krytyczny*, Warszawa, 2000.
- [5] Herzberg G.: *Identification Friend or Foe: Earned Value Management System and Critical Chain Project Scheduling*, <http://www.vancouver.wsu.edu/fac/holt/em540/Herzberg.doc>
- [6] Higgins D.: *CCPP's Visibility Problem*, Cutter IT Journal, March 2003, Vol. 16, No. 3.
- [7] Horroelen W., Leus R.: *On the merits and pitfalls of critical chain scheduling*, Journal of Operation Management, 2001, 19, pp. 559–577.
- [8] Leach L.: *Critical Chain Project Management*, Artech House Boston – London, February 2000.
- [9] Leach L.: *Schedule and Cost Buffer Sizing: How to Account for the Bias Between Project Performance and Your Model*, API, December 2002, <http://www.sphericalangle.com/ARTICLES.ASP> at 14.02.2004.
- [10] Milian Z.: *Critical Chain in Construction* (to appear, in Polish).
- [11] Newbold R.C.: *Project Management in the Fast Line – Applying the Theory of Constraints*, The St. Lucie Press, Boca Raton, 1998.
- [12] Newbold R. C.: *Bridging the Reality Gap*, Cutter IT Journal, March 2003, Vol. 16, No. 3.
- [13] Rand G. K.: *Critical chain: the theory of constraints applied to project management*, International Journal of Project Management, 2000.
- [14] Zultner R.E.: *Getting Project Out of Your System: A Critical Chain Primer*, Cutter IT Journal, March 2003, Vol. 16, No. 3.
- [15] <http://paradigm-360.com/WhitePapers/TOCleanCCPMrefs.html>.
- [16] <http://www.criticalchain.co.uk/balfourbeatty.pdf>.
- [17] http://www.ingeser.cl/toc/archivos/Casos_CCPM.doc.
- [18] http://www.realization.com/press_22-ohl.htm.
- [19] <http://www.centerpoint.pl/metccpm.php>.
- [20] <http://www.pqa.net/ccpm/W05002001.html#5%20TOC>.
- [21] <http://www.goldratt.co.uk/oa/critchpg.html>.
- [22] <http://criticalchain.co.uk/How/>.
- [23] <http://www.advanced-projects.com/TOC/Defs.html>.
- [24] <http://www.tfc.com/goldratt/>.
- [25] <http://www.kadry.info.pl/artykuly/4496.htm>.

Uwagi o szacowaniu buforów czasu w metodzie CCPM

Analizowano błąd oszacowania całkowitego czasu trwania zadań wykonywanych sekwencyjnie i równolegle na podstawie oszacowania czasu trwania poszczególnych zadań przy różnych rozkładach prawdopodobieństwa tych zadań. Oszacowania te mają ścisły związek z roz-

miarami buforów w metodzie łańcucha krytycznego do zarządzania przedsięwzięciem (*Critical Chain Project Management*). Analizę czasu zadań wykonywanych sekwencyjnie rozpoczyna się od dwóch zadań, a następnie bada się wpływ liczby zadań na dokładność oszacowania. Podobnie są analizowane zadania wykonywane równolegle. Z przeprowadzonej analizy wynika, że błędy oszacowania dla zadań wykonywanych szeregowo i równolegle mają przeciwny znak, co oznacza odpowiednio przeszacowanie i niedoszacowanie. Ponadto skala błędu zależy zarówno od rodzaju rozkładu, jak i od liczby zadań. Podano przykład, w którym sugerowana w literaturze i stosowana w praktyce zasada dla sumy zmiennych losowych, że *oszacowanie sumy powinno być mniejsze od sumy oszacowań*, jest błędna. W takim przypadku nie należy zatem skracać buforów, lecz zwiększać. Przeanalizowane przykłady mają na celu ułatwienie podejmowania decyzji związanych z rozmiarami buforów.



Simulation of non-uniformities in deep drawing processes

P. KOSTKA, P. CEKAN

Slovak University of Technology in Bratislava, Faculty of Mechanical Engineering, Department of Materials and Technologies, Pionierska 15, 812 31 Bratislava 1, Slovakia

In the process design stage of deep drawn components, an innovative concept means introduction of new features in the area of blankholders. When deep drawing the complex sheet metal parts, one must be able to control the flow of the non-uniformities of material between the punch and die in order to eliminate the undesired occurrence of wrinkling and tearing of a drawn component. This can be made possible through the adjustment of nominal forces acting on the blank through the blankholder. In the case of non-uniformities in blankholder pressure, an advanced computer-aided interaction approach brings advantages to the process design stage. This paper briefly discusses some results of simulations and experimental verification in tooling with the possibility of blankholder pressure control.

Keywords: *deep drawing, simulation, experiments, non-uniformities, tailored blanks*

1. Introduction

In engineering design, one of the most important tasks is to predict the consequences of the approaches chosen in early design stages. Engineers, who work with product design and development, must know the importance of understanding the complete process from conceptual design to the final planned production. In order to reduce overall costs of a process, a greater effort should be put in the early phases of product design planning. In the past, it was very difficult to study partially the process simulation due to the lack of computer power and an available technology. Today, advanced computational methods along with faster and higher performance computers have given us the opportunity to study the characteristics of a product or a process with high accuracy. This advantage allows computer simulations to help the mechanical engineer to understand better the product or process and to make corresponding improvements. Nowadays every product is more or less simulated, from a complete system to individual components.

In this paper, a study of the deep drawing forming is presented. It is focused mainly on the important process and material parameters that cannot be ignored in the deep drawing process. The process of cylindrical cup drawing is simulated along with experimental evaluation of the results computed. Important characteristics of sheet metal were experimentally determined in previous investigations. In the first stage, the "ideal" process of deep drawing with uniform blank thickness and uniform pressure distribution in the blankholder area was studied. In the second stage, the metal flow of

a tailored blank was investigated both in conditions of uniform and non-uniform distributions of blankholder pressure [1].

2. Computer simulations of a cylindrical cup

In order to investigate the deep drawing simulation of a cylindrical cup, we used DYNAFORM-PC, a modern stamping simulation software applied primarily in the U.S.A. The DYNAFORM-PC software package consists of four programs. These programs represent the pre-processor, solver and two post-processors. They are DYNAFORM, LS-DYNA, eta/PostGL and eta/Graph. DYNAFORM is the pre-processor portion of this software package. Sheet-metal forming models are constructed using this software, which includes VDA and IGES translators for importing line data and a complete array of tools for altering or constructing line data and as well as meshing it. LS-DYNA is the software package's solver. DYNAFORM has a complete LS-DYNA interface allowing the user to run LS-DYNA from DYNAFORM. The eta/PostGL and eta/Graph are the post-processing portions of this package. These programs are used to post-process LS-DYNA result files from the analysis. eta/PostGL creates contour, deformation, FLD, and stress plots as well as animations with the result files. eta/Graph contains functions for graphically interpreting the same results [2], [3].

2.1. Input properties for sheet-metal drawing simulations

In order to run a simulation in DYNAFORM-PC, we created a simulation model and inputted the tool and blank material properties into the simulation software. In this work, we simulated the drawing of a circular cup with an inner diameter of $d_1 = 79$ mm, inside die and blankholder diameters of 81.4 mm, drawing gap of 1.2 mm, die radius of 8 mm and punch radius of 8 mm. Uniform sheet-metal thickness of 1 mm for blank diameters of 140, 150, 170 and 180 mm was used, which corresponded to deep drawing ratios of 1.77, 1.96, 2.15 and 2.34. In addition, we also performed computer simulations on tailored blanks with a diameter of 140 mm, where exactly half of the blank was thinned down from 1 mm to 0.85 mm. This concept of a tailored blank introduced non-uniformity in blankholder pressure design.

In order to determine the required blankholder pressure needed for each blank, the authors took into consideration the following equations:

- according to Tschatsch [4]

$$p_1 = \left[(K - 1)^2 + \frac{d_0}{200 \cdot t_0} \right] \cdot \frac{R_m}{400}, \quad (1)$$

- according to Lange [5]

$$p_2 = 0.0025 \cdot \left[(K-1)^3 + 0.5 \cdot \frac{d_0}{100 \cdot t_0} \right] \cdot R_m, \quad (2)$$

- according to Siebel [6]

$$p_3 = 0.0023 \cdot \left[(K-1)^3 + 0.5 \cdot \frac{d_0}{100 \cdot t_0} \right] \cdot R_m, \quad (3)$$

where K is the deep drawing ratio, d_0 is the initial blank size, t_0 is the average blank thickness, R_m is the ultimate tensile strength.

Figure 1 shows the tool assembly designed for the deep drawing process by the CAD program ProEngineer 2000i. This assembly was saved as an .igs format file, which was then easily imported into the DYNAFORM-PC software.

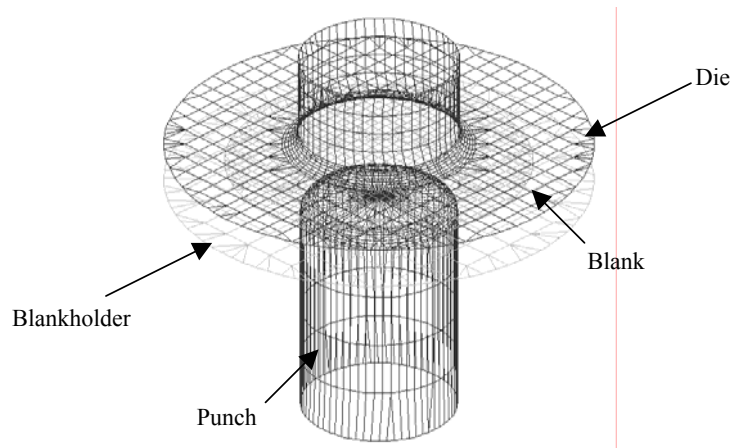


Fig. 1. Tool assembly imported into DYNAFORM-PC

Using the material properties of our experimental metal sheet (11305.21, STN 420127, yield stress $R_{p0.2} = 215$ MPa, ultimate tensile stress $R_m = 320$ MPa) we were able to define the properties of the blank exactly. After setting up the tool and blank material properties we could then run the LS-DYNA computation engine, but first we had to define the frictional properties, anisotropy coefficients, refinement level and adaptive properties. The friction coefficient selected for these simulations was $\mu = 0.12$ (which is the default value in DYNAFORM), the anisotropy coefficients found by us experimentally and inputted into the program were: $r_0 = 1.87$, $r_{45} = 1.23$ and $r_{90} = 2.15$, refinement level 5 and the adaptive value properties of 6. After computation (which lasted between 12–16 hours), LS-DYNA plotted its computations in dplot format, which was then read in the programs eta/PostGL and eta/Graph.

2.2. Simulation results

The results from DYNAFORM-PC provided good insight into the deep drawing process. In our simulated tests, we inputted the blankholder pressures (Table) provided by [4], [5] and [6]. What we found was that when we inputted the resulting pressures calculated using Equations (2) and (3) the blankholder pressure was too low and extensive wrinkling took place. On the other hand using Equation (1) for calculation of blankholder pressure no wrinkling was seen. Thus in this work we adapted the blankholder pressures calculated from Equation (1).

Table. The calculated values of blankholder pressure

K	d_0 [mm]	p_1 [MPa]	p_2 [MPa]	p_3 [MPa]
1.77	140	1.04	0.93	0.85
1.96	150	1.34	1.30	1.20
2.15	170	1.74	1.89	1.74
2.34	180	2.15	2.64	2.43

The simulated results obtained show in an impressive way the consequences of the properties of inputted anisotropy properties of the material used (Figure 2). This is in the form of ears and dips located at the edges of the cup after the computer simulated drawing process.

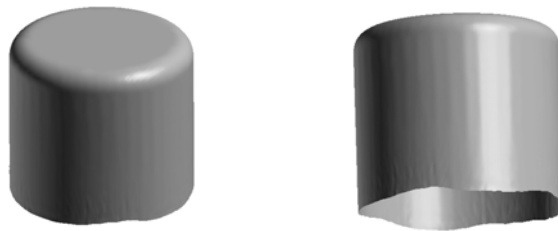


Fig. 2. Different views of the simulated drawn cup with an initial blank size of 170 mm

In order to calculate the strain distribution, a circular grid was implemented in the DYNAFORM-PC software. This allowed us to calculate the strain automatically by zooming in on the cup in eta/PostGL and eta/Graph. This then meant that we were able to calculate φ_1 which is the strain in the transverse direction, φ_2 which is the strain in the longitudinal direction as well as φ_3 which is the negative sum of $\varphi_1 + \varphi_2$ and the strain in the thickness direction. These values were then taken and processed in the graphical program of Microsoft excel. Figure 3 shows the strain distribution of an initial blank of 170 mm. In this figure, one must understand that the dip direction under consideration is the direction of a line in between the ears of the cup, and the ear direction is the line perpendicular to the tangent of the highest point of the ear, which is approximately 45° to the line in the dip direction (Figure 4).

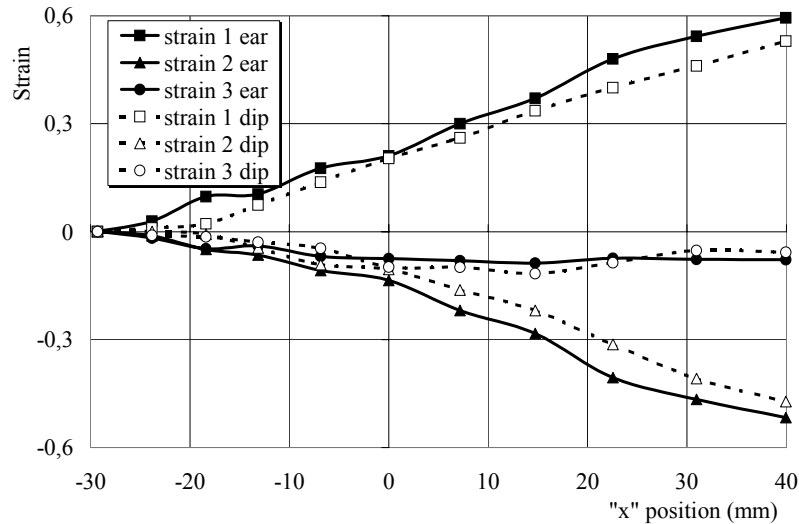


Fig. 3. Simulation strain distribution of a cup with an initial blank diameter of 170 mm

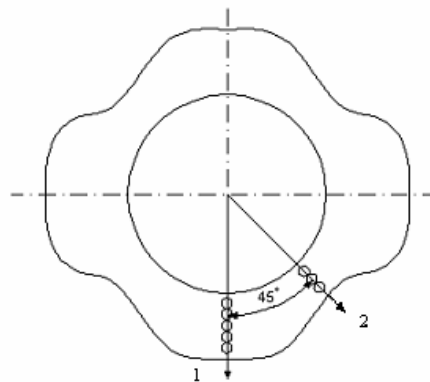


Fig. 4. Exaggerated view of the flange of a cylindrical deep drawn part:
1 – ear direction, 2 – dip direction

With regard to the computer simulations of tailored blank, the simulation was regarded as very interesting and instructive, because this is a fairly new area in computer simulations of deep drawing and it is worth mentioning that comparatively little exploration and attention have been devoted to this field. As said previously, it is very interesting to look at the results of the computer simulation of the 140 mm tailored blank. Figure 5 shows the travel of the borderline dividing the tailored blank parts of different thickness. There is also evidence of preferred flow of the blank material into the die-punch gap at the places of greater thickness next to the indication of small amplitude wrinkles at the opposite side and near the flange.



Fig. 5. Different views of a simulated drawn cup with an initial tailored blank size of 140 mm

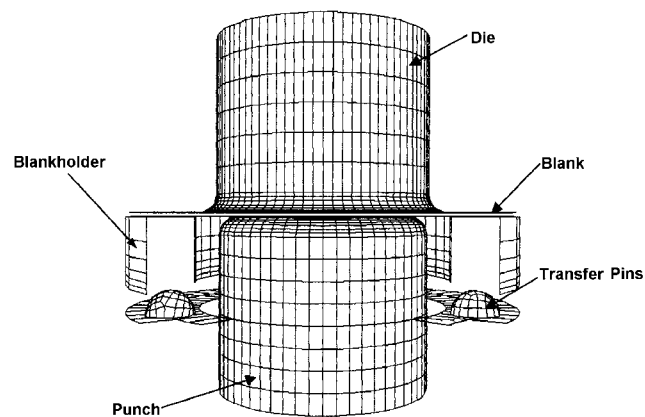


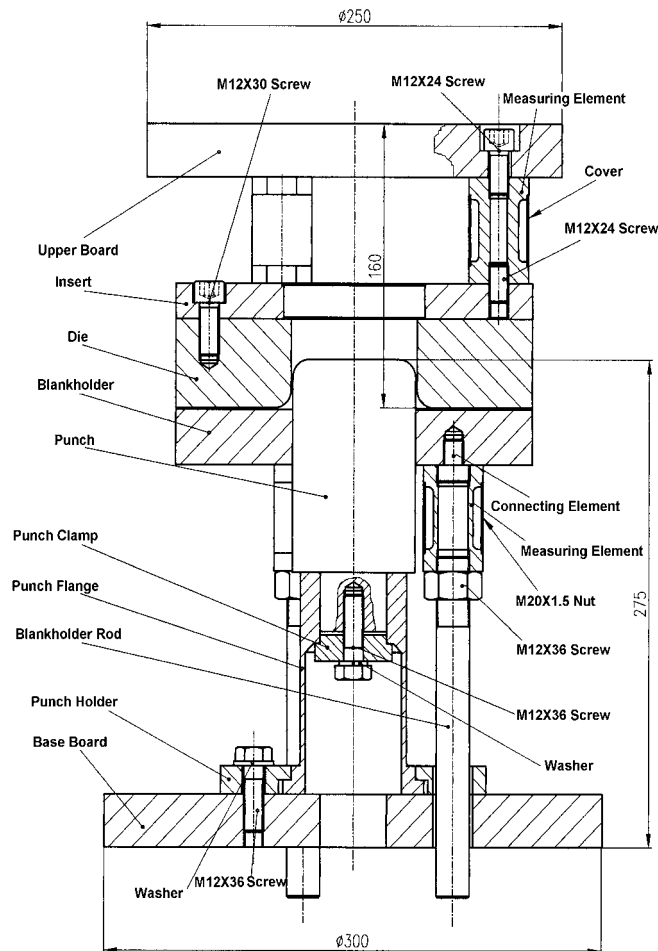
Fig. 6. Suggested model construction for the non-uniform distribution of blankholder pressure

In this simulation package, it was not possible to simulate the drawing of a cup with non-uniform blankholder pressure. The software available in the early stage of our research did not allow us to define a tool part other than a rigid material. For future work it was assumed that the model construction for non-uniform distribution of blankholder pressure, which is secured by a non-rigid blankholder plate, would be supported by a number of transfer pins (see Figure 6). The pins transfer the load from the die cushion. The difference in individual loads transferred by the pins may be controlled either by adjusting the individual power transferred by the pins or by the change in their lengths. For future work in this area it is suggested to follow the schematic Figure 6 for the non-uniform distribution of the blankholder pressure, where the rigid blankholder is transferred with a number of transfer pins, where each transfer pin can be adjusted to yield different forces.

3. Experimental verification

The cross-section of experimental tooling for verification of computer simulation is shown in Figure 7. It corresponds to a “single-action drawing tool with a draw cush-

ion” [7]. The forming force is exerted by the slide above through the die and the blankholder onto the cushion in the press bed. The draw punch and the blankholder of the drawing tool are both located in a base plate on the press bed. Pressure pins, which come up through the press bed and the base plate, transfer the blankholder force from the draw cushion onto the blankholder. The female die and the blankholder are mounted on the press slide. At the start of the forming process the blank is held under pressure between the draw die and the blankholder. The slide of the press pushes the blankholder downward over the draw die – against the upward-acting force of the draw cushion. The part is formed via the downward movement of the die over the stationary draw punch. The press slide must apply both the pressing and the blankholder



forces.

Fig. 7. Experimental tooling

The tooling was instrumented to measure the punch load by means of gauges fixed on the punch flange (Figure 7). The stroke was indicated using a displacement gauge. Moreover, the blankholder load (pressure) and die load were possible to adjust and to on-line control by means of three measuring gauges for the blankholder and three measuring gauges for the die (refer to Figure 7). The tooling was then assembled into the hydraulic C frame press PYE 160. This hydraulic press has the following process and control properties:

Press type:	PYE 160 S.
Forward-nominal force:	120 Mp.
Retractable head velocity:	0.100 m/sec.
Maximum stroke distance:	500 mm.
Minimum distance between table & retractable head:	32/60.
Ejector force:	32 Mp.
Elevation:	160 m.

The lubricant that was used was called WEDOLIT Z 1043. It is a high-performance lubricant with excellent temperate protection against corrosion. It is also a good degreaser and partially evaporates so no chemicals are needed to remove it. It is used for the deep drawing of carbon steel blanks with no additional phosphorous layer, and the friction coefficient was estimated at 0.12, the lubricant is also self-adaptive. The lubricant was evenly coated on each blank before the deep drawing operation.

When we experimentally verified blankholder pressures obtained from the formulas (1), (2) and (3) we found that the highest values given by formula (1) provided the most satisfactory results. Lower pressure levels resulted in large amplitudes of wrinkles as shown in Figure 8.

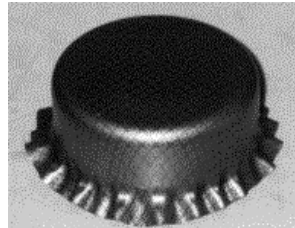


Fig. 8. Wrinkling due to low blankholder pressures calculated from (2), (3)

Generally the simulations provided an in-depth evaluation of the deep drawing process and as well as the results that were comparable to experimental verifications. In our experimental simulated cup drawing, we have seen that in all cases the simulated curves predicted the results of experiments. In Figure 9, one may see the plot of punch stroke versus the punch, die and blankholder forces for a 170 mm initial blank, where the die and blankholder forces are the sum of the partial loads exercised on the three different measuring gauges. Note the similarities between computer simulations and experiments.

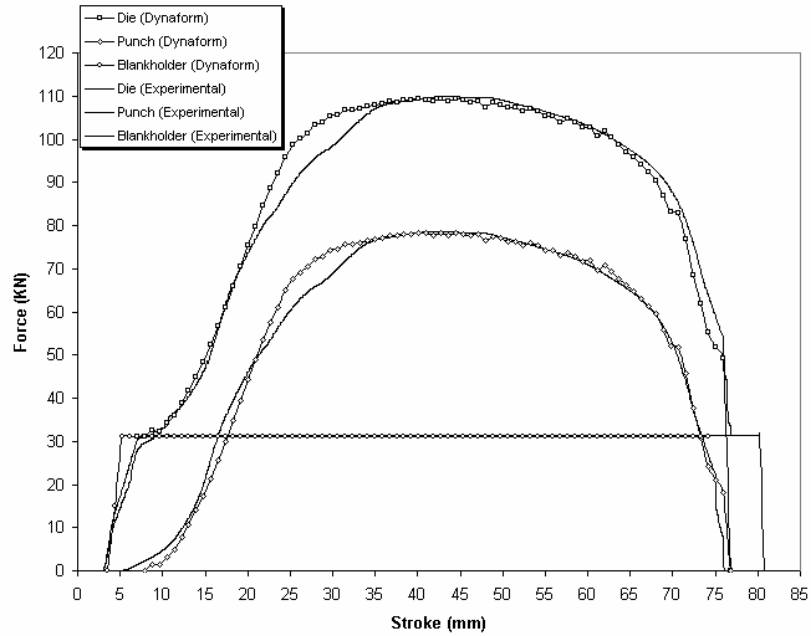


Fig. 9. Comparison of simulated and experimental force characteristics (170 mm initial blank)

For the evaluation of strain distribution on the non-uniform blankholder drawings, we measured the deformed circles along the imaginary axis from the highest blankholder pressure point to the other side of the cup. The zero position value is the mid point of the cup (Figures 10 & 11). We then measured a line 45° with respect to the

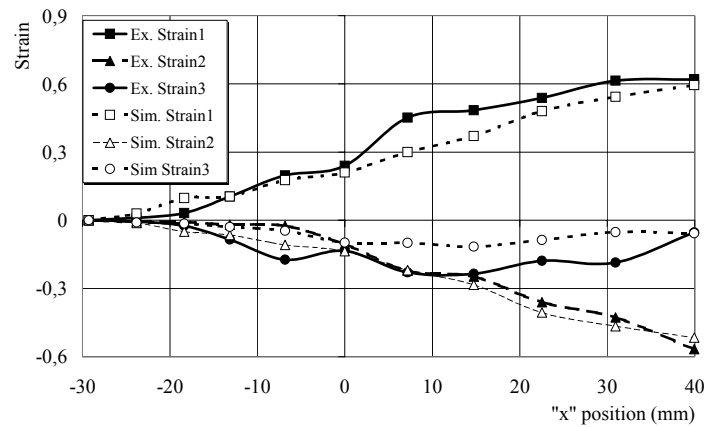


Fig. 10. Comparison of simulated and experimental strain distribution results of a drawing from an initial 170 mm blank in the ear direction

highest blankholder pressure line. The arrows in Figure 12 indicate our axes of measurement, along those axes we measured the dimensions of the deformed circle mesh.

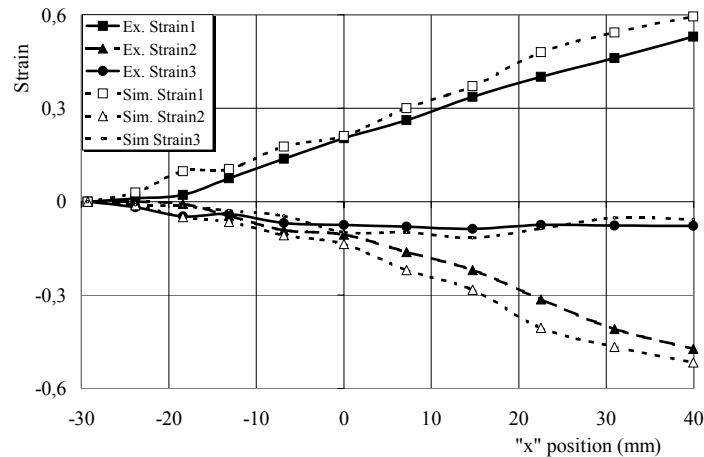


Fig. 11. Comparison of simulated and experimental strain distribution results of a drawing from an initial 170 mm blank in the dip direction

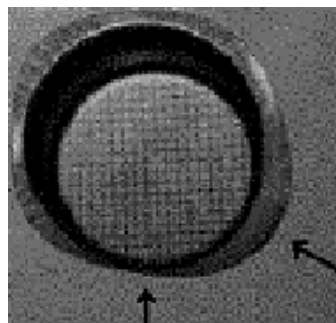


Fig. 12. Specimen used for measuring a non-uniform blankholder pressure cup strain distribution. Arrows indicate the axis of measurement

Generally all of the cups drawn gave evidence that the strain distribution in the direction of the ear is higher than that in the dip direction (Figure 13). This is quite logical in that in the ear direction we have more material because of anisotropic properties of the sheet metal. Cups drawn at applied non-uniform blankholder pressure were seen to have larger strains in the direction of the highest point of the force applied. This is due to the fact that the material is braked by the non-uniform blankholder distribution, resulting in the effect of a larger ear, caused not only by enhanced anisotropic properties but also by the effect of mechanical properties of the hydraulic press.

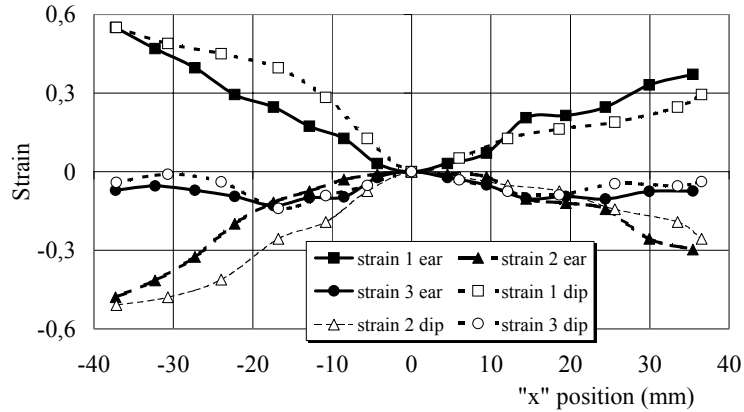


Fig. 13. Strain distribution of a cup with non-uniform blankholder pressure, with initial blank diameter of 170 mm. The right-hand side of the graph represents the area in which a higher blankholder pressure was applied

When we simulated the deep drawing, with an initial 180 mm blank, into a 79 mm cup with uniform blankholder pressure, this simulation stopped at the shown level of drawing. This was due to the fact that LS-DYNA recognized that this blank to drawing ratio exceeded the allowable value, and stopped drawing at this cup height, where we could assume that tearing of the blank took place (Figure 14). The same result was obtained after experimentally verifying the simulation, where the blank tore after having reached about 30 mm into the drawing process. Even after lowering the blankholder pressure and repeating the process the blank tore in the same place every time (refer to Figure 15). This tearing was due to the fact that the drawing ratio was too high for this blank.



Fig. 14. Different views of the simulated drawn cup with the initial blank size of 180 mm

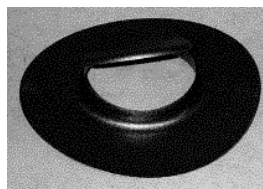


Fig. 15. Deep drawing of a 180 mm blank into a 79 mm cup

For the tailored blank that is subjected to uniform blankholder pressure, the blankholder force was seen to be not uniform. This can be simply explained as follows: since one of the sides of the blank is thinner than the other, we in fact have the effect of a non-uniform blankholder pressure distribution. Now taking a look at the tailored blank experiments more closely, we can see that the orientation or position of the tailored blank affects the outcome of the cup (Figure 16). For example, when the thinner section of the blank was placed in the normal direction of the highest point of non-uniformity pressure, the process went on as if the blank was under uniform blankholder pressure. This is explained by the fact that we actually create a uniform distribution of the cup, and very little wrinkles form. The same cannot be said when placing the thicker section at the highest point. In this case we obtain rigorous wrinkling of the flanges, and the frequency of wrinkles increases more in the thinner section of the blank. This is attributed to the fact that the blank is in a more non-uniform position considering the blankholder pressure applied [1].

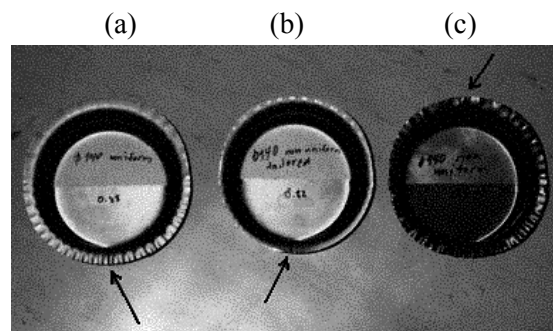


Fig. 16. Cups made from tailored blanks. The arrows indicate the point of the highest blankholder pressure applied. (a) uniform, (b) & (c) non-uniform blankholder pressure

4. Conclusions

Before computer software can be implemented in a commercial deep drawing process it must be rigorously tested and experimentally verified. In this work, we tried to verify this statement. After testing and finding the material properties we inputted the resulting parameters into the DYNAFORM-PC software package. After the simulation calculated the theoretical force curves, we set out to verify these results with the results of experiments. Designing and constructing a forming tool according to the computer model were made, with incorporated measuring devices, to measure the die, punch, blankholder force, and the punch stroke. These measuring devices were first calibrated and then used.

With respect to the tailored blank experiments we found that the placement of the blank in respect of a non-uniform blankholder pressure affects the quality of the drawn cup. When comparing the resulting tailored cups, we can conclude that the optimal re-

sults are obtained when the thinner section of the blank, rather than the thicker one, is placed at the point where the blankholder pressure is the highest (the point at which one of the transfer pins is elongated to produce a higher force than the other pins). This was seen with the introduction of wrinkles on the flanges of the drawings. For the thicker section that was subjected to high blankholder pressure, the thinner side had a higher sinusoidal fluctuation of wrinkles than the thicker side. Otherwise the fluctuation of initiating wrinkles was homogeneous on both sections.

The results obtained from simulations, in comparison to experimental findings, showed that the process forces were higher than the ones found by experiments. The result is very much favoured by industry. All computer simulations of the deep drawing of a cylindrical cup carried out by the DYNAFORM-PC software package showed that after experimental verification the final results obtained were very similar to each other. In other words, we are able to predict flaws or defects that occur with computer simulations before the actual experimental or testing process is initiated. This means that manufacturers can save time and money due to the reduction of floor shop trials and shortened product development time, which in turn increases the product quality.

References

- [1] Kostka P., Cekan P.: *Deep Drawing of a Tailored Blank*, [in:] 6th International Conference FORM '02 Forming Technology, Tools and Machines, 16.9.2002, Brno, pp. 225–230.
- [2] DYNAFORM-PC TRAINING MANUAL (Introduction to the dynaform-PC software) version 1.01, 2001.
- [3] DYNAFORM-PC USERS MANUAL (A pre-processor compatible with LS DYNA/PC), Version 1.0, 1999.
- [4] Tschatsch H.: *Handbuch Umformen*, Hoppensedt Technik Tabellen Verlag, 1993.
- [5] Lange K.: *Umformtechnik, Handbuch für Industrie und Wissenschaft*, Band 3, *Blechbearbeitung*, Springer-Verlag, 1990.
- [6] Siebel E.: *Der Niederhalttdruck beim Tiefziehen*, Stahl Eisen 1954, 74, pp. 155–158.
- [7] *Metal Forming Handbook/Schuller*, Library of Congress Cataloguing-in-Publication Data, Springer-Verlag, Berlin–Heidelberg, 1998.

Symulacja niejednorodności w procesach głębokiego tłoczenia

Współczesna koncepcja projektowania procesów głębokiego tłoczenia wyrobów oznacza inne spojrzenie na zastosowanie dociskacza. Podczas procesów tłoczenia złożonych wyrobów należy kontrolować niejednorodne płynięcie materiału między stemplem a matrycą, aby wyeliminować niepożądane fałdowanie i tworzenie się uszu w wytłoczonym wyrobie. Można to osiągnąć, dopasowując siły wywierane przez kształtowaną blachę na dociskacz. Gdy nacisk wywierany przez dociskacza jest niejednorodny zaawansowane programy komputerowe, określające wzajemne oddziaływanie dociskacza i wyrobu, pozwalają korzystnie zaprojektować proces tłoczenia. Opisano niektóre wyniki symulacji i eksperymentalnie zweryfikowano narzędzia, uwzględniając możliwość kontroli nacisku wywieranego przez dociskacz.



Approximation technique for the Bezier curves in numerical analysis of photoelastic experiment

A. SMYKLA

Rzeszów University of Technology, 35-959 Rzeszów, ul. Wincentego Pola 2, Department of Computer Science

The paper presents the mutation of standard local interpolation of a sequence of points by the Bezier segments. This method is applied in photoelastic experiment, but can be used in any approximation where the data are distributed sparsely. Finally the results of approximation of photoelastic experiment to be assessed in FEM calculations have been presented.

Keywords: *Bezier curves, photoelastic, approximation, FEM*

1. Introduction

In stress analysis by means of photoelastic models, an important role of complex structures in the design is assumed. Employing analytical (or numerical) solutions alone during the design phase can lead to errors in predicting actual stress concentrations, hence safety factors might be miscalculated. Photoelastic model analysis is usually performed during the very early stages of a product or structures. Observation and analysis of the stress pattern in a photoelastic model are made with a polariscope. As a result of photoelastic experiment a picture with fringe pattern has been obtained. The picture is often used for estimating qualitatively the stress concentrations in the structures. It enables a qualitative comparison of photoelastic analysis and numerical calculation (for instance, FEM). This relationship can be defined as follows:

$$N_{\text{theoret.}} = \frac{\sigma_1 - \sigma_2}{K_\sigma}, \quad (1)$$

where:

- σ_1, σ_2 – principal stresses,
- K_σ – material constant,
- N – fringe count.

To compare the results it is necessary to specify fringe count in the whole structure under investigation. This can be done by the method presented below.

In the first step, integer fringe count is interpolated using interactive picture processing. A simple way to do this is to draw the Bezier curves of integer fringe count

using graphic program (for example, CorelDraw) and to write each of them in a separate PostScript text file [1], [2]. The PostScript file contains the description of the control Bezier points. For example, the description of one Bezier curve (in PostScript language [3]) is defined as:

```
276.9120 649.7280 m
```

```
259.8480 660.2400 235.7280 647.4240 224.3520 634.5360 c
```

It corresponds to curve where locations of control points are as follows:

$W1x = 276.9120,$

$W1y = 649.7280,$

$W2x = 259.8480,$

$W2y = 660.2400,$

$W3x = 235.7280,$

$W3y = 647.4240,$

$W4x = 224.3520,$

$W4y = 634.5360.$

A graphical representation of this curve is given in Figure 1.

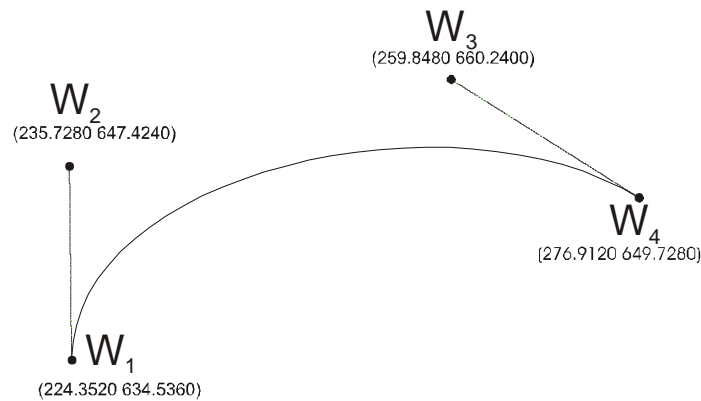


Fig. 1. Control points of the Bezier curve

Equation (2) of Bazier curve is:

$$\mathbf{B}(t) = (1-t)^3 \mathbf{W1} + 3t(1-t)^2 \mathbf{W2} + 3t^2(1-t) \mathbf{W3} + t^3 \mathbf{W4}, \quad (2)$$

where

$$W1=[W1x \ W1y]^T, \ W2=[W2x \ W2y]^T, \ W3=[W3x \ W3y]^T, \ W4=[\ W4x \ W4y]^T, \ t \in [0, 1].$$

Let us consider a plate with hole whose dimensions are given in Figure 2.

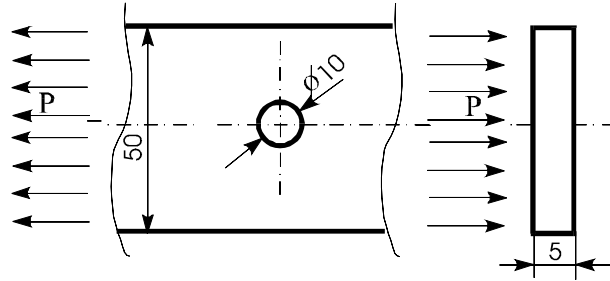


Fig. 2. Dimensions of a plate with a hole. Preferred parameters for the material are:
 $P = 170$ [daN] and $\nu = 0.42$ [-]

The model was made of resin (Epidian 5). The picture of fringe pattern in critical cross-section is presented in Figure 3.

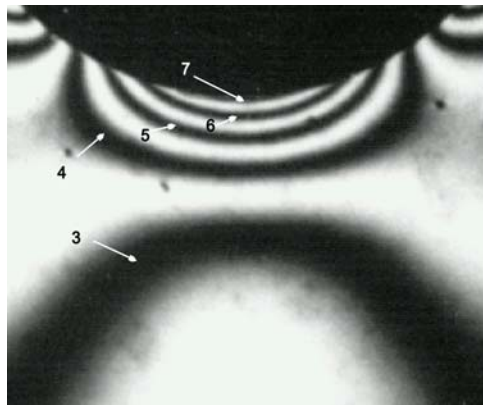


Fig. 3. Fringe pattern around a hole

The corresponding collection of the Bezier curves of integer fringe pattern is presented in Figure 4.

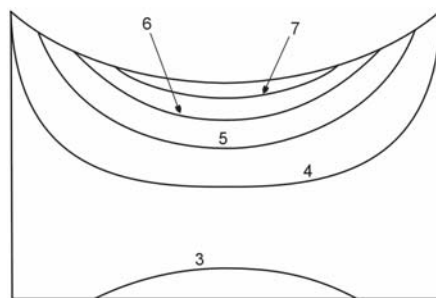


Fig. 4. A collection of the Bezier curves around a hole

A real fringe pattern in any cross-section can be also obtained by interpolation of the Bezier curve. This method is discussed below.

2. Approximation technique

The method proposed leads to a piecewise smooth G^1 Bezier curve, which consists of cubical parabolas designed so as to pass through adjacent points and are tangents to the surface at those points (in exceptional cases in the vicinity of inflections). To obtain uniform representation of the result, as piecewise cubic curve, degree elevation has been applied to all parabolic segments. All tangent directions missing in this group of interpolation methods must be somehow estimated. In this case, they are defined (at the internal points) by the chord joining the previous and the next points. As result, the method applies to the points dense enough to provide a sensible estimation of the tangent direction by the chord.

We intend to construct a “smooth” Bezier curve passing through the given points

$$\mathbf{W}_1(x_1, y_1), \mathbf{W}_2(x_2, y_2), \dots, \mathbf{W}_n(x_n, y_n).$$

If we assume that the nodes are ordered:

$$a = x_1 < x_2 < \dots < x_n = b,$$

then we can represent the desired curve by a spline function B , where $B_i(x)$ is composed of the Bezier B_i for $x \in [x_i, x_{i+1}]$. These B are defined differently in each subinterval and must satisfy certain connecting conditions at the nodes.

To solve this problem we use an adequate geometrical dependence. Therefore the following three cases should be considered:

1. Nodes are the first or the last in the data set (W_1 and W_n).
2. Nodes $W_{n-1} \dots W_{n+2}$ create convex figure.
3. Nodes $W_{n-1} \dots W_{n+2}$ do not create convex figure.

In order to define each curve, equation representing four control Bezier points must be written. Each case is presented in a separate illustration.

The first case is shown in Figure 5.

Node W_1 is the end point. W_1, W_2, W_3 are interpolation points.

k_2 is a straight line, where $W_2 \in k_2$ and $k_2 \perp \overline{W_1W_3}$.

$k_{1,2}^{\text{pr}}$ is midperpendicular to $\overline{W_1W_2}$.

S_1 is the intersection of $k_{1,2}^{\text{pr}}$ and k_2 .

$P2_1$ is the central point of $\overline{W_1S_1}$.

$P3_1$ is the central point of $\overline{W_2S_1}$.

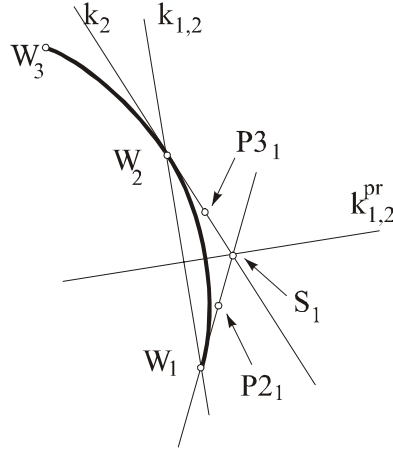


Fig. 5. Geometrical construction of curve ends

According to a geometrical dependence this can be written in the form:

$$k_2 \rightarrow y = \frac{Wy_3 - Wy_1}{Wx_3 - Wx_1} x + Wy_2 - \frac{Wx_2(-Wy_1 + Wy_3)}{Wx_3 - Wx_1}, \quad (3)$$

$$k_{1,2} \rightarrow y = \frac{Wy_2 - Wy_1}{Wx_2 - Wx_1} x + Wy_2 - \frac{Wx_2(-Wy_1 + Wy_2)}{Wx_2 - Wx_1}. \quad (4)$$

Because the coordinates of $k_{1,2}^{pr}$ are $((Wx_2 + Wx_1)/2, (Wy_2 + Wy_1)/2)$, then we can write:

$$k_{1,2}^{pr} \rightarrow y = \frac{(-Wy_1 + Wy_2)}{-Wx_1 + Wx_2} + \frac{Wy_1 + Wy_2}{2} + \frac{(Wx_1 + Wx_2)(-Wy_1 + Wy_2)}{2(-Wx_1 + Wx_2)}. \quad (5)$$

Intersection of straight lines can be find by solving the system of Equations (4), (5):

$$Sx_1 = \frac{\frac{-Wy_2 - Wy_1}{2} + Wy_2 - \frac{(-Wx_1 + Wx_2)(Wx_1 + Wx_2)}{2(-Wy_1 + Wy_2)} - \frac{Wx_2(-Wy_1 + Wy_3)}{-Wx_1 + Wx_3}}{\frac{-Wx_1 + Wx_2}{-Wy_1 + Wy_2} + \frac{-Wy_1 + Wy_3}{-Wx_1 + Wx_3}}, \quad (6)$$

$$S y_1 = \frac{(-W x_1 + W x_2)(W x_1 + W x_2)}{2(-W y_1 + W y_2)} + \frac{W y_1 + W y_2}{2} - \frac{(-W x_1 + W x_2) \left(\frac{-W y_1 - W y_2}{2} + W y_2 - \frac{(-W x_1 + W x_2)(W x_1 + W x_2)}{2(-W y_1 + W y_2)} - \frac{W x_2(-W y_1 + W y_3)}{-W x_1 + W x_3} \right)}{(-W y_1 + W y_2) \left(\frac{-W x_1 + W x_2}{-W y_1 + W y_2} + \frac{-W y_1 + W y_3}{-W x_1 + W x_3} \right)}. \quad (7)$$

In this way, we found the coordinates of control points, where independent variables were only coordinates of interpolated points:

$$\begin{aligned} P1x_1 &= Wx_1, \\ P1y_1 &= Wy_1, \\ P2x_1 &= (Wx_1 + Sx_1)/2, \\ P2y_1 &= (Wy_1 + Sy_1)/2, \\ P3x_1 &= (Wx_2 + Sx_1)/2, \\ P3y_1 &= (Wy_2 + Sy_1)/2, \\ P4x_1 &= Wx_2, \\ P4y_1 &= Wy_2. \end{aligned} \quad (8)$$

The second case is given in Figure 6.

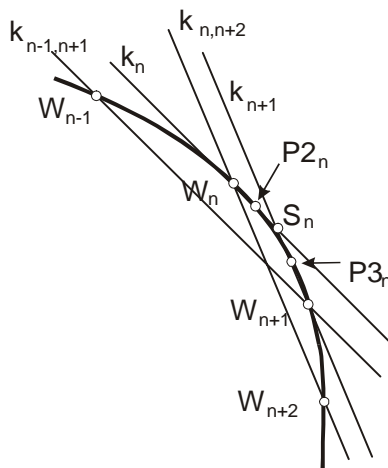


Fig. 6. Geometrical construction of the second case

W_{n-1}, \dots, W_{n+2} – interpolation points.

$k_{n-1, n+1} - k_{n-1, n+1} \subset W_{n-1}$ and $k_{n-1, n+1} \subset W_{n+1}$,

k_n – straight line, where $k_n \parallel k_{n-1, n+1}$ and $k_n \subset W_{n-1}$,

$k_{n,n+2}$ – straight line, where $k_{n,n+2} \subset W_n$ and $k_{n,n+2} \subset W_{n+2}$.

k_{n+1} – straight line, where $k_{n+1} \perp k_{n,n+2}$ and $k_n \subset W_{n+1}$.

S_n – point, where $S_n = k_n \cap k_{n+1}$

$P2_n$ – midpoint of $\overline{W_n S_n}$.

$P3_n$ – midpoint of $\overline{W_{n+1} S_n}$.

According to the geometrical dependence, we arrive at:

$$k_n \rightarrow y = \frac{Wy_{n-1} - Wy_{n+1}}{Wx_{n-1} - Wx_{n+1}}x + Wy_n - \frac{Wx_n(Wy_{n-1} - Wy_{n+1})}{Wx_{n-1} - Wx_{n+1}}, \quad (9)$$

$$k_{n+1} \rightarrow y = \frac{Wy_n - Wy_{n+2}}{Wx_n - Wx_{n+2}}x + Wy_{n+1} - \frac{Wx_{n+1}(Wy_n - Wy_{n+2})}{Wx_n - Wx_{n+2}}. \quad (10)$$

Intersection of straight lines can be found by solving the system of Equations (9), (10):

$$Sx_n = \frac{Wy_n - \frac{Wx_n(Wy_{n-1} - Wy_{n+1})}{Wx_{n-1} - Wx_{n+1}} - Wy_{n+1} + \frac{Wx_{n+1}(Wy_n - Wy_{n+2})}{Wx_n - Wx_{n+2}}}{\frac{Wy_{n-1} - Wy_{n+1}}{Wx_{n-1} - Wx_{n+1}} - \frac{Wy_n - Wy_{n+2}}{Wx_n - Wx_{n+2}}}, \quad (11)$$

$$Sy_n = -\frac{Wx_{n+1}(Wy_{n-1} - Wy_{n+1})}{(Wx_{n-1} - Wx_{n+1})} + Wy_{n+1} - \frac{(Wy_{n-1} - Wy_{n+1}) \left(Wy_n - \frac{Wx_n(Wy_{n-1} - Wy_{n+1})}{Wx_{n-1} - Wx_{n+1}} - Wy_{n+1} + \frac{Wx_{n+1}(Wy_n - Wy_{n+2})}{Wx_n - Wx_{n+2}} \right)}{(Wx_{n-1} - Wx_{n+1}) \left(\frac{Wy_{n-1} - Wy_{n+1}}{Wx_{n-1} - Wx_{n+1}} - \frac{Wy_n - Wy_{n+2}}{Wx_n - Wx_{n+2}} \right)}. \quad (12)$$

Then we found the coordinates of the control points:

$$\begin{aligned} P1x_n &= Wx_n, \\ P1y_n &= Wy_n, \\ P2x_n &= (Wx_n + Sx_n)/2, \\ P2y_n &= (Wy_n + Sy_n)/2, \\ P3x_n &= (Wx_{n+1} + Sx_n)/2, \\ P3y_n &= (Wy_{n+1} + Sy_n)/2, \\ P4x_n &= Wx_{n+1}, \\ P4y_n &= Wy_{n+1}. \end{aligned} \quad (13)$$

The third case is presented in Figure 7.

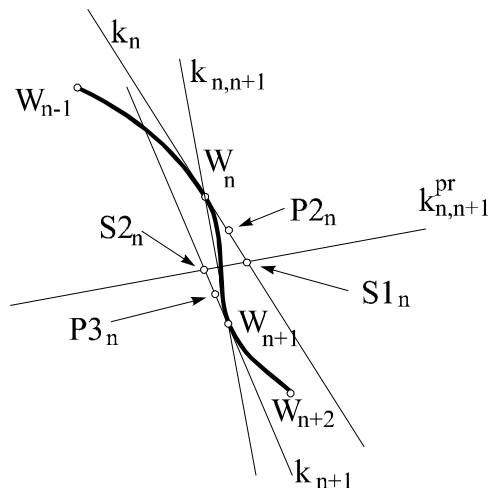


Fig. 7. Geometrical construction of the third case

W_{n-1}, \dots, W_{n+2} – interpolation points.

k_n, k_{n+1} – straight line the same as in the second case.

$k_{n,n+1}$ – straight line, where $k_{n,n+1} \subset W_n$ and $k_{n,n+1} \subset W_{n+1}$.

$k_{n,n+1}^{pr}$ – midperpendicular $\overline{W_{n+1}W_n}$.

$S1_n = k_{n,n+1}^{pr} \cap k_n$.

$S2_n = k_{n,n+1}^{pr} \cap k_{n+1}$.

$P2_n = \overline{W_n S1_n}$.

$P3_n$ – midpoint of $\overline{W_{n+1} S2_n}$.

According to the geometrical dependence the following relation can be obtained:

$$k_{n,n+1} \rightarrow y = \frac{Wy_n - Wy_{n+1}}{Wx_n - Wx_{n+1}}x + Wy_n - \frac{Wx_n(Wy_n - Wy_{n+1})}{Wx_n - Wx_{n+1}} \quad (14)$$

and perpendicular straight line

$$k_{n,n+1}^{pr} \rightarrow y = \frac{Wx_n - Wx_{n+1}}{Wy_n - Wy_{n+1}}x + \frac{Wy_n + Wy_{n+1}}{2} - \frac{(Wx_n - Wx_{n+1})(Wx_n - Wx_{n+1})}{2(Wy_n - Wy_{n+1})}. \quad (15)$$

The point $S2_n$ can be find by solving the system of Equations (9) and (15), and the point $S3_n$ by solving Equations (10) and (15):

$$S1x_n = \frac{-Wy_n - \frac{(Wx_n - Wx_{n+1})(Wx_n + Wx_{n+1})}{2(Wy_n - Wy_{n+1})} + \frac{Wy_n + Wy_{n+1}}{2} + \frac{Wx_n(Wy_{n-1} - Wy_{n+1})}{Wx_{n-1} - Wx_{n+1}}}{-\frac{Wx_n - Wx_{n+1}}{Wy_n - Wy_{n+1}} - \frac{Wy_{n-1} - Wy_{n+1}}{Wx_{n-1} - Wx_{n+1}}}, \quad (16)$$

$$S1y_n = -\frac{Wx_n(Wy_{n-1} - Wy_{n+1})}{(Wx_{n-1} - Wx_{n+1})} + Wy_n \\ - \frac{(Wy_{n-1} - Wy_{n+1}) \left(Wy_n - \frac{(Wx_n - Wx_{n+1})(Wx_n + Wx_{n+1})}{2(Wy_n - Wy_{n+1})} + \frac{Wy_n + Wy_{n+1}}{2} + \frac{Wx_n(Wy_{n-1} - Wy_{n+1})}{Wx_{n-1} - Wx_{n+1}} \right)}{(Wx_{n-1} - Wx_{n+1}) \left(\frac{Wy_{n-1} - Wy_{n+1}}{Wx_{n-1} - Wx_{n+1}} - \frac{Wy_n - Wy_{n+2}}{Wx_n - Wx_{n+2}} \right)}, \quad (17)$$

$$S1x_n = -\frac{-Wy_{n+1} - \frac{(Wx_n - Wx_{n+1})(Wx_n + Wx_{n+1})}{2(Wy_n - Wy_{n+1})} + \frac{Wy_n + Wy_{n+1}}{2} + \frac{Wx_{n+1}(Wy_n - Wy_{n+2})}{Wx_n - Wx_{n+2}}}{-\frac{Wx_n - Wx_{n+1}}{Wy_n - Wy_{n+1}} - \frac{Wy_{n-1} - Wy_{n+2}}{Wx_{n-1} - Wx_{n+2}}}, \quad (18)$$

$$S1y_n = -\frac{Wx_{n+1}(Wy_n - Wy_{n+2})}{(Wx_n - Wx_{n+2})} + Wy_{n+1} \\ + \frac{(Wy_n - Wy_{n+2}) \left(-Wy_{n+1} - \frac{(Wx_n - Wx_{n+1})(Wx_n + Wx_{n+1})}{2(Wy_n - Wy_{n+1})} + \frac{Wy_n + Wy_{n+1}}{2} + \frac{Wx_{n+1}(Wy_n - Wy_{n+2})}{Wx_n - Wx_{n+2}} \right)}{(Wx_n - Wx_{n+2}) \left(\frac{Wx_n - Wx_{n+1}}{Wy_n - Wy_{n+1}} - \frac{Wy_n - Wy_{n+2}}{Wx_n - Wx_{n+2}} \right)}. \quad (19)$$

Then we found the coordinates of the control points:

$$\begin{aligned} P1x_n &= Wx_n, \\ P1y_n &= Wy_n, \\ P2x_n &= (Wx_n + S1x_n)/2, \\ P2y_n &= (Wy_n + S1y_n)/2, \\ P3x_n &= (Wx_{n+1} + S2x_n)/2, \\ P3y_n &= (Wy_{n+1} + S2y_n)/2, \\ P4x_n &= Wx_{n+1}, \\ P4y_n &= Wy_{n+1}. \end{aligned} \quad (20)$$

The fourth case.

All points are collinear.

The coordinates of control points:

$$\begin{aligned}
 P1x_n &= Wx_n, \\
 P1y_n &= Wy_n, \\
 P2x_n &= (Wx_n + Wx_{n+1})/2, \\
 P2y_n &= (Wy_n + Wy_{n+1})/2, \\
 P3x_n &= P2x_n, \\
 P3y_n &= P2y_n, \\
 P4x_n &= Wx_{n+1}, \\
 P4y_n &= Wy_{n+1}.
 \end{aligned} \tag{21}$$

By using this method the chart of fringe pattern can be drawn in any cross-section and fractional fringe count can be obtained. As an example, the interpolation of the central vertical cross-section is presented in Figure 8.

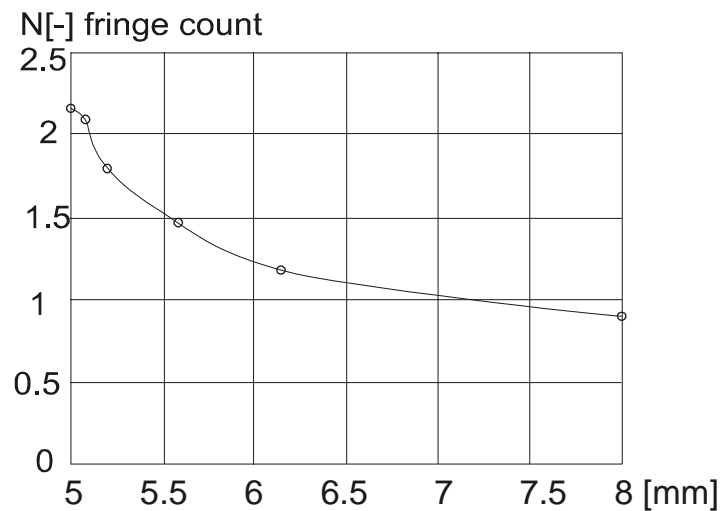


Fig. 8. Interpolation of the central vertical cross-section obtained by using the method presented

3. Comparison of the results

We can make a practical use of the method presented comparing photoelastic analysis with numerical calculations. The result of FEM numerical calculations of this model is presented in Figure 9.

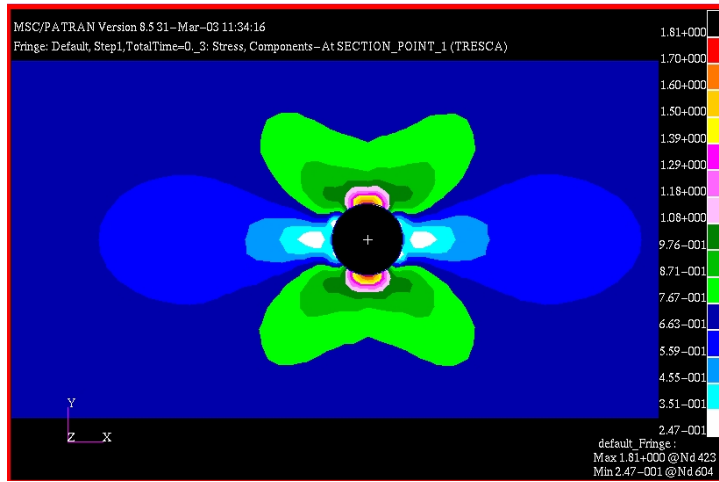


Fig. 9. The result of FEM numerical calculations

After this step we can compare each result on singular chart (Figure 10).

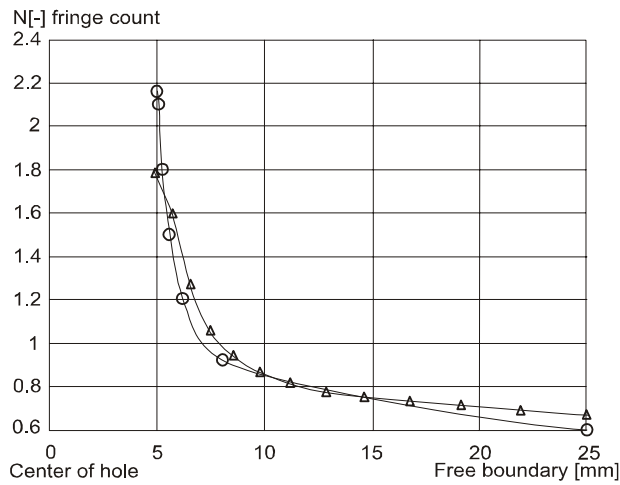


Fig. 10. Comparison of results of FEM numerical calculations (triangle) with the Bezier interpolation (circle)

4. Final remarks

The method presented can be used for interpolation where some of data are placed rarely.

1. The curves (splines) calculated are smooth and could be used not only in photoelastic analysis.

2. It is possible to adapt this method for quality estimation in FEM calculations.
3. PostScript file is useful in moving information on coordinates (the Bezier curves, line). It is easy to write a program for processing PostScript file.
4. Interpolation methods of this type proved to be useful in simple applications, because they are local, which means that they do not require solution of any set of 0 (number of interpolated points) equations.

References

- [1] Smykla A.: *Tworzenie rozwinięć brył wypukłych*, Prace V Sympozjum *Mikrokomputery w edukacji*, Polana Chochołowska, 1995.
- [2] Smykla A.: *Zastosowanie systemu komputerowego w wyznaczaniu parametru izochromy na podstawie zdjęć elastoptycznych*, Zeszyty naukowe Wyższej Szkoły Informatyki i Zarządzania w Rzeszowie, 1998, nr 7.
- [3] Spring B.M., Dubin D.: *PostScript od A do Z*, INTERSOFLAND, Warszawa, 1992.
- [4] Farin G.: *Curves and Surfaces for Computer Aided Geometric Design – a practical guide*, third edition, 1988, Academic Press, Inc.

Przybliżona technika zastosowania krzywej Beziery w numerycznej analizie fotoelastycznego eksperymentu

W pracy przedstawiono oryginalną przybliżoną technikę zastosowania krzywej Beziery. Metoda ta została zastosowana do analizy eksperymentu fotoelastycznego. Może ona być również służyć do dowolnego przybliżenia wyników eksperymentu, gdy są one rozmieszczone z dużymi odstępami. Przedstawiono wyniki przybliżenia eksperymentu fotoelastycznego oszacowane metodą elementów skończonych



The effect of subterranean exploitation of mines on the state of stress and displacements of transport embankments

ELŻBIETA STILGER-SZYDŁO, WALDEMAR TUTAJ

Technical University of Wrocław, Wybrzeże Wyspiańskiego 27, 50-370 Wrocław

This study presents the theoretical bases and the concepts of modelling the interaction between embankment and mining subsoil and predicting its deformations. These bases and concepts mainly focus on examining the mining tension strains and on the safe operation of road constructions. Some solutions (by employing MES) in the flat and spatial state of strain, including a change in location of the exploitation front with respect to the axis of the embankment, were presented.

Keywords: *mining subsoil, embankments, stress, displacements*

1. Introduction

Recently a number of large-scale projects have been carried out in the field of land transport infrastructure engineering with regard to motorways, roads and bridges as well as accompanying facilities. The construction is often located in the areas that used to be exploited for industrial purposes and are characterized by complex geotechnical conditions. The construction of motorways in mining areas requiring special protection against mining deformations is a new and complex issue. The subterranean exploitation of mines has a negative impact on the surface and the structures erected on it. This impact manifests itself in the change in water relations, displacements of an orogen and its tremors causing vibrations in subsoil.

What still remains an open question is the interaction of a transport earthen structure with a subsoil in mining areas. There are no official regulations and guidelines for design of earthen structures (slopes, embankments and earth dams) and their protection against mining deformations. So far no complex approach to the design of embankments in mining areas in accordance with bearing capacity and limit states has been developed. Mining effects are especially dangerous with respect to tension strains (in the convex part of the subsiding trough), which causes ravelling of both subsoil and embankment. As a result, this leads to non-uniform settlements of the embankment top, local subsidence as well as horizontal displacements of roadways, and ultimately to safety-threatening the local earth slides and damage to surface. The current problem is the settlement of motorway embankment due to ravelling of a subsoil in the mining area.

This study presents the theoretical bases as well as the concepts of: a) modelling the interaction between an embankment and a mining subsoil and b) predicting its de-

formations. They mainly focus on examining the mining tension strains and on the safe operation of road constructions. Some solutions (by employing MES) in the flat and spatial state of strain, including a change in location of the exploitation front with respect to the axis of the embankment, were presented.

2. Mining-area deformations of the surface

The paper deals with continuous deformations of the surface. As a result of the exploitation of mines, the so-called subsiding trough is formed on the surface. It is characterized in its every point by: settlement, slope, curvature and soil horizontal strain (Figure 1).

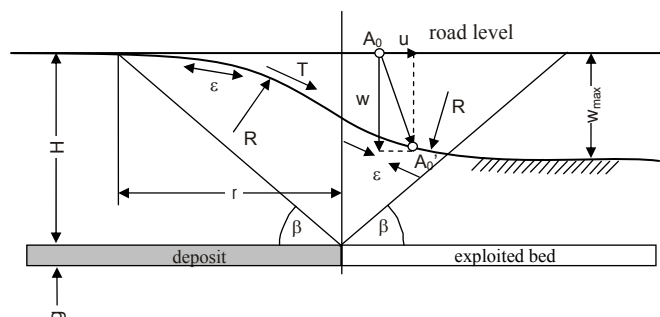


Fig. 1. Model of established subsiding trough – profile of vertical displacements: w – vertical displacement, T – slope, R – radius of curvature, ε – horizontal strain, H – depth of exploited bed, g – thickness of exploited bed, β – angle of the range of mining effects, r – radius of the range of principal effects

The theories of orogenesis are based on geometric models defining a vectorial displacement field of orogen seen as a continuous medium. In practice, the most frequently applied theory is that of Budryk-Knothe [2], [5], [6]. Extreme values of the indexes of area deformation determine the category of the deformation of a mining area in which it is placed (Table 1).

Table 1. Categories of deformations of mining area

Categories	Boundary values of the indexes of area deformation		
	T [mm/m]	R [km]	ε [mm/m]
0	$T \leq 0.5$	$ R \geq 40$	$ \varepsilon \leq 0.3$
I	$0.5 < T \leq 2.5$	$40 > R \geq 20$	$0.3 < \varepsilon \leq 1.5$
II	$2.5 < T \leq 5$	$20 > R \geq 12$	$1.5 < \varepsilon \leq 3$
III	$5 < T \leq 10$	$12 > R \geq 6$	$3 < \varepsilon \leq 6$
IV	$10 < T \leq 15$	$6 > R \geq 4$	$6 < \varepsilon \leq 9$
V	$T > 15$	$ R < 4$	$ \varepsilon > 9$

3. Development of methods of defining the interaction between a structure and the subsoil in mining area

Difficulties arise when one attempts to formulate mathematical models for the subsoil in mining area. In the past, the model of a rigid body for the structure and soil was adopted, then – that of an elastic body for the structure and Winkler's model as well as the elastic half-plane model for the soil. Currently, in order to define the processes occurring in the structure and its foundation, the models of the ground medium mechanics, i.e. elastoplastic models, are used. The existing computer software packages developed with a view of their application in geotechnics, based on the finite element method, define the soil medium by dint of the linear-elastic-perfectly-plastic constitutive model.

It is impossible to perform a theoretical analysis of the above-mentioned issues without a continuous improvement of experimental research. The interpretation of the results of numerous field and laboratory tests on cohesive and cohesionless soil, employing the methods of structural soil mechanics, constituted the basis for presenting empirical dependencies determining the reduction in the strength parameters of soil that was subject to the process of ravelling [4], [7]. Above all, the reduction concerned soil cohesion, because its internal friction angle virtually remained stable. The following dependence allows defining the changes in soil cohesion occurring during the process of its ravelling

$$c_R = c_0 \cdot \left(1 - \frac{\varepsilon_R}{\alpha_R + \varepsilon_R} \right) + c_{kr} \cdot \frac{\varepsilon_R}{\alpha_R + \varepsilon_R}, \quad (1)$$

where:

- c_0 – standard soil cohesion (if $\varepsilon_R = 0$);
- c_R – reduced soil cohesion (if $\varepsilon_R > 0$);
- c_{kr} – critical cohesion when a decrease in soil resistance is stabilized;
- α_R – coefficient marking out cohesion reduction (when ravelling of “infirm” made ground $\alpha_R < 1.5$);
- ε_R – horizontal ravelling strain.

The research conducted reveals that there is a substantial influence of horizontal strains on the change of cohesive soil strength parameters. For instance, in silt clays, in the case of horizontal strains ε_R of the order of 3–10 mm/m, a decrease in cohesion totalled from 20 up to 45% of its value determined prior to soil ravelling, whereas cohesionless soil shear strength subject to ravelling ($\varepsilon_R \leq \varepsilon_{R(kr)}$) virtually remained stable.

4. Assessment of stability and bearing capacity of embankment

The assessment of slope and stability constitutes a more complex issue. It results not only from the difficulties that arise while determining the parameters characterizing the slope (physical, strength, geometric), but also from the adopted methods of calculation. While analyzing how an earthen structure is associated with soil medium of mining area we are interested in the boundary value of horizontal ravelling strain, whose exceeding will result in the occurrence of limit equilibrium state of stresses.

An overview of the assessment methods of slope stability of an earthen structure on the mining-area foundation as well as the analysis of the results of calculations have been presented in the authors' previous works [9], [10], in which boundary strain values (ε_n) for embankment soil have been compared with boundary strain values (ε_p) for subsoil, with respect to the predicted strains in mining area. It has been concluded that the block methods used in engineering are ineffective while assessing the embankment stability and that the Finite Element Method's numerical analyses are of a great use. They allow determining simultaneously both the bearing capacity and the strain of an earthen structure (in the flat and spatial state of strain). The obtained patterns for the embankment bearing capacity loss are perfectly consistent with those of block method of stability assessment presented by Kezdi. The method posits that the slope block is displaced along the floor of a weaker layer. This pattern of the slope devastation can be employed when $\varepsilon_n > \varepsilon_p$. The sliding-down force is the active pressure from the embankment body, and the holding forces – possible passive pressure from the footing and friction force acting in the foundation of the soil medium body (Figure 2).

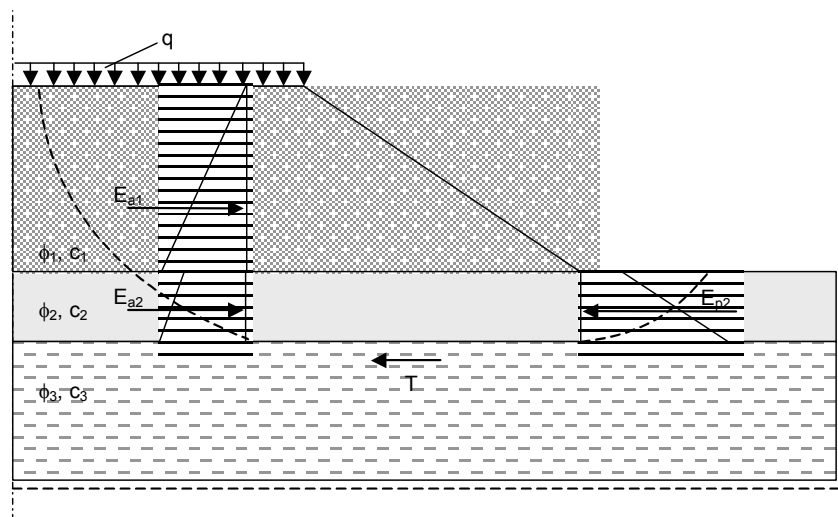


Fig. 2. Design method of stability assessment for embankment built on a soil of low bearing capacity, in accordance with Kezdi's method

The embankment stability coefficient is determined based on the dependence:

$$F = \frac{T + E_{p2}}{E_{a1} + E_{a2}}, \quad (2)$$

where:

T – horizontal shear resistance of weak layer floor;

E_{a1} – active pressure in embankment;

E_{a2} – active pressure in weak layer;

E_{p2} – passive pressure in weak layer.

Figure 3 illustrates the dependence of the stability coefficient value (Equation (2)) on the diversified soil geotechnical parameter values (for the embankment soil it is an internal friction angle equalling the angle of its slope).

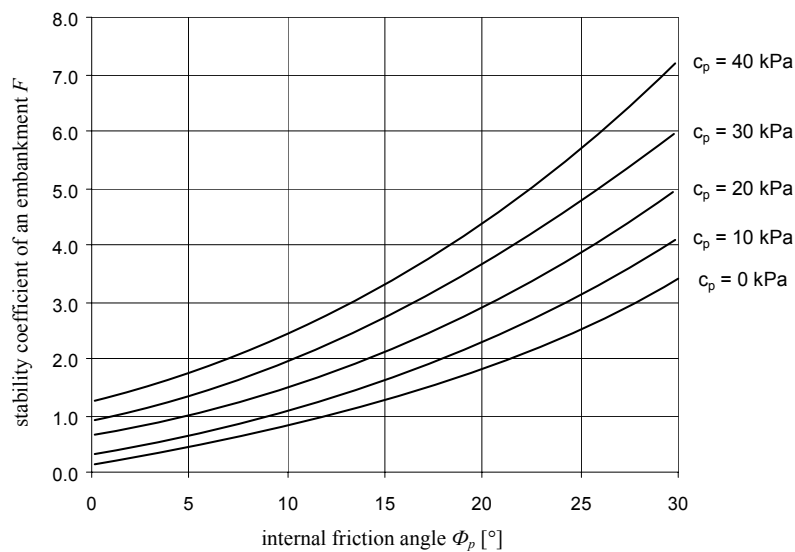


Fig. 3. Stability coefficient value versus diversified subsoil geotechnical parameter values

Comparative analyses with MES methods showed that the above-mentioned method of the slope stability loss fits the method of devastation of embankment built on a subsoil in mining area. In the solutions obtained it coincides with the maximum plastic strain zone in the slope, clearly marking out a triangular area near the slope. The impact of mining area should be accounted for in the Kezdi's method by reducing cohesion and changing the value of pressure dependent on horizontal strain.

5. Embankment strength analysis with Finite Element Method

The numerical analysis with the Finite Element Method (MES) is the most general method allowing us to determine bearing capacity and – at the same time – the strain of an earthen structure [1], [8]. Examples of the available geotechnics-oriented MES computer programs include HYDRO-GEO, PLAXIS and Z_SOIL. Although they allow a number of limitations, such as carrying out analysis only in the flat state of strain or in axial symmetry as well as no possibility of changing the material model, they fulfil their function for engineering purposes. In addition to that, there are some general programs, such as COSMOS and ABAQUS, based on an advanced finite element method. Their rich library of material models and finite elements and the possibility of analysing spatial problems make them widely applicable to the analyses of stress and displacement in numerous problems of static and dynamic mechanics. However, the resulting problem is laborious data input and a huge computing power required. While analysing geotechnical constructions with the ABAQUS program, the most commonly applied soil constitutive models are those of Coulomb–Mohr and of modified Drucker–Prager.

Coulomb–Mohr's condition of strength posits devastation by maximum tangential stress dependent on normal stress:

$$\tau = c - \sigma \tan \phi, \quad (3)$$

where:

τ – tangential stress;

σ – normal stress (negative on compression).

On the plane, this condition is represented by a straight line tangent to Mohr's circles, determined on the basis of the maximum and minimum principal stresses (Figure 4).

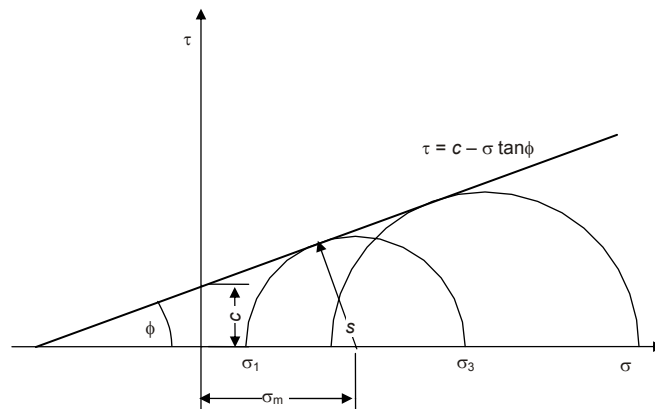


Fig. 4. Coulomb-Mohr's model in system of stresses:

$$\tau = s \cos \phi; \quad \sigma = \sigma_m + s \sin \phi; \quad s = 1/2(\sigma_1 - \sigma_3); \quad \sigma_m = 1/2(\sigma_1 + \sigma_3)$$

In the space of principal stress, Coulomb-Mohr's condition is expressed by

$$\sigma_1 - \sigma_3 + \sin \phi (\sigma_1 + \sigma_3) - 2c \cos \phi = 0. \quad (4)$$

Drucker-Prager's model used in the ABAQUS system undergoes a number of modifications. Due to these modifications the surface of plasticity assumes complex shapes, allowing us to simulate an actual behaviour of various materials, and only in a special case it assumes the shape of a classic Drucker-Prager's surface [3].

The modified Drucker-Prager's model takes into account three conditions of plasticity, which differ from each other in terms of the shape of plasticity surface in the meridional plane (the invariants p and q), assuming linear, hyperbolic or exponential shape.

The choice of a right model depends on the type of material, available experimental data of the model's calibrated parameters and the range of stress pressure that will be exerted on the material.

The Drucker-Prager's linear model is defined as the condition of plasticity with three invariants of stress (Figure 5):

$$F = t - p \tan \beta - d = 0, \quad (5)$$

where:

$$t = \frac{1}{2}q \left[1 + \frac{1}{K} - \left(1 - \frac{1}{K} \right) \left(\frac{r}{q} \right)^3 \right], \quad (6)$$

β – the slope of the linear surface of plasticity in the plane $p-t$, related to an angle of internal friction of material;

d – the material cohesion;

K – the ratio of plasticizing stresses in triaxial tension to plasticizing stresses in triaxial compression.

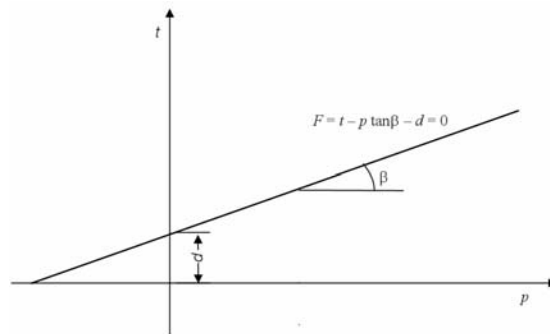


Fig. 5. Drucker-Prager's linear condition

The material cohesion d is related to the initial data:

- with reinforcement defined by plasticizing compressive stresses σ_c :

$$d = \left(1 - \frac{1}{3} \tan \beta\right) \sigma_c; \quad (7)$$

- with reinforcement defined by plasticizing tension stresses σ_t :

$$d = \left(\frac{1}{K} + \frac{1}{3} \tan \beta\right) \sigma_t; \quad (8)$$

- with reinforcement defined by plasticizing shear stresses τ :

$$d = \frac{\sqrt{3}}{2} \tau \left(1 + \frac{1}{K}\right). \quad (9)$$

The shape of plasticity surface in the deviator plane is influenced by the coefficient K , having the value of $0.778 \leq K \leq 1.0$ (Figure 6).

In the soil mechanics, it is appropriate to apply the non-associated flow law with $\psi < \beta$.

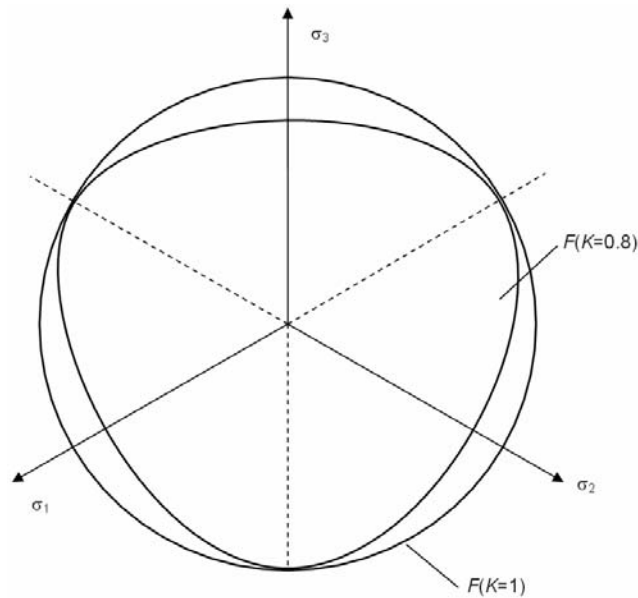


Fig. 6. Plasticity surface in the case of Drucker–Prager’s linear condition in deviator plane (negative compressive stresses have been adopted)

Adjusting Coulomb–Mohr’s parameters to Drucker–Prager’s model

In the event that experimental data (friction angle and cohesion) have already been graduated because of Coulomb–Mohr’s model, they can be converted into Drucker–Prager’s linear model, determining the parameters β and d . As a result of the comparison of two equations defining the surface of plasticity in Drucker–Prager’s and Coulomb–Mohr’s models, the following equations are obtained that connect the material parameters in Coulomb–Mohr’s model with the parameters of Drucker–Prager’s linear model (in the flat state of strain):

$$\sin \phi = \frac{\tan \beta \sqrt{3(9 - \tan^2 \psi)}}{9 - \tan \beta \tan \psi}, \quad (10)$$

$$c \cos \phi = \frac{\sqrt{3(9 - \tan^2 \psi)}}{9 - \tan \beta \tan \psi} d. \quad (11)$$

In the event of the associated flow law ($\psi = \beta$) from Equations (10), (11) the following material parameters arise in Drucker–Prager’s model:

$$\tan \beta = \frac{\sqrt{3} \sin \phi}{\sqrt{1 + \frac{1}{3} \sin^2 \phi}}, \quad (12)$$

$$\frac{d}{c} = \frac{\sqrt{3} \cos \phi}{\sqrt{1 + \frac{1}{3} \sin^2 \phi}}. \quad (13)$$

In a specific case of the non-associated flow law ($\psi = 0$) we can write:

$$\tan \beta = \sqrt{3} \sin \phi, \quad (14)$$

$$\frac{d}{c} = \sqrt{3} \cos \phi. \quad (15)$$

In both cases, plasticizing stress at the compression σ_c^0 is expressed as

$$\sigma_c^0 = \frac{1}{1 - \frac{1}{3} \tan \beta} d. \quad (16)$$

The differences between the values of parameters determined in both flow laws increase together with the value of the friction angle ϕ ; however, they are slight and not larger than a few per cent, whereas the discrepancy between the values of parameters in the C–M and D–P models is substantial at low values of material parameters and decreases together with an increase in the value of friction angle ϕ .

Similar theoretical considerations can be made in order to adjust the models discussed to the spatial specification of the soil medium state of strain. In the system of the invariants p and q , the values of the parameters β and d are determined in Drucker–Prager’s linear model (Figure 7) and the coefficient K as well (determining the ratio of plasticizing stresses in tension to stresses in compression in the deviator plane:

$$K = \frac{q_t}{q_c}.$$

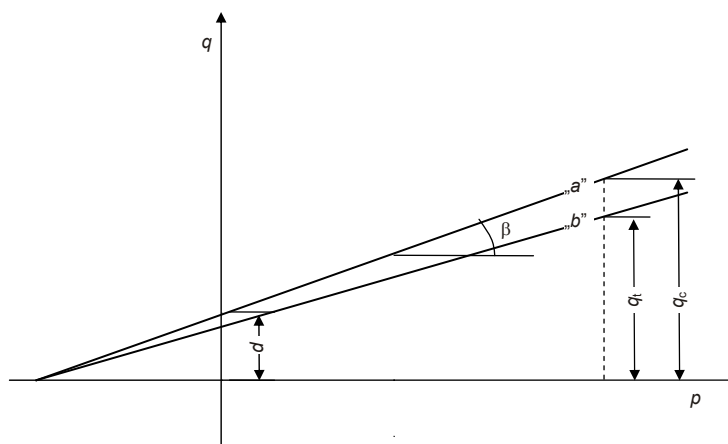


Fig. 7. Adjusting the linear model in triaxial test

By comparing both models, the values of material parameters are obtained:

$$\tan \beta = \frac{6 \sin \phi}{3 - \sin \phi}, \quad (17)$$

$$\sigma_c^0 = 2c \frac{\cos \phi}{1 - \sin \phi} \quad (18)$$

as well as

$$K = \frac{3 - \sin \phi}{3 + \cos \phi}. \quad (19)$$

In practical applications, it is necessary to take into account the fact that the value of the coefficient K in Drucker–Prager’s linear model is limited by the condition of the surface of plasticity convexity ($K \geq 0.778$). It limits the employment of dependence (19) up to the value of the friction angle $\phi \leq 20^\circ$. With higher values of ϕ it is necessary to adopt $K = 0.788$ – using formulae (17), (18) in order to transform parameters from the C–M to the D–P model. If the friction angle, however, is substantially greater than 22° , then the presented adjustment is not sufficiently accurate and the best solution is to adopt Coulomb–Mohr’s model for calculations.

While modelling an earthen structure by dint of MES, the bearing-capacity limit point can be achieved by:

- The reduction of soil strength parameters c/R_F and ϕ/R_F and by means of trial and error method arriving at such a maximum value of reduction coefficient R_F that provoked substantial displacements of characteristic points of the structure. It may indicate the loss of slope stability or the loss of bearing capacity of the subsoil.
- An incremental increase in the structure load over the nominal value while simultaneously observing the characteristic points of the structure. Then such a limit load value q_{gr} is being sought that will provoke a substantial increase in displacements.

The employment of the reduction of strength parameter method causes that the reach of plastic zones is extended beyond the impact of an embankment (in which the soil maintains elasticity). The limit load method leads to the development of a plastic zone only in the areas where the actual slip zones occur as a result of the loss of bearing capacity of the soil. Its advantage is that it is easy to define the boundary conditions by an incremental increase in the load. There is no need to intervene every time in the soil material model, which is indispensable in the case of employing the previous method.

The authors [10] analysed embankments in the flat state of strain by using the method of the reduction of soil strength parameters (c , ϕ). Comparative calculations were made by using a Polish geotechnics-oriented program HYDRO-GEO [11] and a general, based on the advanced Finite Element Method – ABAQUS [12]. The former, in an available version, did not lead to the determination of plastic strains in the structure, but only provided a description of the reach of plastic zones. By using it, unlike in the case of the ABAQUS, it was not possible to determine the coefficient of the embankment stability. The ABAQUS’s advantage was the possibility of determining the coefficient of inelastic strains as well as modelling the structure in three dimensions. Including additionally the change in cohesion caused by ravelling and determining SGN by dint of the limit load method produce more realistic results of the analyses.

Below there are selected results and conclusions drawn from the static and strength analyses of the embankment in the flat and spatial state of strain. They concern the embankment that is being made along the section of the Wrocław–Kraków A4 motorway running across the areas of productive mines in Upper Silesia. Coal field is exploited by dint of longwall working with fall of ground. The exploitation is carried out

at the height of 1.40–3.60 m, and at the depth of 600–940 m. Under the section of the motorway that is being built the exploitation has been limited. What is tolerable is a mining impact characterized by the values of the 2nd category of the mining area.

6. MES analyses in flat state of strain

Geomorphological and geotechnical conditions of the ground under the analysed section of the motorway are considered to be complicated. Under the superficial layer of sandy soil, in the subsoil there are deposited organic cohesive soils containing on average 4.1% of organic matter and 60% of silt and clay fraction. Humus silty clay in a plastic state is quite widespread. Deeper we can find heterogeneous cohesive soils (average silt and clay fraction content is 63%). Among others, firm silty clays occur here. Underneath there is carrying ground – fine grained irrigated soil, in a moderately concentrated state.

In order to increase the bearing capacity of the foundation and the embankment located on “infirm” ground subject to mining deformations, the reinforcement of the foundation was adopted. It was suggested that a mat made of grainy material reinforced with geo-synthetics should be built in the foundation. Its outline reaches 3 m outside the footing. The mat’s height of 0.50 m was achieved by placing three layers of geocells. Between the foundation and the mat a non-woven geotextile fabric was placed preventing grained aggregate from fusing with cohesive subsoil.

The embankment was modelled with the Finite Element Method by using the ABAQUS program. The elastoplastic material model with reinforcement at shearing was adopted.

In the calculations, the simplification of diversified ground and water conditions was assumed in order to eliminate the influence of the diversification of geotechnical layers on the results of calculations. An embankment built of cohesive soil on a homogeneous cohesive ground was examined. What was not included was the influence of time on the process of mining deformations and the change in the values of soil strength parameters (the embankment is being built). Only the convex part of the subsiding trough was included (tension strains).

Two static models of an embankment were analysed: a) an embankment made of natural loose ground with aggregate supplement obtained from burnt shale founded on cohesive and homogeneous ground made of firm silty clay (Figure 8); b) an embankment whose foundation was reinforced with a 0.50 m thick mat (average strength parameters of the composite material were adopted) (Figure 9).

Figure 10 illustrates the adopted reduction in the cohesion c_R of soil and embankment related to ravelling strains ε_R in accordance with (1). The output data as well as the values of the reduced cohesion d_R in Drucker–Prager’s model and the reduced plasticizing stress σ_c^0 are presented in Table 2.

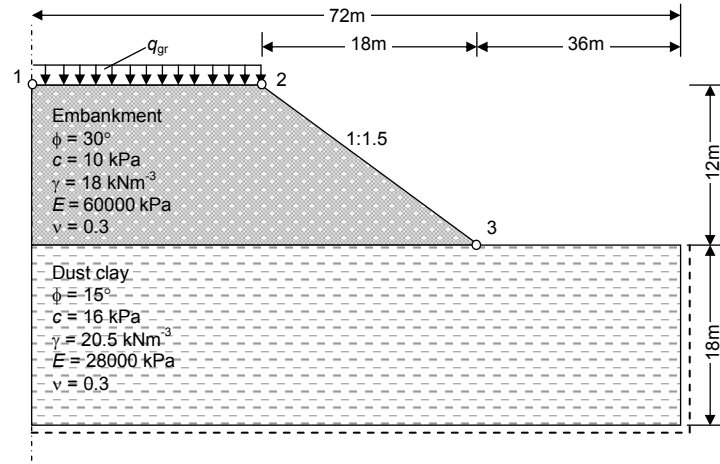


Fig. 8. Static model of an embankment without reinforcement that allows reduction of mining effects

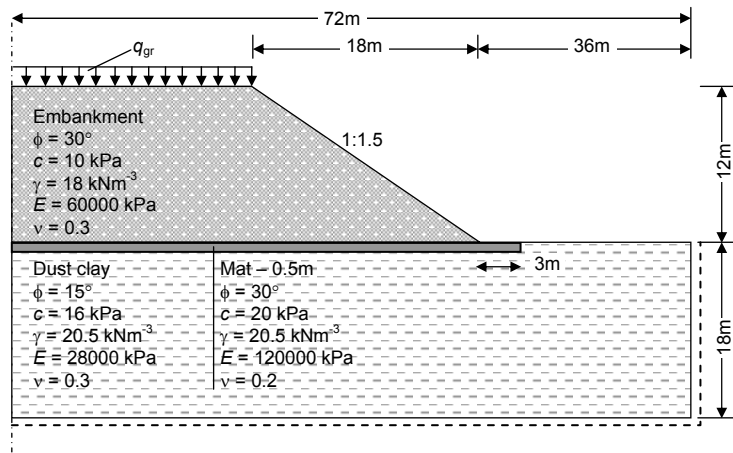


Fig. 9. Static model of an embankment on the foundation reinforced with a mat

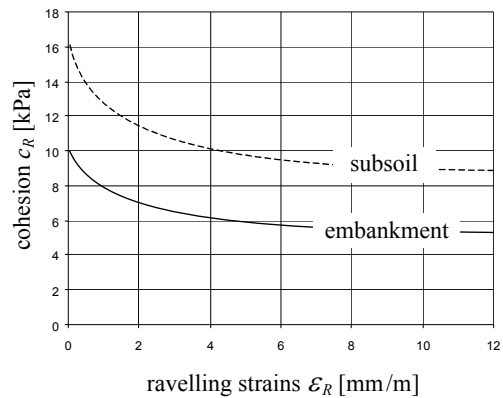


Fig. 10. Reduction in soil cohesion in foundation and embankment

Table. 2 Values of reduced cohesion in Drucker-Prager's model

Subsoil				Embankment with burnt shale			
$\phi = 15.0[^\circ]$				$\phi = 30.0[^\circ]$			
$\beta = 24.15[^\circ]$				$B = 40.89[^\circ]$			
$C_0 = 16.00[\text{kPa}]$				$C_0 = 10.00[\text{kPa}]$			
$c_{kr} = 8.00[\text{kPa}]$				$c_{kr} = 5.00[\text{kPa}]$			
$\alpha_R = 1.5[-]$				$\alpha_R = 1.5[-]$			
ε_R	c_R	d_R	σ_c^0	ε_R	c_R	d_R	σ_c^0
0.00	16.00	26.77	31.47	0.00	10.00	15.00	21.09
0.30	14.67	24.54	28.86	0.30	9.17	13.76	19.34
0.65	13.58	22.72	26.71	0.65	8.49	12.74	17.90
1.00	12.80	21.41	25.18	1.00	8.00	12.00	16.87
1.50	12.00	20.08	23.60	1.50	7.50	11.25	15.82
2.00	11.43	19.12	22.48	2.00	7.14	10.71	15.06
2.50	11.00	18.40	21.64	2.50	6.88	10.32	14.51
3.00	10.67	17.85	20.99	3.00	6.67	10.01	14.07
4.00	10.18	17.03	20.02	4.00	6.36	9.54	13.41
5.00	9.85	16.48	19.37	5.00	6.15	9.23	12.97
6.00	9.60	16.06	18.88	6.00	6.00	9.00	12.65
9.00	9.14	15.29	17.98	9.00	5.71	8.57	12.04
12.00	8.89	14.87	17.49	12.00	5.56	8.34	11.72

Mining deformations of the surface are typical of the mining area of the 2nd category, whose maximum horizontal strain $\varepsilon = 3$ mm/m, minimum radius of curvature $R = 12\,000$ m and maximum slope of the surface $T = 5$ mm/m. It has been assumed that the depth of exploitation $H = 600$ m, exploited seam thickness $g = 2.0$ m, parameter of rock mass $\tan\beta = 2.0$; exploitation coefficient a ranges from 0.70 to 0.85 (Figure 11). The remaining values of parameters and the index of strain have been determined on the basis of Budryk–Knothe's theory [2], [5], assuming infinitely long, linear exploitation front.

The displacements of the embankment foundation were determined by placing the exploitation front in parallel to the axis of the embankment (direction of exploitation perpendicular to the axis of the embankment). Not only was the embankment subject to tension strains, but also the curvature of terrain was included, which has a major influence on the obtained values of displacement because of a substantial size of the embankment. The symmetry of the problem was included (Figure 12). In the first stage, the embankment was subject to forced mining deformations, and then load was incrementally imposed along the top until the loss of stability. Mining deformations were introduced by forced horizontal and vertical displacements of foundation nodes, increasing in proportion to the distance from the axis of the embankment. Between the embankment foundation and the ground a contact surface was introduced, adopting the

full transfer of normal stress with any separation of contact surfaces. Tangential stress was modelled by means of the coefficient of friction $\mu = 0.95$ and a critical shear stress τ_{\max} , equalling the maximum strength of the ground to shearing (which is 50.0 kPa).

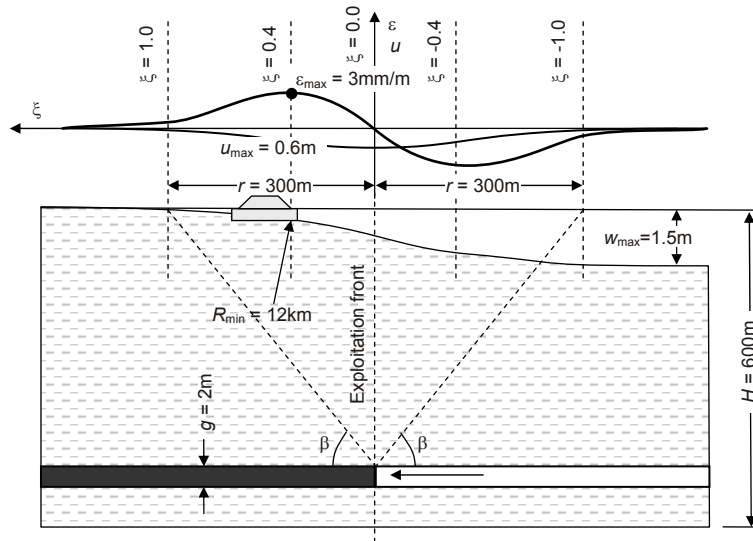


Fig. 11. Parameters of mining deformations in the terrain of the 2nd category

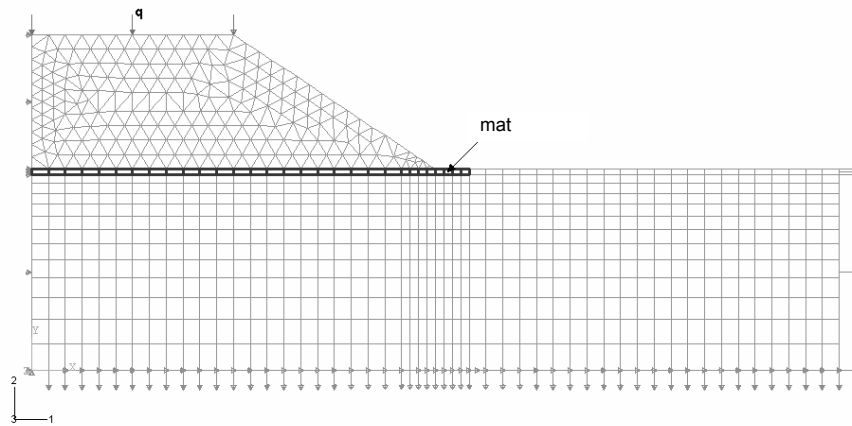


Fig. 12. Design model of 2D embankment on reinforced mat

Drucker-Prager's linear, elastoplastic model with reinforcement for shearing was used for the description of the soil. Material parameters, i.e. β – angle of friction and

σ_c^0 – reinforcement, were determined with the dilatation $\psi = 0$, transforming parameters ϕ and c from the Coulomb–Mohr’s model.

Table. 3. Material parameters

Material parameters			
Material	Subsoil	Embankment	Mat
Coulomb–Mohr’s model			
c [kPa]	16.00	10.00	20.00
ϕ [°]	15.00	30.00	30.00
Drucker–Prager’s model			
$\tan \beta$	0.448288	0.866025	0.866025
β [°]	24.15	40.89	40.89
d/c	1.67	1.50	1.50
D [kPa]	26.77	15.00	30.00
σ_c^0 [kPa]	31.47	21.09	42.17

The subsequent stages of calculations include: introduction of initial stress into the ground (0); simulation of the embankment’s erection (I); mining deformations (II); adoption of service load of transport structure: $q = 24$ kPa (III); limit load (IV); overload (V). Four types of an embankment were considered: a) without a mat and without deformations; b) without a mat, with deformations; c) with a mat, without deformations; d) with a mat and with deformations. The following parameters of embankment were examined: horizontal and vertical displacements of its characteristic points; limit loads, stresses and plastic strains. Figures 13, 14, 15 illustrate the model of the embankment’s strains after forced mining deformations as well as the horizontal and vertical displacements of the characteristic points of the embankment subject to stretching mining deformations.

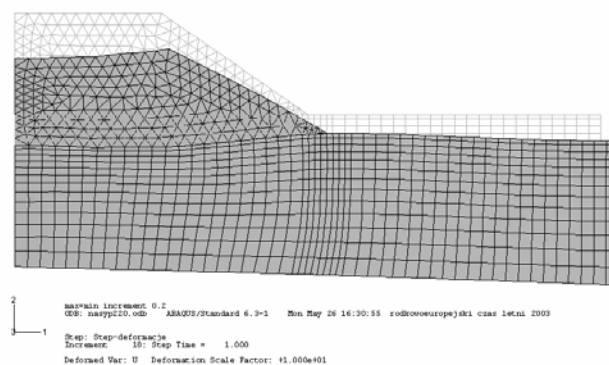


Fig. 13. Deformed 2D embankment after forced mining deformations

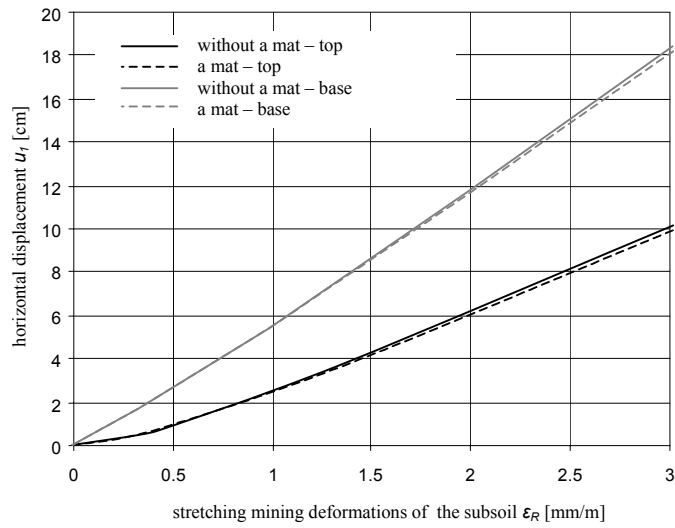


Fig. 14. Horizontal displacement of characteristic points of 2D embankment subject to stretching mining deformations

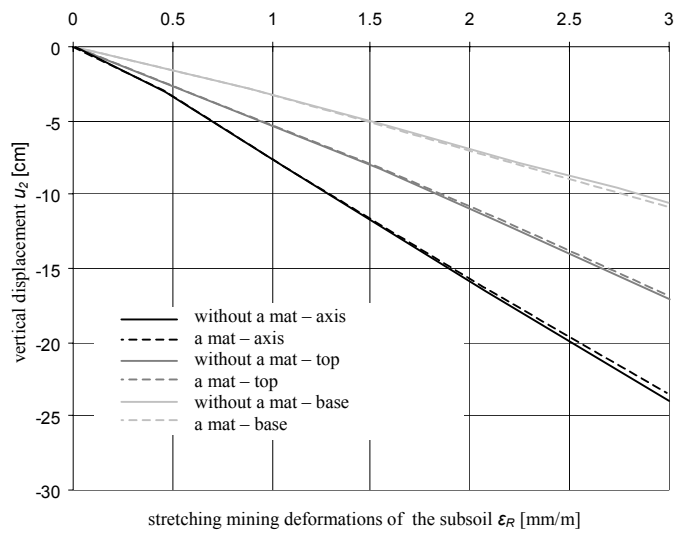


Fig. 15. Vertical displacement of characteristic points of 2D embankment subject to stretching mining deformations

The results of the analysis performed constituted the basis for formulating the following conclusions and generalizations:

- While modelling mining deformations it is necessary to include not only the force displacements of the embankment support resulting from terrain subsidence w and horizontal displacement u , but also the curvature of terrain, which causes the turn of the edge of the model. Including merely the ravelling of the soil does not provide a realistic distribution of stresses, especially in the near-surface layer of terrain and the embankment.

- In mining areas, the embankments made of cohesionless soils are difficult to model in MES, because the limit state is quickly reached. In practice, those embankments tend to form earthslides (a mixture of loose ground with cohesive material, e.g. burned shale and reinforcement of the embankment body with geosynthetics from top to bottom, is used).

- Use of a mat reinforcing the foundation leads to an increase in the values of tangential stresses (S_{12}) in the embankment slope. This mobilization is visible in all stages of calculations, whereas the effect of forced stretching deformations in the embankment's slope results in the reduction of tangential stress.

- As a result of forced mining deformations, the earthen structure's deadweight as well as service load, substantial plastic strains occur in the embankment foundation and the ground. Strengthening the foundation with a mat reinforced with geosynthetics increases its bearing capacity; it does not, however, decrease the value of the embankment's displacements.

- The need for identifying the impact of the direction of exploitation on bearing capacity and the embankment's deformations creates a necessity to include a spatial state of strain.

7. MES analyses in spatial state of strain

The static model of the embankment comprises a full section of the body, without including symmetry. A decrease in the cohesive soil strength of the embankment and the foundation was considered by reducing cohesion. The exploitation front of mines was placed at different angles to the longitudinal axis of the embankment: $\alpha = 0^\circ$ – exploitation front is parallel to the axis of the embankment (only mining deformation component in the plane perpendicular to the axis of the embankment occurs); $\alpha = 30^\circ$, 45° , 60° and $\alpha = 90^\circ$ – exploitation front perpendicular to the axis of the embankment (Figure 16). The analysed section of the embankment is within the radius of principal effect range $r = 300$ m. In each node of the MES grid, forced displacements were determined: subsidence w , horizontal displacement u , the turn of the vertical edge of terrain resulting from its curvature.

Two design models of the embankment were analysed: non-reinforced on the ground reinforced with a mat under the body (Figure 17). In the first stage of calculations, the embankment was subject to forced mining deformations with the exploitation front placed at an angle of 0° , 30° , 45° , 60° and 90° . In the second stage – load was incrementally imposed along the top until the loss of stability. Mining deforma-

tions were introduced by forced horizontal and vertical displacements of foundation nodes, increasing in proportion to the distance from the straight line $\zeta = 1.5$ (defining practically zero mining deformations). The nodes on the vertical planes of the embankment's edge were subject to forced displacements in two directions that depended on the distance from the straight line $\zeta = 1.5$, and also on the hollow in relation to the terrain surface. The operational load was imposed incrementally along the embankment top, increasing its value by 2.0 kPa at each step of calculations. The elastoplastic soil model with modified Drucker–Prager's condition of plasticity was adopted.

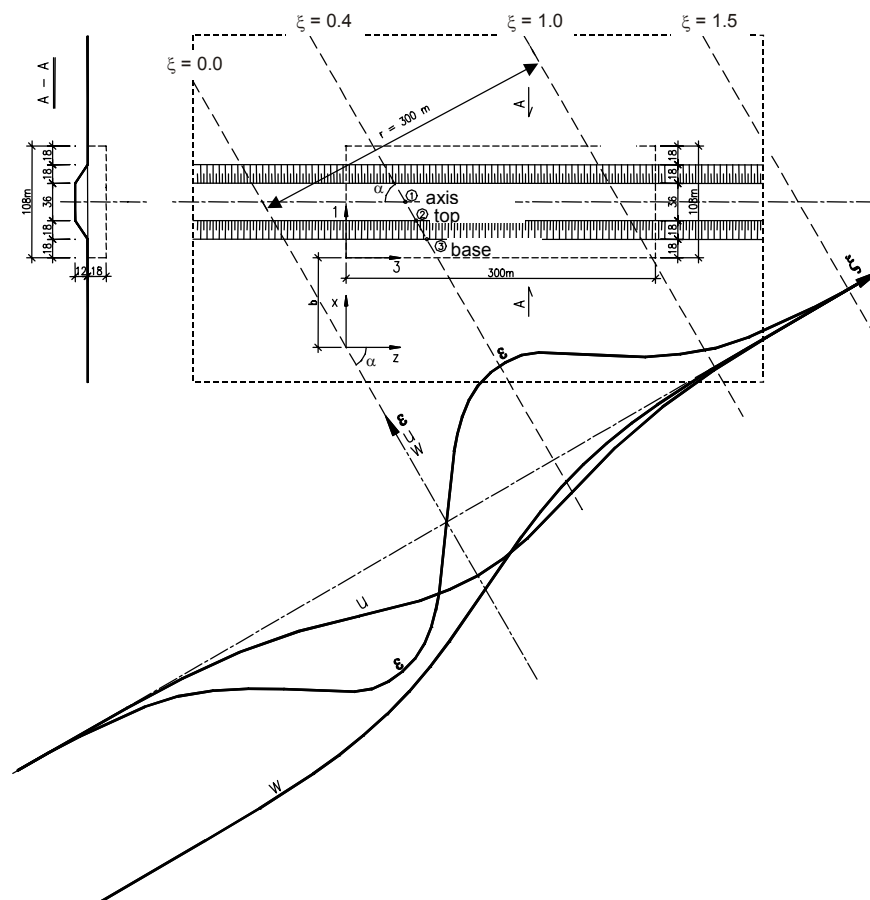


Fig. 16. Location of mining deformations in relation to the axis of embankment

The deformed MES grid of the embankment, together with its outline before introducing mining deformations, $\alpha = 45^\circ$, is presented in Figure 18. The results of calculations are illustrated in Figures 19–23.

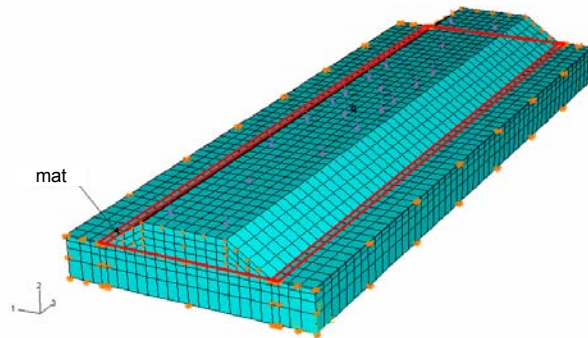


Fig. 17. Design model of embankment on reinforced mat

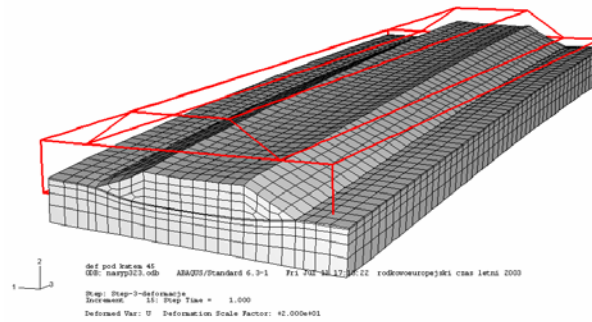


Fig. 18. Deformed (3D) embankment after forced mining deformations

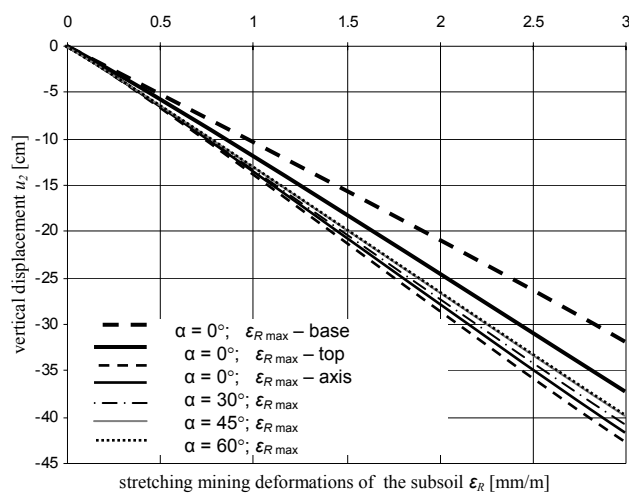


Fig. 19. Influence of the direction of exploitation on subsiding in axis of top during deformations

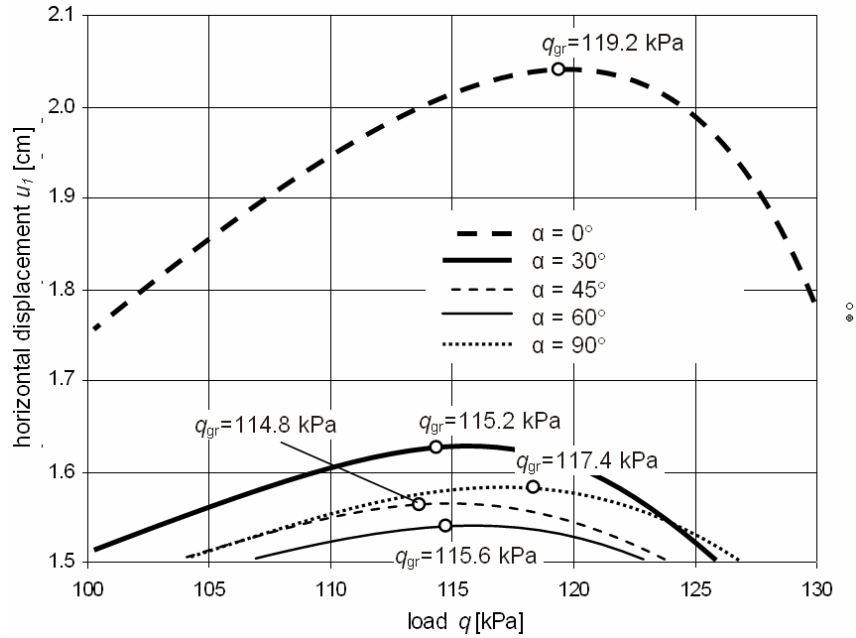


Fig. 20. Variation of limit load with two different directions of exploitation

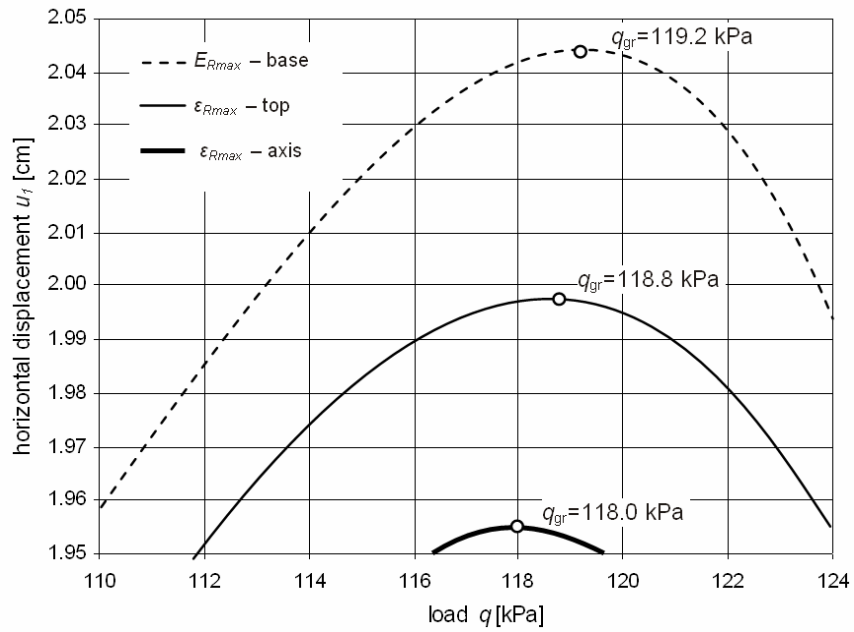


Fig. 21. Dependence of limit load on the place where it is imposed ϵ_{max} , with parallel front

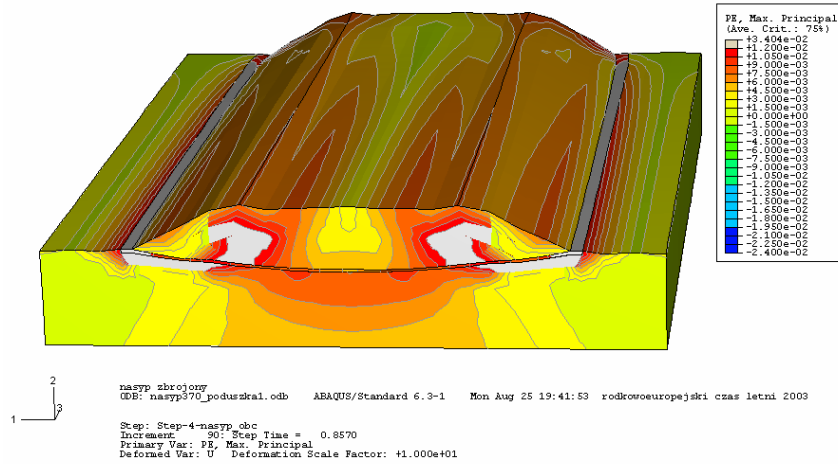


Fig. 22. Maximum plastic strain PE_{\max} in the cross-section of reinforced embankment after exceeding a limit state (without mining deformations)

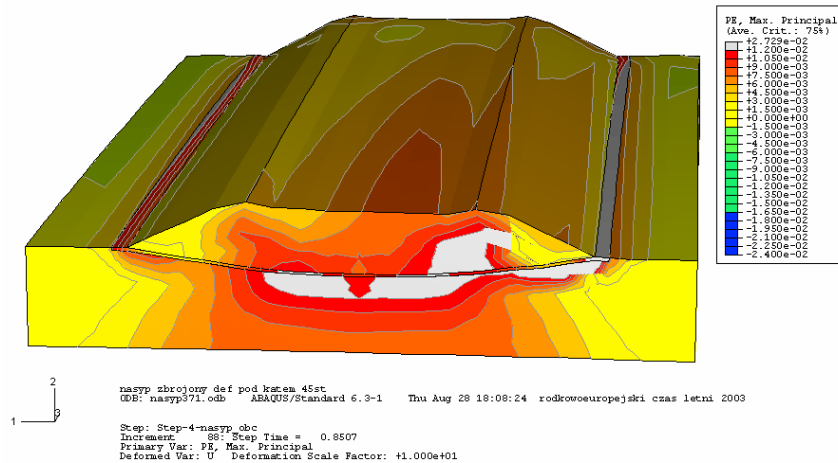


Fig. 23. Maximum plastic strain PE_{\max} in the cross-section of reinforced embankment after exceeding a limit state deformed by diagonal exploitation front ($\alpha = 45^\circ$)

8. Conclusions from numerical analyses

Displacements of embankment points (horizontal and vertical)

- Vertical displacements (in the axis of the top) to a slight degree depend on the direction of exploitation (Figure 19). Even smaller differences in displacements were obtained on the edge of the top (1.60 cm). The greatest subsidence (38.40 cm) oc-

curred with the perpendicular exploitation front, and the smallest – with the parallel one. Minimum differences of the displacements occur on the edge of the footing (1.0 cm).

- Horizontal and vertical displacements of the embankment set on the foundation reinforced with a mat are not reduced compared with the embankment without reinforcement. A slight impact of the direction of exploitation on the values of horizontal and vertical displacements is being observed in the analyses of the embankment top displacements incrementally loaded in the third stage of calculations. There are marked differences in the values of horizontal displacements of the edge of the top in the event of exploitation with the front parallel to the axis of the embankment. When the front is positioned in different ways, the paths of displacement are almost identical. The influence of the position of the direction of exploitation on the limit load value is illustrated in Figures 19, 20, 21.

Limit loads

- The lowest value of limit load corresponds to the exploitation at an angle of $\alpha = 45^\circ$ to the axis of the embankment, and the highest – with the front positioned in parallel ($\alpha = 0^\circ$).

- The load reaches the lowest value when the maximum tension strain is imposed in the axis of the embankment top. The influence of the direction of exploitation is bigger when embankment is made of cohesionless soil being more susceptible to ravelling.

- In the event of the embankment on the foundation reinforced with a mat ($\alpha = 45^\circ$), a substantial increase in limit load, i.e. by 15%, occurs (up to 132.0 kPa) compared to the limit load of the embankment without reinforcement.

Stresses

- The state of stress depends on the position of the exploitation front in relation to the longitudinal axis of the embankment. On the axis, where tension strains act, the development of tension strain zone is visible in the near-surface layer of soil, with the change in the state of stress in the layers deposited deeper. In the case of mining deformations oriented perpendicularly to the axis of tension strain effect, their increase in the deeper layers of soil occurs.

- As a result of horizontal tension strain effect, an increase in stresses on the axis perpendicular to the forced strains occurs, and on the axis consistent with mining deformations, a reduction in vertical stresses takes place in the foundation.

- The biggest increment in the value of reduction of stresses occurs in the place where the biggest tension strains are imposed, within the distance of $\zeta = 0.4$ from the exploitation front (with the exploitation front perpendicular to the axis of the embankment, the increment of horizontal strain S_{11} under the body of the embankment,

on the transverse axis of the embankment, was ~ 25.0 kPa, and the reduction in horizontal strain $S33$ on the longitudinal axis of the embankment approached 20.0 kPa).

- Tangential strains $S12$ undergo a substantial reduction in the embankment slope and immediately under the embankment footing, with a simultaneous slight increase in the foundation, close to the footing: in the cross-section of the embankment on the reinforced foundation ($\alpha = 45^\circ$), their reduction equals 15.0 kPa.

Plastic strains

- The increment of plastic strains appearing in the stage of mining deformation exceeds their values by several times, occurring in the loaded embankment, without those deformations.

- Extreme values of strain are concentrated in the area of the most substantial raveling of the soil, and horizontal components $PE11$ and $PE33$ depend on the direction of exploitation.

- As a result of mining deformation effect, a substantial increase in horizontal plastic strain $PE11$ occurs.

- Tangential strains $PE12$ are reduced at the deformation stage, and while the top is loaded, they increase again, but they do not exceed the strain value $PE12$ appearing in an embankment without deformations (with identical load).

- Horizontal plastic strain $PE11$, and also $PE33$ in the case of the diagonal front, has a decisive influence on the loss of stability of embankments located in mining areas.

- The composition of maximum plastic strains PE_{max} , determined after exceeding the limit state, allows us to pinpoint theoretical slip planes. In the embankment without mining deformations in the extreme strains PE_{max} , it is possible to circumscribe the cylindrical slip plane (Figure 22), unlike in the case of the embankment subject to mining effects (Figure 23).

The performed MES numerical simulations give rise to suggestions concerning the mechanisms governing the loss of bearing capacity of embankments on “infirm” cohesive soil. The loss of bearing capacity occurs as a result of reaching the boundary bearing capacity by the central section of the embankment. As a result of soil raveling, in the embankment slope a reduction in shear strains takes place. The loss of stability of the slope occurs after reaching the limit state and after substantial displacements of the central part of the embankment have occurred. To define the soil medium, a modified Drucker–Prager’s condition of plasticity is as good as Coulomb–Mohr’s condition.

The values of vertical displacements of the embankment subject to mining deformations virtually do not depend on the direction of exploitation. What changes, however, is their distribution on the surface of the top of the embankment. Because of the flexure of the embankment top in the cross-section, the most disadvantageous is a par-

allel front, and the biggest increments in subsidence along the embankment are obtained with the front perpendicular to the axis.

Strengthening the foundation with a mat reinforced with geosynthetics has an influence on the increase of the embankment's bearing capacity, with a simultaneous increase in displacements. A reduction in horizontal displacements as a result of using this way of strengthening an earthen structure has not been observed.

9. Conclusions

As a result of mining deformation effect, embankments are subject to substantial horizontal and vertical deformations and ravelling, which is conducive to the loss of their stability. The factor determining the stability of embankments is the impact of mining-area subsoil horizontal strains.

The solutions presented constitute a new approach to expressing such a complicated geotechnical problem as designing and building transport earthen structures founded within the range of the impact of exploitation of mine effects. It follows from them that a spatial analysis of an embankment with the Finite Element Method, with the introduction of the full cross-section of the body and the actual mining displacements, is the most effective way of determining displacements and an earthen structure's bearing capacity. It shows how the direction of exploitation of mines influences the obtained limit load values as well as displacements of an embankment founded on an "infirm" soil. The employment of the block methods used in engineering only allows us to assess the embankment's bearing capacity without the possibility of determining the structure displacements.

MES spatial analyses of an embankment allow us to take measures in order to secure those structures against mining effects. Strengthening the foundation with a mat reinforced with geosynthetics results in an increase in the embankment's bearing capacity and protects it against sudden and non-uniform subsidence, but also partly reduces horizontal mining displacements and subsidence of the top of an earthen structure. Using a mattress made of geogrids made of high-density polyethylene, with rigid nodes, filled with stony material causes that it takes tension stresses appearing during soil ravelling, and at the same time it constitutes protection against out-of-control sink holes.

The MES ABAQUS software package was used for the numerical calculations which were carried out with the computers of the Wrocław Centre of Networking & Supercomputing.

References

- [1] Bathe K. J.: *Finite element procedures*, Prentice Hall, Englewood Cliffs, 1996.
- [2] Budryk W.: *Wyznaczanie wielkości poziomych odkształceń terenu*, Archiwum Górnictwa i Hutnictwa, 1953, t. 1, z. 1.

- [3] Drucker D.C., Prager W.: *Soil mechanics and plastic analysis or limit design*, Quart. Appl. Math., 1952, Vol. 10, 157–165.
- [4] Glinko H.: *Przebieg procesu rozluźnienia gruntów spoistych w świetle badań wytrzymałościowych i strukturalnych*, Prace IIBiS Politechniki Lubelskiej, Seria A, nr 10, Lublin, 1984.
- [5] Knothe S.: *Równanie profilu ostatecznie wykształconej niecki osiadania*, Archiwum Górnicztwa i Hutnictwa, 1953, t. 1, z. 1.
- [6] Kwiatek J. (red.): *Ochrona obiektów budowlanych na terenach górniczych*, Wyd. Głównego Instytutu Górnicztwa, Katowice, 1998.
- [7] Litwinowicz L.: *Wpływ rozluźnienia nasypów znajdujących się w zasięgu oddziaływania podziemnej eksploatacji górniczej na ich stateczność*, Prace Inst. Inżynierii Budowlanej i Sanitarnej Politechniki Lubelskiej, Seria A (monografie), nr 7, Lublin, 1982.
- [8] Rusiński E., Czmochowski J., Smolnicki T.: *Zaawansowana metoda elementów skończonych w konstrukcjach nośnych*, Oficyna Wyd. Politechniki Wrocławskiej, Wrocław, 2000.
- [9] Stilger-Szydło E., Tutaj W.: *Wpływ deformacji górniczych na stateczność nasypów komunikacyjnych*, Inżynieria i Budownictwo, 2003, 8, 446–451.
- [10] Stilger-Szydło E., Tutaj W.: *Effect of Mining Deformations on Stability of Transport Embankments*, Studia Geotechnica et Mechanica, 2004, Vol. XXVI, No. 3/4.
- [11] Program MES: HYDRO-GEO v. 3.0. Politechnika Warszawska, Wydział Inżynierii Środowiska, 1997. Dłużewski J.M., HYDRO-GEO, *Program elementów skończonych dla geotechniki, hydrotechniki i inżynierii środowiska*, Oficyna Wydawnicza Politechniki Warszawskiej, Warszawa, 1997.
- [12] Program MES: ABAQUS v. 6.2 Hibbitt, Karlsson & Sorensen, Inc., 2001.

Wpływ podziemnej eksploatacji górniczej na stan naprężenia i przemieszczenia nasypów budowli komunikacyjnych

Przybliżono podstawy teoretyczne oraz koncepcje zarówno modelowania współpracy nasypu z podłożem górniczym, jak i prognozowania jego deformacji. Są one ukierunkowane głównie na badanie wpływu rozciągających odkształceń górniczych oraz na bezpieczną eksploatację konstrukcji drogowych. Przedstawiono rozwiązania (z zastosowaniem MES) w płaskim i w przestrzennym stanie odkształcenia, przyjmujące zróżnicowane usytuowanie frontu eksploatacji względem osi nasypu oraz wzmocnienie podłoża gruntowego. W obliczeniach numerycznych ośrodek gruntowy opisano za pomocą modelu ciała sprężystoplastycznego, a stan graniczny – ośrodka za pomocą zmodyfikowanego warunku plastyczności Druckera–Pragera ze wzmocnieniem zależnym od spójności. Oceniano przemieszczenia i naprężenia w nasypie posadowionym na podłożu górniczym, dokonując sprężystoplastycznej analizy z zastosowaniem pakietów programów MES: HYDRO-GEO ver. 3.0 oraz ABAQUS.

W załączonych przykładach wyznaczono wartość obciążenia granicznego przyłożonego w koronie nasypu, stan naprężenia i przemieszczenia oraz zasięgi stref plastycznych w korpusie i podłożu. Przedstawione rozważania teoretyczne oraz dokonane analizy naprężeń i przemieszczeń nasypów mogą być pomocne w opracowaniu nowych sposobów zabezpieczeń budowli ziemnych i podłoża górniczego.



Information about PhD thesis at the Civil Engineering Faculty and the Mechanical Engineering Faculty of Wrocław University of Technology

Title: *Load capacity of one-sided longitudinally stiffened steel plates (in Polish)*
Nośność stalowych płyt uźebrowanych jednostronnie podłużnie

Author: Jacek Kudziela

Supervisor: Professor Ernest Kubica

Promoting Council: Institute of Building Engineering, Wrocław University of Technology

Reviewers:

Professor Zbigniew Kowal

Professor Kazimierz Rykaluk

Date of PhD thesis presentation: December 1st, 2004

PhD is available in Main Library and Scientific Information Centre of WUT

The monograph contains: 220 pages, 164 figs, bibliography: 88 items, 1 annex: 9 pages.

Keywords: *longitudinally stiffened plates, residual stresses, geometrical imperfections, bearing capacity of compression load*

Abstract: Compressed steel plates with longitudinal stiffeners were taken into consideration. The plates with stiffeners of blade of T-shape and closed cross-sections were tested. The actual shape of geometrical imperfections of stiffeners and plates was measured and the shape of residual stresses was estimated by the Okerblom method. The equilibrium paths and deflection curves in the full range of deflections were given as a result of experimental tests.

Finite element analyses were also performed. The impact of geometrical imperfections, residual stresses, local and global slenderness and cross-section shapes on equilibrium paths, compression capacity and ductility of compressed longitudinally stiffened plates was determined. The equilibrium paths derived based on finite element analysis and obtained from experimental studies were compared. The impact of restraining in the transverse stiffeners with different torsional stiffness was studied.

The analytical procedures that allow determining equilibrium paths of non-stiffened and longitudinally stiffened plates in the full range of deflections were presented. The equilibrium paths derived based on those analytical procedures and finite element analyses were compared.

The initial imperfection factors of plates with longitudinal stiffeners of different cross-section shapes were derived. The value of limit stresses obtained from experimental studies and simple analytical methods that allow deriving those stresses were used in order to calculate the factors.

Title: *The influence of design parameters on the characteristic of the multifunction hydrostatic machine (in Polish)*
Wpływ wybranych cech konstrukcyjnych na charakterystyki wielofunkcyjnej maszyny hydraulicznej zębatej

Author: Michał Banaś

Supervisor: Doctor Jarosław Stryczek, Professor of Wrocław University of Technology

Promoting Council: Institute of Machines Design and Operation, Wrocław University of Technology

Reviewers:

Doctor Andrzej Milecki

Doctor Franciszek Przystupa

Date of Ph.D. thesis presentation: January 4th, 2005.

PhD is available in Main Library and Scientific Information Centre of WUT

The monograph contains: 158 pages, 91 figs, bibliography: 60 items

Keywords: *multifunction hydrostatic machine, rotary spool valve*

Abstract: The monograph deals with multifunctional hydrostatic machines (MHMs). It describes design and operation of MHM as a pump, motor and rotational speed changer. The mathematical equations were formulated to describe the phenomena and processes in the machine, especially in the rotary spool valve. The model has been verified in a special test stand. The changes in rotational speed of pump and motor were examined. The result of the investigations were taken to calculate the coefficients of the model. The influence of some design parameters on the static characteristics was shown. It enabled us to create the method of forming the characteristics of MHM. Using this method the geometrical parameters of clearances in the rotary spool valve were calculated.

Title: *Modelling of dynamic stability of industrial vehicles with spring elements of suspension (in Polish)*
Modelowanie stateczności dynamicznej pojazdów przemysłowych z podatnymi elementami jezdnyymi

Author: Tomasz Siwulski

Supervisor: Professor Piotr Dudziński

Promoting Council: Institute of Machines Design and Operation, Wrocław University of Technology

Reviewers:

Professor Stanisław Konopka

Professor Kazimierz Pieczonka

Date of PhD thesis presentation: January 11th, 2005.

PhD thesis is available in Main Library and Scientific Information Centre of WUT

The monograph contains: 188 pages, 124 figs, bibliography: 80 items

Keywords: *industrial vehicle, dynamic stability*

Abstract: The phenomena affecting dynamic stability of industrial wheel vehicles were identified. A preliminary analysis of the dynamic stability phenomena was performed. The simulation tests were carried out based on dynamic models of vehicles, created in “multibody” system using MBS-DADS program. The dynamic models were positively verified. The influence of selected parameters of vehicle on dynamic stability was tested based on numerical models.

A new system allowing an increase in the dynamic stability of industrial vehicles was proposed and tested.

Title: *The influence of water depth on viscous resistance of inland navigation vessel (in Polish)*
Wpływ głębokości drogi wodnej na opór lepkościowy statku śródlądowego

Author: Maciej Zawiślak

Supervisor: Professor Jan Kulczyk

Promoting Council: Institute of Machines Design and Operation, Wrocław University of Technology

Reviewers:

Professor Jan Szantyr

Professor Janusz Plutecki

Date of PhD thesis presentation: March 8th, 2005

PhD thesis is available in Main Library and Scientific Information Centre of WUT

The monograph contains: 137 pages, 120 figs, bibliography: 89 items

Keywords: *inland vessel, resistance, coefficient of viscous resistance, CFD, shallow water*

Abstract: Inland vessels sail through, the waterways of limited width and low depth. Current methods of resistance prediction based on model tests do not provide reliable results in the case of shallow water. The monograph presents new method of calculation of viscous coefficient for a limited water depth. New formulae were used in classic Froude method of resistance extrapolation. The results of extrapolation obtained using the method proposed are presented. The Fluent professional software based on CFD method was used for calculating a model ship resistance.

Title: *An influence of external perturbation on pressure fluctuation in hydraulic system with proportional directional control valve*
(in Polish)
Wpływ wymuszenia zewnętrznego na pulsację ciśnienia w układzie hydraulicznym z rozdzielaczem proporcjonalnym

Author: Michał Stosiak

Supervisor: Professor Waclaw Kollek

Promoting Council: Institute of Machines Design and Operation, Wrocław University of Technology

Reviewers:

Doctor Zbigniew Zarzycki

Professor Edward Palczak

Date of PhD thesis presentation: April 12th, 2005

PhD thesis is available in Main Library and Scientific Information Centre of WUT

The monograph contains: 171 pages, 161 figs, bibliography: 93 items

Keywords: *pressure fluctuation, vibrations, proportional directional control valve*

Abstract: The original output of the dissertation is mathematical description of influence of external vibrations on changes in frequency spectrum of pressure fluctuation in hydraulic system with proportional directional control valve. Ph. D. student proved that mechanical vibrations e.g. mobile machine equipped with hydraulic system can lead to induce of vibration of valve control element and as a result pressure fluctuation in considered hydraulic system. In the PhD dissertation Author propose mathematical model of proportional directional control valve taking external vibrations into consideration and combine it with pressure fluctuation. On the basis of theoretical and experimental analyses included in the Ph. D. dissertation author shows ranges of external vibrations which entail maximal vibrations amplitudes of considered element of hydraulic valve and maximal pressure amplitudes in hydraulic system. Moreover created mathematical model allows to make wide analysis of influence of changes some structural and operation parameters on amplitude of vibration of forced element in hydraulic valve and pressure fluctuation as a result of induced vibrations. Suggested model can be useful for analysis results of elastic mounting of considered hydraulic valve on vibrating base.



Information about PhD thesis at the Civil Engineering Faculty and the Mechanical Engineering Faculty of Wrocław University of Technology

Title: *The influence of mechanical stabilizing systems on the strain of the lumbar spine structures (in Polish)*
Wpływ mechanicznych układów stabilizacji na odkształcenia struktur kostnych kręgosłupa lędźwiowego

Author: Sylwia Bukartyk

Supervisor: Doctor Franciszek Przystupa, Professor of Wrocław University of Technology

Promoting Council: Institute of Machines Design and Operation, Wrocław University of Technology

Reviewers:

Professor Dagmara Tejszerska

Doctor Tadeusz Smolnicki

Date of PhD thesis presentation: May 31st, 2005

PhD is available in Main Library and Scientific Information Centre of WUT

The monograph contains: 165 pages, 165 figs, bibliography: 102 items,

Keywords: *biomechanics of lumbar spine, transpedicular stabilizations, FEM*

Abstract: New transpedicular screws with multi-joint allow a better adaptation of lumbar spine to stabilizing systems. Clinicians ask whether and how to use those screws. This thesis answers to those questions.

This thesis deals with a mobile segment of the lumbar spine L3-L4 and its stabilization. This problem was considered because the dysfunctions of spine (particularly of the above-mentioned part) are common disease nowadays. The transpedicular stabilizer is a construction employed in the treatment of lumbar spine dysfunctions.

The monograph was divided into two parts. The first of them deals with the experiments on physical models with different variations of screws' connections; determination of mechanical properties of multi-joint screws and one-axis screws as loading characteristics. This is a complete analysis of transpedicular stabilization system. The second part presents numerical simulations that consists in L3-L4 mobile segment's FEM modelling taking account of different mechanical properties, dysfunctions and multi-joint screws and one-axis screws.

In the model of lumbar spine segment, use is made of ortotropic material properties (the values of parameters were taken from the literature), non-homogeneous bone structures and soft structure ligaments. The influence of muscles is also considered. Evaluation of the stabilization system stiffness and a global influence of those systems on the lumbar spine are given. Two different stabilization systems are examined by comparison. The influence of

loading on the behaviour of these systems and on the configuration of implant-spine is also given.

In the numerical simulations, the strain and the displacement in an anatomical and a dysfunctional segment and a stabilized segment were obtained. Two different biomechanical positions of human body were examined (erected and back-flexed postures).

Title: *Load capacity of RC columns strengthened by means of CFRP strips and wraps (in Polish)*
Nośność żelbetowych słupów wzmacnianych taśmami i matami z włókien węglowych

Author: Tomasz Trapko

Supervisor: Professor Mieczysław Kamiński

Promoting Council: Civil Engineering Faculty, Wrocław University of Technology

Reviewers:

Professor Maria Ewa Kamińska, Technical University of Łódź

Professor Jerzy Hoła, Wrocław University of Technical

Date of Ph.D. thesis presentation: February 16th, 2005.

PhD is available in Main Library and Scientific Information Centre of WUT

The monograph contains: 177 pages, 119 figs, bibliography: 66 items

Keywords: *column, compression, load capacity, strengthening, CFRP*

Abstract: The load capacity of RC columns strengthened by means of CFRP strips and wraps was investigated theoretically and experimentally. Survey of theoretical computational models referring to the elements subjected to compression was described.

The methods used for testing the load carrying capacity of reinforced concrete columns strengthened by means of CFRP strips and wraps and the testing procedures for CFRP materials in tension test were presented. The experimental was divided into four stages. The columns differed in the manner of constructing external strengtheners: internal adhesive bonding of longitudinal strips, external adhesive bonding of longitudinal CFRP strips, external adhesive bonding of transverse CFRP band wraps and external adhesive bonding of longitudinal CFRP strips with transverse wrapping (bands or jacket). In order to accomplish the objectives indicated, i.e. to determine the influence of the type of reinforcement on strain and strength properties of the materials tested, they were subjected to axial and eccentric compression.

CFRP strips used to strengthen the elements being compressed increase their boundary load carrying capacity. This is caused by a decrease in longitudinal strains in control elements at an equal increase in a longitudinal force. The use of additional external CFRP band wraps prevents a strip from de-bonding till the moment of the wrap breaking and the element damage.

Two theoretical models developed by Wang and Campione with Miraglia were described. On the basis of my own test results an expanded and modified model of Campione and Miraglia was proposed.

Title: *Border states of the great diaphragm clutches (in Polish)*
Stany graniczne wielkogabarytowych sprzęgieł membranowych

Author: Tomasz Jacek Zając

Supervisor: Doctor Franciszek Przystupa, Professor of Wrocław University of Technology

Promoting Council: Institute of Machines Design and Operation, Wrocław University of Technology

Reviewers:

Professor Sylwester Markusik

Professor Dionizy Dudek

Date of PhD thesis presentation: June 3rd, 2005.

PhD thesis is available in Main Library and Scientific Information Centre of WUT

The monograph contains: 106 pages, 64 figs, bibliography: 144 items

Keywords: *border states, diaphragm clutches, thin-walled elements*

Abstract: In the monograph, the border states of plastic deformation of great diaphragm clutches were analyzed. The purposes of this PhD thesis are as follows:

- to provide an analytic model of plastic deformation of diaphragm based on the models of deflection of thin-walled elements,
- to carry out the research on a real object in order to verify an assumption of deformation diaphragm model,
- to analyze the measurements in order to identify the causes of real plastic deformation of diaphragm,
- to generalize a plastic deformation phenomenon which allows application of numerical methods in the case of different loads and geometry.

Title: *Deterministic and stochastic methods of vibration analysis of suspension bridges (in Polish)*
Deterministyczne i stochastyczne metody analizy drgań mostów wiszących

Author: Danuta Bryja

Promoting Council: Council of Faculty of Civil Engineering, Wrocław University of Technology

Reviewers:

Professor Tadeusz Chmielowski, Opole University of Technology

Professor Piotr Konderla, Wrocław University of Technology

Professor Czesław Szymczak, Gdańsk University of Technology

Date of PhD thesis presentation: June 6th, 2005

PhD thesis is available in Main Library and Scientific Information Centre of WUT

The monograph contains: 237 pages, 69 figs, bibliography: 126 items

Keywords: *suspension bridges, theory of vibration, linear and nonlinear vibrations, random vibrations, correlation theory, numerical simulation, random highway traffic, reliability, bridge aerodynamics*

Abstract: A valid theory of spatial nonlinear vibrations of multi-span suspension bridges is formulated. Specifying more precisely the theory leads to generalization of earlier computational models. In the theory presented, specific features of suspension bridge vibrations are taken into account and therefore it can be applied to dynamic analysis of modern suspension bridges of typical structure systems with a multi-box stiffening girder. Based on such a theory an efficient algorithm for deterministic vibration analysis has been developed with respect to requirements for stochastic analysis of vibrations excited by a highway traffic and wind action. The algorithm has been applied to an eigenproblem analysis and to the analysis of the dynamic and static influence functions of cable tensions and displacements in selected cross-sections of a hypothetical bridge. The results of numerical investigation have justified the specification of the theory by taking the horizontal cable displacements into account. Particular attention has been paid to the problem of an appropriate damping model selection. The suspension bridge damping features have been described and the numerical solutions for the resonant vibrations corresponding to an excitation by the periodic series of concentrated moving forces have been analyzed for a few damping descriptions in the equations of motion of the bridge. In the second part of the dissertation, the methods of stochastic vibration analysis are formulated. Two entirely different methods for determination of the moment characteristics of random vibrations caused by highway traffic have been presented. The first one is the case of an analytical approach and relates to linear vibrations. In the second method meant for nonlinear vibrations, the simulation approach is applied with Monte Carlo principles to simulation of random events being used. By means of the simulation method the nonlinear effects have been analyzed and the influence of a vehicle springing and vehicle inertia forces on vibration characteristics of hypothetical bridge have been evaluated. When formulating the analytical method, the theory of stochastic Poisson process and dynamic influence functions of bridge response have been adopted. Based on the

analysis of the probability density function the possibility of modelling the traffic load effects by a stationary Gaussian process has been examined. The reliability of a suspension bridge with respect to the material fatigue and the first crossing of boundary level is also considered. Considerations are focused on the question of how the stochastic processes describing the bridge vibrations in a steady-state should be idealized in reliability problem. In the last part of the dissertation, the problem of vibrations excited by a gusty wind is investigated in the probabilistic approach. A stochastic nonstationary gusty wind model and the corresponding formulae for aerodynamic loads have been formulated. Solutions of the random vibration problem have been obtained in the range of correlation theory using the mathematical tools of stochastic processes. The wind field has been divided into many sections along the bridge span in order to take the spatial correlation between wind turbulences into consideration. The methods and algorithms for the dynamic analysis of a suspension bridge under highway traffic and gusty wind are characterized by the uniformity and similarity of approach as regards the time domain, so they can be a good basis for the total analysis of vibrations caused by simultaneous action of the two aforementioned loadings.

Title: *Topology optimization of continuum structure (in Polish)*
Optymalizacja topologii kontinuum materialnego

Author: Ryszard Kutylowski

Promoting Council: Council of Faculty of Civil Engineering, Wrocław University of Technology

Reviewers:

Professor Tadeusz Burczyński, Gliwice University of Technology

Professor Krzysztof Dems, Łódź University of Technology

Professor Piotr Konderla, Wrocław University of Technology

Date of PhD thesis presentation: January 19th, 2005

PhD thesis is available in Main Library and Scientific Information Centre of WUT

The monograph contains: 216 pages, 125 figs, bibliography: 81 items

Keywords: *topology optimization, variational method, minimum compliance, finite element method*

Abstract: Topology optimization answers the question about the way of distributing the material within a fixed domain to obtain the optimal topology of the structure for a given load and for the given boundary conditions.

In order to formulate the boundary problem, the variational method was used. It was also used to formulate the homogenized, relaxed topology optimization problem for a continuum structure. The compliance function was minimizing with the constraints put on the mass of the structure. In order to solve the problem numerically, the FEM algorithm was formulated. The steering parameters of the optimization process (the threshold functions, the relaxed functions and the Young modulus updating functions) were analyzed from the convergence and kind of topology points of view. Additionally some topology optimization problems for various civil engineering structures were solved, i.e. optimization of the structure with holes, the structure of decreasing mass, the structure of an increasing mass and an increase in the structure domain which can be useful during the fitting up the structure. Verification of the optimal distribution of internal ribs for the internally ribbed surface girders was also done.